Thermal and mechanical responsiveness of some 4-substituted benzonitriles

By

Lukman Olawale Alimi

Submitted in partial fulfilment of the requirements for the degree of Doctor of Philosophy

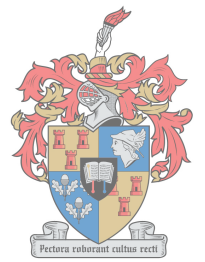

UNIVERSITEIT
iYUNIVESITHI
STELLENBOSCH
UNIVERSITY

Advisor: Prof. Leonard J. Barbour

Co-advisor: Dr Vincent J. Smith

Department of Chemistry and Polymer Science
Faculty of Science
Stellenbosch University

December 2018

Declaration

By submitting this thesis electronically, I declare that the entirety of the work contained therein is my own, original work, that I am the owner of the copyright thereof (unless to the extent explicitly otherwise stated) and that I have not previously in its entirety or in part submitted it for obtaining any qualification.

Lukman O. Alimi
December 2018

Acknowledgements

My unflinching appreciation goes to my advisor, Prof. Leonard James Barbour for giving me the opportunity to work independently in his laboratory. His style, passion and commitment to research are highly inspiring and worthy of emulation. I am glad to have benefitted immensely from your wealth of knowledge and worldwide connections. I will forever be grateful for the great support you have given me in the course of my study.

I am grateful to my co-advisor, Dr. Vincent Smith for his professional advice and contributions. I also really appreciate Dr. Prem Lama for his great assistance and professional information towards the success of this study. Thank you.

My sincere gratitude goes to all members of the Supramolecular Group, most especially those who have contributed to the success of my study. I say thank you to other technical staff of the De Beers building. To my soccer group, I will forever remember you. You people are awesome.

I am highly indebted to my parents and other family members as well as my parents-in-law for their support and prayers. To my dearest wife, Khadija Kuburah, I am deeply thankful for your love, understanding, support and sacrifice. To my lovely boys, Mubarak and Mukhtar, thank you for being wonderful kids. I love you all.

I am very grateful for the rare opportunity given to me by my home university (UMYU Katsina, Nigeria) to add a feather in my cap. I thank the Royal Society of Chemistry (RSC) for a travel grant to attend the ECM 29 conference in Croatia, and the Newton Fund Scholarship for my exchange program to Durham and Newcastle Universities in the UK. I thank Prof. Jonathan Steed and Dr Mike Probert of the Chemistry Departments of Durham and Newcastle Universities, respectively for hosting me.

Above all, I give all thanks to Almighty Allah who has made all this possible for without His grace nothing could be done. Alhamdulillah, Robil Al-Amin.

Abstract

This work is based on three publications.

The first manuscript describes the large volumetric thermal expansion of an organic cocrystal over a wide range of temperature (100–300 K). The novel organic multicomponent crystal (cocrystal) (ABN·2DMABN) consisting of 1:2 molar ratio of 4-aminobenzonitrile (ABN) and 4-(dimethylamino)benzonitrile (DMABN) was prepared. It shows linear positive thermal expansion (PTE) along all its three principal axes over the temperature range 100–300 K, which is exclusively dependent on the intermolecular interactions that govern the crystal packing. The associated volumetric thermal expansion coefficient (α_v) of 222 MK^{-1} is the largest reported to date for a cocrystal over such a wide temperature range.

The second manuscript explains the mechanical response/behaviour of a rigid small organic molecule, 4-bromobenzonitrile (4-BBN) that has been crystallised using sublimation under dynamic vacuum (0.02 mbar). Interestingly, the crystals show highly flexible plastic behaviour and bends along two orthogonal faces under mechanical stress– a rare phenomenon, resulting in helical twisting, or coiling, which is also rare for crystals of such rigid small organic molecules.

The third manuscript discusses the thermal behaviour of the purely organic material 4-aminobenzonitrile (ABN). The single crystals of ABN undergo reversible thermosalience upon cooling from 300 to 100 K and subsequent heating to 300 K. In this study we have demonstrated that the release of accumulated strain in these crystals upon cooling, which results in rapid structural rearrangement, is due to the interplay between the directional and non-directional intermolecular interactions in the system.

Abbreviations

SCXRD	Single Crystal X-ray diffraction
VT-SCXRD	Variable temperature single crystal X-ray diffraction
PXRD	Powder X-ray diffraction
VT-PXRD	Variable temperature powder X-ray diffraction
ZTE	Zero thermal expansion
NTE	Negative thermal expansion
PTE	Positive thermal expansion
FTIR	Fourier Transform Infrared spectroscopy
DSC	Differential scanning calorimetry
HSM	Hot stage microscopy
LM	Leica Microscopy
CIF	Crystallographic information file

Atom colour key

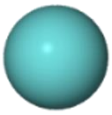

Hydrogen

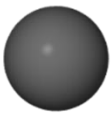

Carbon

Nitrogen

Oxygen

Bromine

Publications

4. Lukman O. Alimi, Dewald P. van Heerden, Prem Lama, Vincent J. Smith and Leonard J. Barbour, Reversible thermosalience of 4-aminobenzonitrile, *Chem. Commun*., 2018, **54**, 6208 – 6211.

3. Lukman O. Alimi, Prem Lama, Vincent J. Smith and Leonard J. Barbour, Hand-twistable plastically deformable crystals of a rigid small organic molecule, *Chem. Commun*., 2018, **54**, 2994 – 2997.

2. Lukman O. Alimi, Prem Lama, Vincent J. Smith and Leonard J. Barbour, Large volumetric thermal expansion of a novel organic cocrystal over a wide temperature range, *CrystEngComm*, 2018, **20**, 631 – 635.

1. Prem Lama, Lukman O. Alimi, Raj K. Das and Leonard J. Barbour, Hydration-dependent anomalous thermal expansion behaviour in a coordination polymer, *Chem. Commun.*, 2016**,** **52**, 3231 – 3234.

Furthermore, a conference paper was published during the course of the PhD study

- Lukman O. Alimi, Vincent J. Smith and Leonard J. Barbour, Thermosalient effect of an organic aminonitrile and its derivatives, *Acta Crystallogr*., 2015, **A71**, s455.

Conferences

6. 23rd International Conference on the Chemistry of Organic Solid State (ICCOSS XXIII), STIAS, Stellenbosch University, South Africa, April 2 – 7, 2017.
   Poster presentation: *Tuning thermomechanical properties of thermosalient organic materials.*

5. 1st Miniconference, Newton Fund International, Polymer Science Building, Stellenbosch University, South Africa, September 19 – 20, 2016.
   Oral presentation: *Tuning thermomechanical properties of thermosalient organic materials.*

4. UK Soft Matter Showcase, Newton Fund International: Leeds University, United Kingdom, June 29 – 30, 2016.

3. 7th UK-Japan Symposium on Fundamental Research Advances in Carbon Nanomaterials: Royal Society of Chemistry Building, Burlington House, London, United Kingdom, June 13, 2016.

2. 29th European Crystallographic Meeting (ECM 29), Conference Centre, Rovinj, Croatia, August 23 – 28, 2015.
   Oral presentation: *Thermosalient effect of an organic aminonitrile and its derivatives.*

1. 1st International Meeting on Porous Molecular Solids (POMOS), STIAS, Stellenbosch University, South Africa. April 7 – 10, 2015.
   Poster and Oral presentation: *Noble gas inclusion compounds of an organic molecular host: 4-Phenoxyphenol*.

Table of contents

Chapter 1: Introduction

1.1. Supramolecular chemistry

Supramolecular chemistry is one of the areas of chemistry which deals with secondary interactions between molecules rather than covalent bonds within molecules and focuses on the chemical systems made up of a discrete number of assembled molecular subunits or components.[1] Generally, the forces responsible for the spatial organisation may vary from weak intermolecular forces to strong covalent bonding[1] but the advent of supramolecular chemistry has had a profound effect on how efficiently chemists prepare molecules of different sizes and shapes with dimension in the range of 1 to 100 nm using spontaneous secondary interactions such as hydrogen bonding, dipole-dipole interactions, halogen bonding, van der Waals interactions, π···π stacking interactions and electrostatic effects.[2-7] The existence of intermolecular forces was first postulated by Johannes Diderik van der Waals in 1873. However, it is with 1902 Nobel laureate Hermann Emil Fischer that supramolecular chemistry has its philosophical roots. The importance of supramolecular chemistry was established by the 1987 Nobel Prize for Chemistry which was awarded jointly to Donald J. Cram, Jean-Marie Lehn, and Charles J. Pedersen in recognition of their work in this area.[8]

In the 1990s supramolecular chemistry became even more sophisticated, with researchers such as Stoddart developing molecular machinery and highly complex self-assembled structures, and Willner developing sensors and methods of electronic and biological interfacing.[9-13] During this period, electrochemical and photochemical motifs became incorporated into supramolecular systems to increase functionality, research into synthetic self-replicating systems began, and work on molecular information processing devices was initiated.[13]

In the development of new materials with interesting properties supramolecular chemistry and molecular self-assembly processes have been applied to a great extent.[14] Supramolecular chemistry research has drawn much inspiration from naturally-occurring macromolecular structures, since biological processes such as protein folding, enzyme-substrate binding and the zipping and unzipping of DNA all rely on non-covalent intermolecular interactions.[15-17] In recent years, the field has developed beyond the examination of supramolecular interactions to facilitating our current understanding of the development of supramolecular materials with exciting properties such as molecular separation and storage,

negative thermal expansion, thermosalient effects, sensing, soft electronics and catalysis. Most recently, the 2016 Nobel Prize in Chemistry was awarded jointly to Jean-Pierre Sauvage, Sir J. Fraser Stoddart and Bernard L. Feringa *"for the design and synthesis of molecular machines"* in supramolecular chemistry, which further establishes the relevance and potential of this area of chemistry.

1.2. Supramolecular interactions

A crystal bears the collective properties of molecules moderated by intermolecular interactions.[18] So, in crystal engineering it is crucial to distinguish different interaction types in any design strategy. It is immensely difficult to predict crystal structures of molecular substances *ab initio* because the determining factors, namely the intermolecular interactions, are weak (supramolecular interactions) and numerous with limited directionality.[19] Almost all interactions in crystals are electrostatic in nature and the strength of the interaction depends on the degree of polarisation of the molecules involved.[20] Intermolecular interactions can also be directional or nondirectional. Directional interactions determine the geometry and spatial alignment of molecules, while the nondirectional contacts exert a long-range influence over the orientation of molecules with respect to one other.[21] Moreover, supramolecular interactions are reversible, whereas covalent bonds are usually irreversible. The use of supramolecular interactions to direct the spontaneous assembly of molecules is of utmost importance owing to their high specificity, controlled affinity, and reversibility.[22] Supramolecular interactions also control the path of molecular recognition, the mode of the crystal packing arrangement and, in the case of flexible molecules, the molecular conformation.[23] The intermolecular interactions that are specifically relevant to this study are discussed in detail below.

1.2.1. Hydrogen bonds

Hydrogen bonding interactions, one of the better understood types of non-covalent interactions,[24,25] are a powerful organising influence in designing solids for several reasons: they are directional, selective and their formation is reversible at room temperature.[26-28] Linus Pauling was the first to describe the hydrogen bond in 1931[29] as a bond formed between a polarised hydrogen atom (due to its covalent connection to an electronegative atom X) and an acceptor atom A that has a lone pair of electrons or polarisable π-electrons.[21,30] The IUPAC task group defined hydrogen bonding as “an attractive interaction between a hydrogen atom from a molecule or a molecular fragment D–H, in which D is more electronegative than H, and an atom or group of atoms in the same or different molecule in which there is evidence of bond

formation".[31] Hydrogen bonds are mainly electrostatic in nature.[20] Hydrogen bonds could be categorised as strong, moderate or weak, depending on the distance between the donor and acceptor as well as the bond angle that exists between them.[31,32] The strength of the hydrogen bond varies due to the wide range of possible donor-acceptor pairs, depending on how well they are able to determine and control supramolecular assembly.[32] Although the strength of a hydrogen bond is usually defined in terms of energy to break the bond, that it can only be classified as strong, moderate or weak according to certain geometric parameters of the hydrogen bond such as listed in Table 1.

Table 1. Strong, moderate, and weak hydrogen bonds[33, 34]

	Strong	**Moderate**	**Weak**
Interaction type	strongly covalent	mostly electrostatic	electrostatic/disperse
Bond length [Å], H···A	1.2-1.5	1.5-2.2	>2.2
Lengthening of D-H [Å]	0.08-0.25	0.02-0.08	<0.02
D-H versus H···A	D-H ≈ H···A	D-H < H···A	D-H << H···A
D···A [Å]	2.2-2.5	2.5-3.2	>3.2
Directionality	strong	moderate	weak
Bond angle [°]	170-180	>130	>90
Bond energy [kcal/mol]	15-40	4-15	<4
Relative IR shift [cm^{-1}]	25%	10-25%	<10%
^{1}H downfield shift	14-22	<14	

It is possible for a hydrogen atom to interact with more than one acceptor atom, especially in the case of weak hydrogen bonds. If a hydrogen atom hydrogen bonds to only one acceptor atom, it is seen as a simple hydrogen bond. If it hydrogen bonds to two or three acceptor atoms or two or three hydrogen atoms from a donor atom bond to one acceptor atom, it is described as a bifurcated or trifurcated hydrogen bond, respectively.[35] This concept is shown in Figure 1.1.

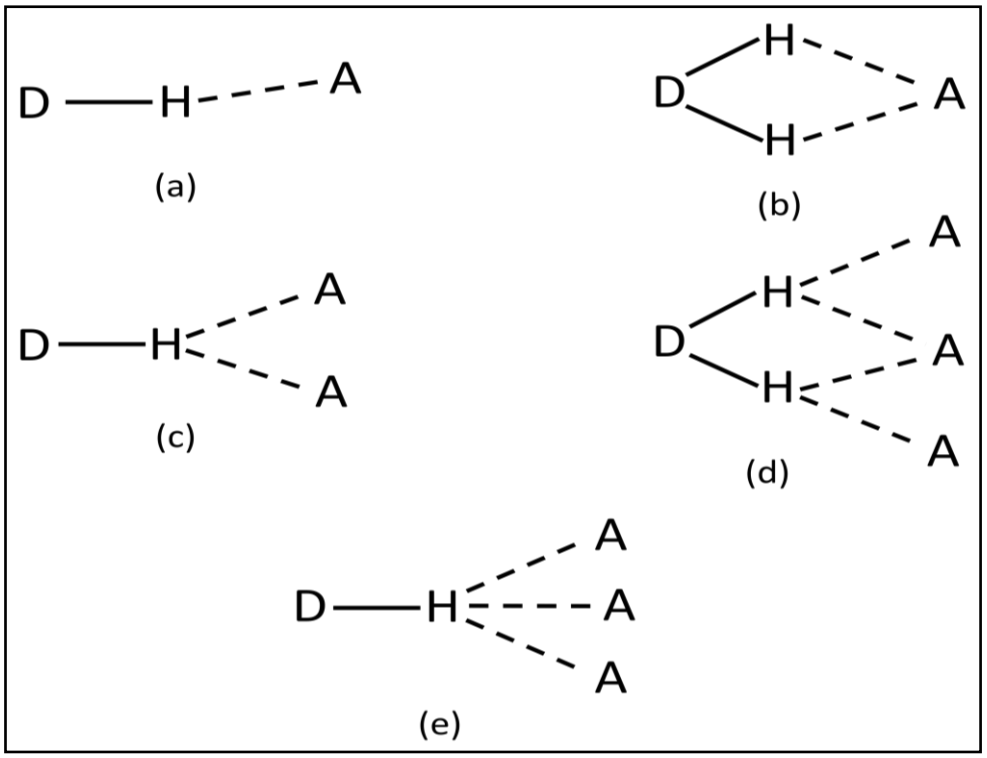

Figure 1.1. (a) Nearly linear, (b) and (c) bifurcated, (d) three center bifurcated and (e) trifurcated hydrogen bonds.

It is generally known from X-ray crystallography that most hydrogen bonds are non-linear.[36] Figure 1.1 shows possible ways in which hydrogen atoms can interact with the acceptor atom(s). During this study, we observed the presence of three center bifurcated[37, 38] hydrogen bonding interactions in one of the systems we investigated. In this case, the two hydrogen atoms from one donor atom hydrogen bond with three different acceptors. The rules governing the formation of this type of hydrogen-bonding interaction and the order of the interactions have been proposed by Etter.[39] These rules play a vital role in selecting molecules and functional groups to employ in the design of desired structures. The rules are: (1) "*all good proton donors and acceptors are used in hydrogen bonding*",[39] (2) "*six-membered-ring intramolecular hydrogen bonds form in preference to intermolecular hydrogen bonds*"[39] and (3) "*the best proton donors and acceptors remaining after intramolecular hydrogen-bond formation form intermolecular hydrogen bonds to one another*." [39] These rules and guidelines for which hydrogen bonds preferentially form in the solid state remain highly relevant to present day crystal engineering.

Supramolecular synthons[40] depict the possible ways in which complementary functionalities of molecules interact by non-covalent interactions such as hydrogen bonds. In this case, the hydrogen bond is a strong, directional, selective and stabilising interaction

between a hydrogen atom and an electronegative atom. As depicted in Figure 1.2, supramolecular synthons can either be self-complementary (a supramolecular homosynthon such as a carboxylic acid dimer[41]) or the result of complementary interactions between different moieties (a supramolecular heterosynthon such as a DNA base pair or the well-known carboxylic acid-pyridyl interaction[39]).

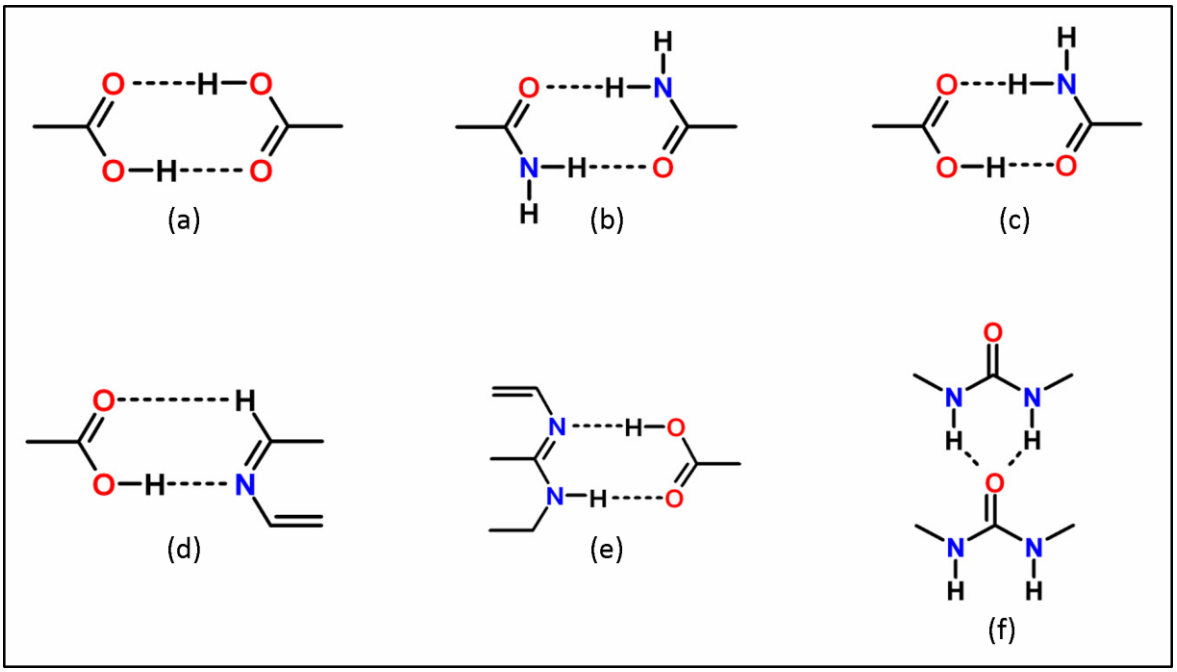

Figure 1.2. Representative supramolecular synthons (homo and heterosynthons).

1.2.2. Halogen bonds

Non-bonded attractions, typically 1–11 kcal mol^{-1}, between covalently bonded halogen atoms and other functionalities have been identified for a long time.[42,43] However, their frequency of occurrence and significance to crystal engineering have become very widely recognised during the past few years. Metrangolo[44] and Resnati[44] introduced the term halogen bonding to describe this highly important group of interactions. If a hydrogen bond is represented generally as –X–H···Y, then its analogous halogen bond is –Hal···Y.[44] Thus halogen bonding includes situations such as Hal···O, Hal···N, Hal···Hal and Hal···π, where the interaction energy follows the trend Hal = I > Br > Cl > F (Figure 1.3). According to a recent IUPAC recommendation, "a halogen bond occurs when there is evidence of a net attractive interaction between an electrophilic region associated with a halogen atom in a molecular entity and a nucleophilic region in another, or the same, molecular entity".[45]

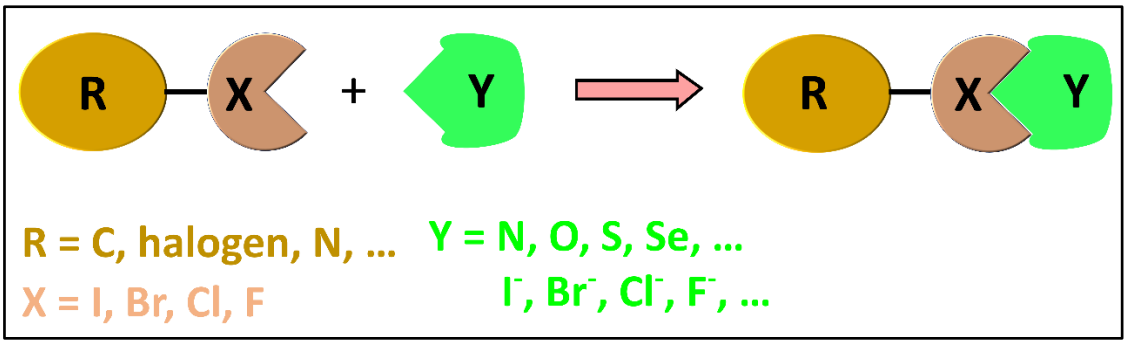

Figure 1.3. Diagram showing formation of the halogen bond.[46]

Saccone *et al*. have described halogen bonds as particularly directional interactions, i.e. more directional than hydrogen bonds.[47] The great directionality of the halogen bond is due to the fact that during interaction the nucleophile enters the halogen atom σ-hole which is narrowly confined on the elongation of the R−X covalent bond axis, and the R−X···Y angle between the covalent and noncovalent bonds around the halogen is approximately 180°.[46,48] Figure 1.4 shows the CSD[46] (version 5.35) scatterplots of intermolecular C−X···N interaction versus X···N distance (X = I, Br, and Cl) relevant to the one established in the course of this study. Obviously, short and strong halogen bonds are more directional than the long and weak ones, and by reducing the polarizability of the halogen bond donor, the linearity slightly decreases (mean values for the C−X···N angle are 171.4° for I, 164.1° for Br, and 154.6° for Cl). This trend is general and has also been observed when halogen bond acceptor sites besides nitrogen are used.[46]

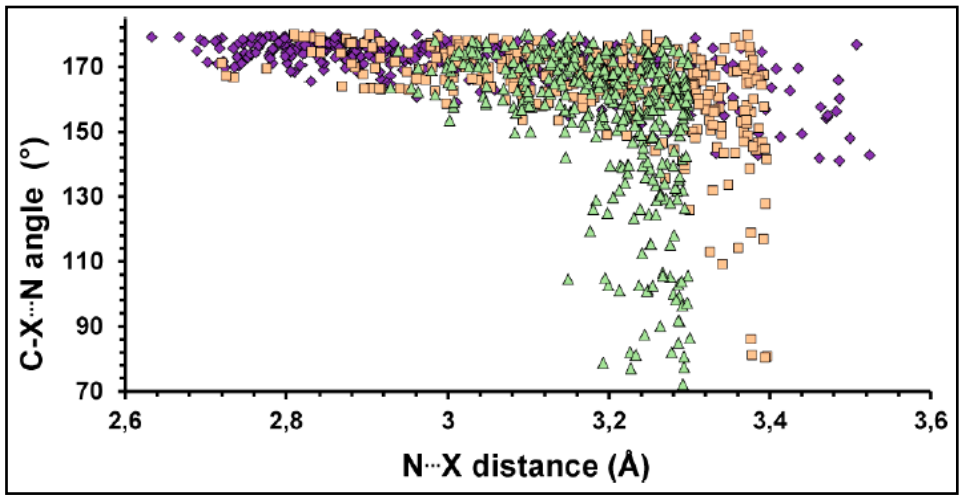

Figure 1.4. Scatterplot obtained from a CSD search showing the C−X···N angle (°) against the X···N distance (Å) for crystal structures with X···N contacts. Blue rhombuses, I···N contacts; pink squares, Br···N contacts; green triangles, Cl···N contacts. Consideration is for structures that are error-free, not polymeric with single-bonded I, Br, or Cl atoms and are not disordered with R < 0.05.[46]

1.2.3. π···π interactions

These interactions generally occur between aromatic regions of molecules and can be classified as a type of electrostatic interaction due to the arrangement of the electrons of the aromatic system.[49] They are weakly directional and are weaker than hydrogen bonding interactions.[50] Calculations give about 2.4 kcal/mol (for typical aromatic–aromatic interactions), in comparison with 4–10 kcal/mol (for moderate hydrogen bonds between neutral molecules).[50] At the supramolecular level, the aromatic rings can interact in different ways: stacked arrangement (face-to-face, perfect alignment, and offset, slipped, parallel displaced) and edge- or point-to-face, T-shaped conformation (Figure 1.5).[51]

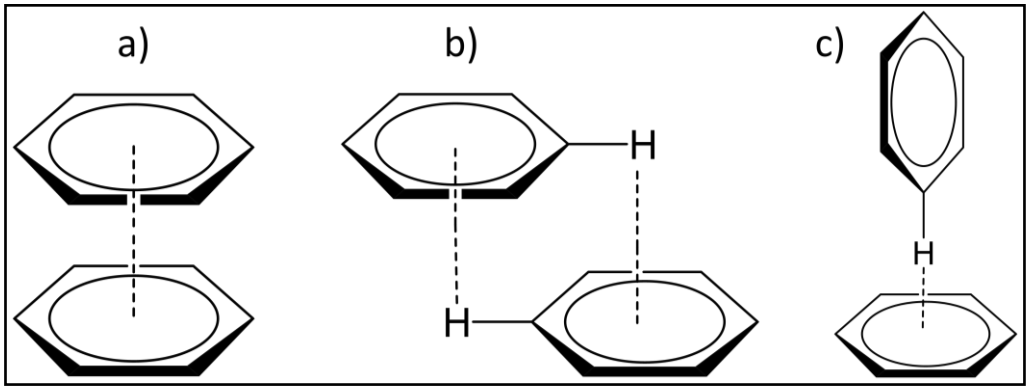

Figure 1.5. The three positionings of benzene dimers: a) face-to-face or stacked, b) offset parallel or offset stacked and c) edge-to-face or T-shaped.[21]

1.2.4. Van der Waals interactions

These are attractive or repulsive forces between molecular entities (or between groups within the same molecular entity) apart from those due to formation of bond or to the electrostatic interaction of ions or of ionic groups with one another or with neutral molecules.[52] They include dipole–dipole, dipole-induced dipole and London (instantaneous induced dipole-induced dipole) forces.[52] van der Waals interactions are generally weak interactions, less than 1.2 kcal/mol,[21] but they are found in large number within a crystal structure, they often contribute largely to how molecules pack in the solid state.[53] They also determine solubility, density, as well as boiling and melting points of organic materials.[53-55]

1.3. Organic cocrystals

Cocrystals are crystals containing two or more neutral molecular components that rely on noncovalent interactions to form a stoichiometric regular arrangement in the solid-state (Figure 1.6).[56-59] Through cocrystallisation, properties can be dramatically altered, and this technique

has therefore been applied to a substantial extent in pharmaceuticals to improve solubility, dissolution rate, stability, bioavailability, morphology, colour, and melting point.[57] In this thesis, cocrystallisation is used as a method to improve properties critical to energetic materials. Through the formation of cocrystals, commonly used energetic materials may be improved and existing energetic materials that do not meet all the requirements for a specific application could be made viable. Cocrystallisation has seen application in many fields, including research on pharmaceutical materials,[60-67] optoelectronic materials,[68,69] and non-linear optical materials.[70-73] For example, the energetic materials nitroglycerin and triacetone triperoxide (TATP) have desirable qualities such as high power and inexpensive synthesis, respectively, but because of their high shock sensitivity, none of them are used in their pure state. Through cocrystallisation, such materials could be stabilised to enable their common use.

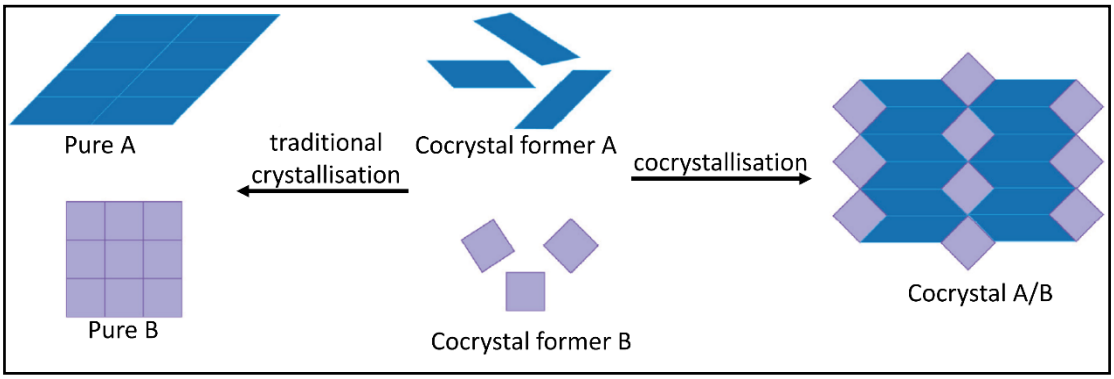

Figure 1.6. Cocrystallisation combines two or more neutral molecular components in a defined ratio within a crystal. This produces a material distinct from the pure cocrystal formers.

1.4. Thermal expansion in organic crystals

In general, solids expand in all directions upon heating due to anharmonic thermal vibration of atoms, i.e. they show positive thermal expansion (PTE) behaviour.[74,75-77] However, a few solids show the reverse effect, i.e. they contract upon heating, and so display negative thermal expansion (NTE).[78] These types of materials have attracted an increasing amount of interest because of their potential applications. The causal mechanisms for NTE have been found to be complex,[78] unlike most solids that have positive thermal expansion coefficients in which the mechanism is due largely to an increase in the interatomic bond length, which appears at the macroscopic level as an overall increase in a dimension or volume.[78] Thermal expansion is measured in terms of thermal expansion coefficient. If the length of a crystal along a particular direction is L_i at an initial temperature, T_i (K) and L_f at final temperature, T_f (K), then the linear thermal expansion coefficient,

$$\alpha_1 = \frac{L_f - L_i}{L_i\,(T_f - T_i)} \quad (K^{-1})$$

Similarly, if the initial volume is V_i at T_i (K) and the final volume is V_f at T_f (K), then the volumetric thermal expansion coefficient,

$$\alpha_v = \frac{V_f - V_i}{V_i\,(T_f - T_i)} \quad (K^{-1})$$

The above equations are used in crystals with orthogonal unit cell axes where the linear thermal expansion coefficients are calculated along the crystallographic axes. The principal axis strain calculator (PASCal program)[79] is used when the unit cell has non-orthogonal axes.

The magnitude of this expansion differs for different types of materials. A typical inorganic compound generally shows α_v in the range 0–20 × 10^{-6} K^{-1}, but for crystals of small organic molecules and MOFs, it is usually around 100–300 × 10^{-6} K^{-1}. Even though many thermal expansion studies have been reported on inorganic[75-77,80-88] and on metal–organic-based systems,[89-93] those on purely organic systems[94-96] are still rare.

There are some interesting studies on thermal expansion in organic crystals in the literature that are relevant to this study. Generally, noncovalent interactions, responsible for self-assembly in a crystal explain many thermal expansion properties of solids. It is known that thermal expansion decreases with increasing interaction strength.[97-100] Saha *et al*. have shown this in a one-dimensional hydrogen-bonded dimorphic co-crystal system in which the molecules, 1,2,3,4-cyclobutanetetracarboxylic acid and trans-1,2-bis(4-pyridyl)ethylene are assembled via strong O–H···N hydrogen bonds along one direction, in another via relatively weaker C–H···O interactions, and in the third via weak van der Waals contacts.[100,101] In this example, it was revealed that the order of thermal expansion follows the reverse order of interaction strength of these interactions, i.e., the highest expansion is observed along the weak van der Waals contacts and the lowest along the strong O–H···N hydrogen-bonded direction.[100]

Birkedal *et al*. have reported the thermal expansion study of the monohydrate of dipeptide tryptophylglycine crystal.[100,102] In this case, the molecules are arranged in a helical fashion forming channels in the crystal structure.[100,102] The channels are occupied by hydrogen-bonded water chains. As the temperature decreases, the hydrogen bonds become more directional and the water molecules start occupying favoured sites, causing a uniaxial negative

thermal expansion along the channel direction. A similar phenomenon causes lowering of density when the liquid water is condensed to ice.[100,102]

Thermal expansion studies have been performed on some organic energetic materials too.[100] In the energetic materials, γ and ε polymorphs of hexanitrohexaazaisowurtzitane (HNIW) and β form of 5-nitro-2,4-dihydro-3H-1,2,4-triazol-3-one (NTO), the thermal expansion coefficients (α) along the principal axes are shown in Table 2.[100,103,104] Therefore, in these energetic materials, the thermal expansion is found to be less anisotropic.

Table 2. Thermal expansion coefficients of some energetic materials over the temperature range 100 to 298 K

	α_{X1} (MK^{-1})	α_{X2} (MK^{-1})	α_{X3} (MK^{-1})
γ-HNIW	−8.8(9) to −5.0(3)	10.5(7) to 21.1(3)	63(2) to 84.3(6)
ε-HNIW	4(2) to 19.6(6)	29(2) to 45(1)	30(2) to 53.8(7)
β-NTO	−4.7 to 12.3	64.0 to 66.8	57.7 to 90.2

Our research group carried out thermal expansion studies of dimorphic (*S*,*S*)-3,5-octadiyn-2,7-diol. Both forms show very similar hydrogen-bonding patterns and similar packing.[100,105,106] The only noticeable difference is in the stacking angle of the molecules (Figure 1.7).[100,106] But, interestingly, these two forms have shown different thermal expansion properties. One of the forms shows highly anisotropic thermal expansion (156 $MK^{-1} < \alpha_a <$ 515 MK^{-1}; −32 $MK^{-1} < \alpha_b <$ −85 MK^{-1} and −48 $MK^{-1} < \alpha_c <$ −204 MK^{-1}) in the temperature range 225–330 K, whereas the other form does not.[100,105,106] These examples show the extent to which the packing of the molecules in a crystal structure can affect their thermal expansion behaviour.[100]

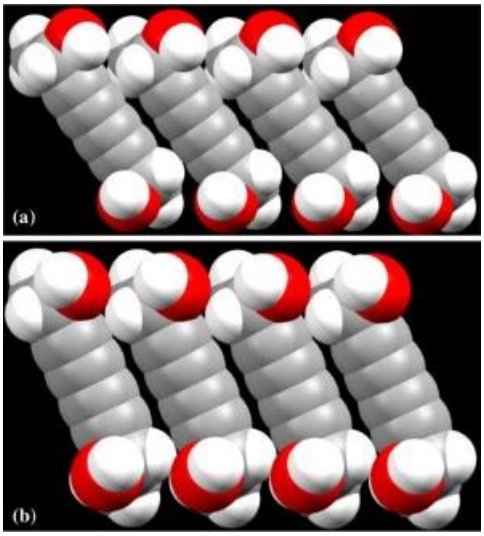

Figure 1.7. Stacking of (*S*,*S*)-3,5-octadiyn-2,7-diol molecules in the a) high- and b) low-temperature phases. In a), the molecules are more tilted to the stacking propagation axis compared to those in b).[100,105]

In another study Engel *et al*. compared the thermal expansions of the isostructural nitromethane, acetonitrile, and iodomethane solvates of 18-crown-6.[100,107,108] They showed that, even though they are isostructural, the first two solvates show uniaxial negative thermal expansion, while the third (iodomethane) exhibits uniaxial zero thermal expansion, and they all have very different volumetric thermal expansion coefficients of 378(22), 226(3), and 256(8) MK^{-1}, respectively.[100,107,108]

The effect of solvent/guest in thermal expansion of solvates was also investigated by Saha.[100,109] Two groups of isostructural systems of 2,4,6-triethyl-1,3,5-tris(4-halophenoxy)methylbenzene (halo = Cl, Br and I) and their ethyl acetate solvates were examined, the volumetric thermal expansions of the three guest-free crystals are 2.8–3.4%, which is considerably smaller than those of the three corresponding ethyl acetate solvates (4.2–4.4%) in the temperature range 118–298 K. Due to this observation, it was concluded that the presence of solvent molecules as guest causes increased thermal expansion in the host lattices.

MacGillivray *et al*. also reported uniaxial zero thermal expansion, this time in 1:2 and 1:1 cocrystals of 2,4-dihaloresorcinol (halo = Cl, Br, I) with 4-phenylazopyridine and 4,4′-azopyridine over a temperature range of 190–290 K and 170–290 K, respectively.[100,110,111] They observed pedal motion, which has a considerable impact on thermal expansion properties in the 1:2 cocrystals (halo = Cl and Br). Interestingly, in the case of the 1:1 series, the cocrystal with the iodo compound exhibited higher volumetric thermal expansion (196(9) MK^{-1}) than

the corresponding chloro (185(3) MK^{-1}) or bromo (181(2) MK^{-1}) compounds, and the latter two showed comparable volumetric thermal expansion.[100]

1.5. Bending crystals

Mechanical bending in molecular crystals was first observed by Desiraju and co-workers in single crystals of hexachlorobenzene (space group $P2_1/n$), and afterward became a well-known phenomenon.[112-114] Bending occurs in molecular crystals when the packing is anisotropic in such a way that strong and weak interaction patterns occur in approximately perpendicular directions.[111] Interactions in such crystals are not uniform and similar in all directions. Bending can be understood based on a structural model that takes into consideration the highly anisotropic nature of the packing.[112] When a single crystal bends, two parallel opposite faces become non-planar.[112] The crystals that once bent, do not regain their original shape on release of the mechanical stress. This is called "plastic bending."[112-114] Some organic materials have been reported to display this bending property.

Reddy and co-workers reported on different organic crystals[55,112-114] where they observed that bending is as a result of crystal packing and does not rely on the morphology of the crystal.[112] For example, in the monoclinic form of the dimorphic compound, 4-nitrobenzoic acid (NBzA),[114-116] the bending face of the crystal is the thickest face, (101), along which the weak C–H···O interactions are present (Figure 1.8). The prominent face is (100) which is the thinnest face but the crystal breaks when mechanical stress is applied on this face.[114] Also, in the α-form of pyrazine-2-carboxamide (PyCA-α),[114,117-120] the bending face is the thickest face because of the emergence of weak and non-specific interactions through this face (Figure 1.9).[112] This demonstrates the strong reliance of mechanical behaviour on the underlying structure in the molecular crystals.[112, 114]

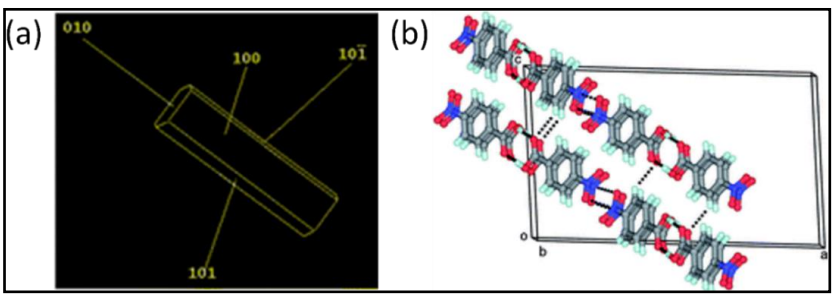

Figure 1.8. 4-nitrobenzoic acid**,** NBzA. (a) image of the crystal face indexing. The crystal bends on the thickest face, (101). (b) The head-to-head antiparallel dimers are connected by C–H···O weak interactions.[112]

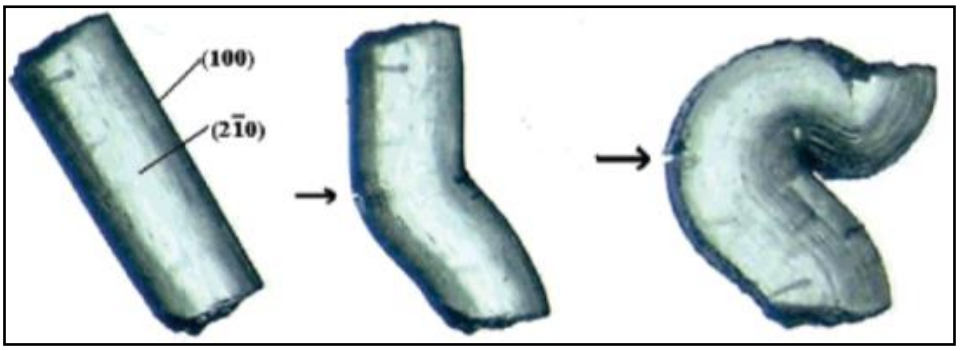

Figure 1.9. Images showing step by step bending of PyCA-α crystal on the plane (100). Arrows show points of breaking.[112]

In another example, the structure of hexachlorobenzene (C_6Cl_6),[121] the planar molecules form π···π stacks along the crystal length with Cl···Cl interactions (Figure 1.10).[113,116] Within these stacks, the molecules are tilted away from the stack direction so that the π···π interactions are enhanced. However, Cl···Cl interactions are not significant, but π···π stacking dominates the packing of the crystal structure.[112] Therefore, the bending face of the crystal is (001), from which the weak and non-specific Cl···Cl contacts emerge.[112]

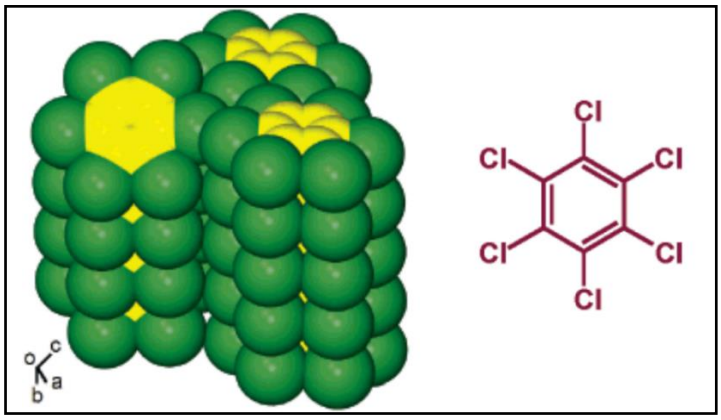

Figure 1.10. Packing in crystals of C_6Cl_6.[112-114]

Interestingly, it is possible to deform the C_6Cl_6 crystals into various shapes by changing the direction and the point at which the stress is applied to the crystal (Figure 1.11).[113,114] In extreme cases, the crystals can be flattened onto themselves without breaking,[112] i.e., they are highly plastic/ductile. The weak nature of the Cl···Cl interactions in C_6Cl_6 is further confirmed by the fact that the crystal can be bent into different shapes depending on the manner in which the force is applied (Figure 1.10).[113,114] It was thereby concluded from the mechanical experiments that the interactions between halogen atoms are weaker and/or less specific than the π···π interactions within these stacks.[114]

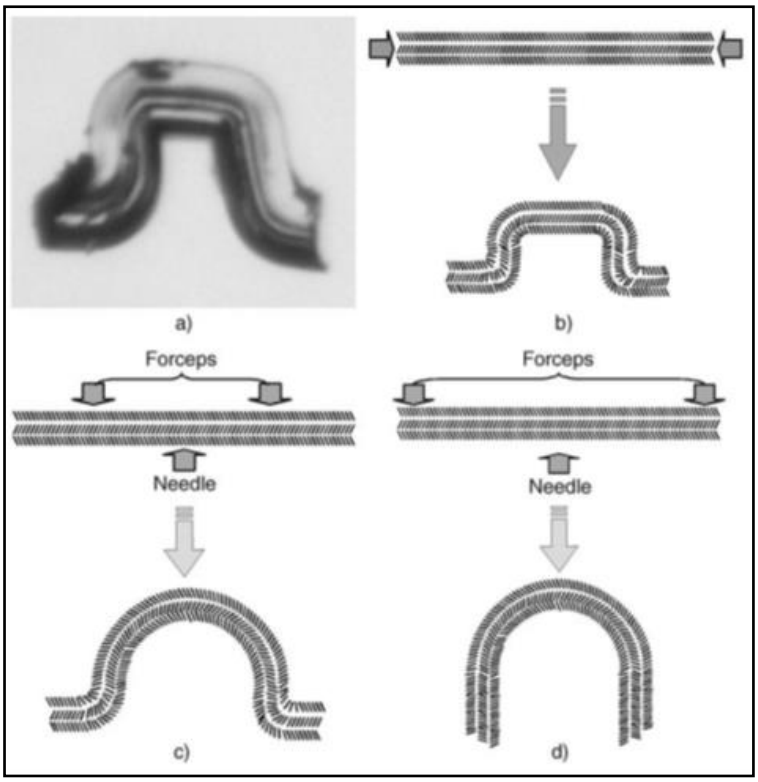

Figure 1.11. Bending of a C_6Cl_6 crystal into different shapes when mechanical stress is applied at different directions. (b) and (c) indicate no variation in the interfacial angles at each crystal ends[113,114]

The crystals of 4-fluorobenzonitrile[116,122] (4-FBN) and 4-chlorobenzonitrile[116] (4-CBN) have been reported to display bending behaviour by Reddy *et al.*[112] In case of 4-FBN, the molecules are connected through weak C–H···N and C–H···F interactions to form corrugated layers with weak van der Waals interactions in between the corrugated layers (Figure 1.12).[112] They observed that the crystals of 4-FBN bend on the face through which C–H···F interactions occur.[112] Also in case of 4-CBN, they reported that the molecules are connected through weak C–Cl···N and C–H···N interactions (Figure 1.13) that form a corrugated sheet and there are van der Waals interactions between the sheets which allow the crystals to bend when a mechanical stress is applied.[112]

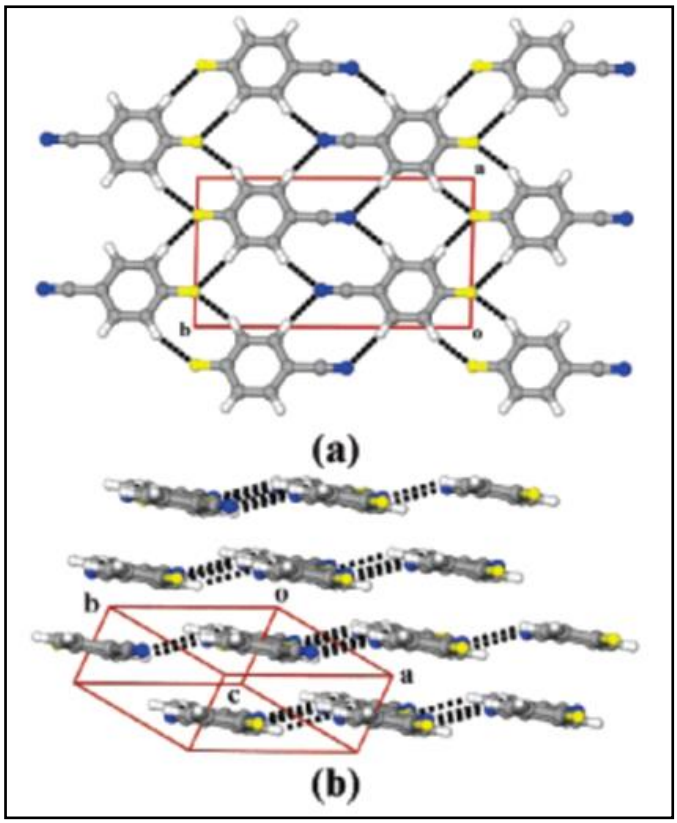

Figure 1.12: (a) Packing diagram of 4-FBN shows the single-layer when viewed down the *c* axis; (b) corrugation of layers.[112]

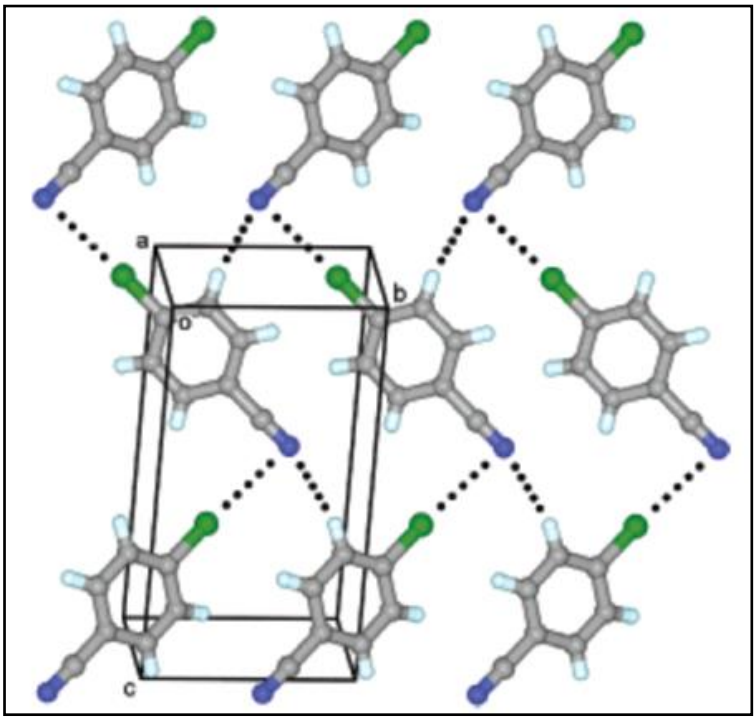

Figure 1.13: Packing diagram of 4-CBN showing the layer formed through C–Cl···N and C–H···N interactions when viewed down the *a* axis.[112]

Some other materials, on the other hand, have been reported to display bending in two faces of the crystal that are orthogonal to each other (two-dimensional bending)[123,124] unlike the one-dimensional bending where only the two parallel crystal faces bend when mechanical stress is applied. This allows the crystals to twist or coil, leading to the formation of helical shapes.[125,126] There are only a few examples of such materials in the literature.[125,126] Helical crystals are generally produced through different methods of crystallisation such as slow evaporation of solvent, sublimation, or diffusion-limited growth in different types of gel media. Materials with these properties have potential as functional materials with specific optical, electric, or catalytic properties, negative-index metamaterials (invisible materials), and enantiosensitive plasmonic sensors.[125,127] In this study, one of the materials we investigated shows this rare phenomenon of bending under mechanical stress.

1.6. Thermosalient materials ("Jumping crystals")

In 1987, Gigg and coworkers suggested the less colloquial term "thermosalient crystals", for thermally-induced jumping crystals.[128] The first report that clearly mentions jumping of organic crystals is a report by Etter and Siedle in 1983.[129] In 1960, it was reported that "a single crystal of ferrocene, when cooled to 77 K, undergoes a violent disintegration; same effect was reported for nickelocene.[130] This description is similar to the visual effect observed during a thermosalient transition.[130] Bodenheimer and Low provided evidence that the phase transition and crystal disintegration are separate phenomena.[131] However, the effect was later studied by calorimetry,[132] and it was revealed that the fragmentation is due to energy transfer from the accumulated strain to the kinetic energy of the fragments; thus, the mechanical effect is triggered by the latent strain accrued during the transition. Figure 1.14 depicts some examples of thermosalient crystals.[132]

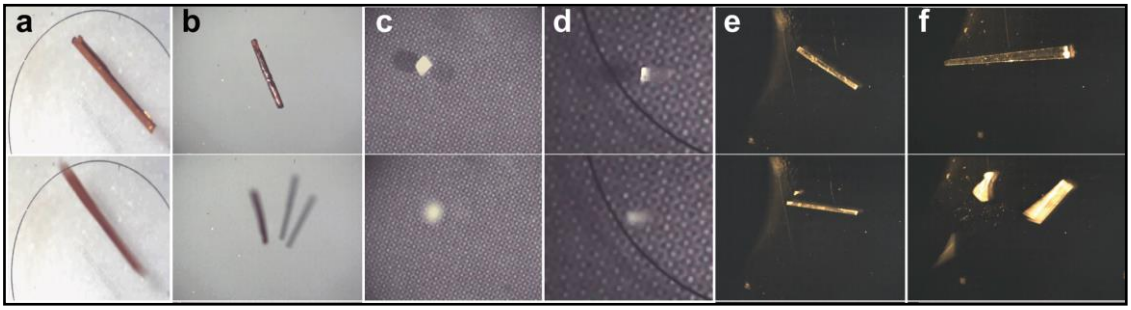

Figure 1.14. Different examples of single crystals that exhibit thermosalient properties. (a, b) Phenylazophenyl) palladium(II) hexafluoroacetylacetonate, (c, d) pyroglutamic acid, and (e, f) 1,2,4,5-tetrabromobenzene. Upon heating, the crystals jump.[133]

The anomalous thermal expansion (of thermosalient solids) is accommodated by reduction along some of the axes.[124] The potential practical applications of the thermosalient effect for direct conversion of thermal energy into mechanical work in organic-based actuators make these solids important materials for future technologies.[133] Jumping crystals represent the most visually impressive demonstration of the macroscopic effects caused by the combined action of relatively weak intermolecular interactions at the molecular level.[133] Indeed, these materials are capable of exerting mechanical force that can develop because of accumulating strain within single crystals.[133] The few documented examples are precious cases and provide the opportunity to acquire a complete understanding of the expression of molecular structural changes at the macroscopic level.[133] Unfortunately, in most cases, the phase transitions causing the thermosalient effect cannot be restored and the propulsion is followed by splitting, shattering, deformation, explosion, twinning, and sublimation of the crystal at high temperature.[133] These hindrances make it particularly difficult to obtain comprehensive structural analysis of the thermosalient phase transition. Consequently, there is only limited experimental evidence on the mechanisms of associated phase transitions, and systematic correlations of the phenomenon with the structure have not yet been established to allow prediction of this effect.[133]

Recently, understanding the mechanism of the thermosalient phenomenon was accomplished with the anticholinergic medicine oxitropium bromide.[134,74] In this system, the thermosalient effect is as a result of first-order phase transition between two phases that have the same crystal symmetry,[134] which is followed by a strongly anisotropic cell expansion of 4% (the *b* axis increases by 11% and the *c* axis decreases by 7%) but the molecular arrangements in the two phases are surprisingly similar.[74,135] On the basis of the scarce data that exist on this effect, and the limited number of characterised structures, it is now generally accepted that the true thermosalient phenomenon is associated with sharp phase transitions and distinctly large, anisotropic changes of the unit cell volume, tentatively related to the martensitic family of phase transitions.[135-138] A martensitic phase change is a first-order displacive solid-to-solid transition that proceeds with homogeneous lattice deformation and without atom diffusion.[136-139] These transitions progress by movement of the habit plane (the plane between the parent and product phase) driven by small cooperative movement of the atoms, while the overall chemical configuration and atomic order are preserved.

1.7. Aims

This thesis is based on applying the principles of crystal engineering in order to generate new compositions of matter through supramolecular synthesis and self-assembly. The study of the structure-property relationship of organic molecules (new and known) has remained an interesting area of research in supramolecular chemistry. This enables us to understand the mechanism or the chemistry involved and to subsequently design materials with some exotic thermal and mechanical properties, which are more often than not discovered serendipitously. The thermal and mechanical properties of molecular crystals are important due to their enormous potential applications that have remained inexhaustible and relevant in some other fields such as pharmaceuticals,[64,140,141] muscle mimetic biomaterials,[142] artificial mechanosensors,[143] molecular machinery,[144] optical devices,[145] organic electronics,[146] and smart nanomaterials,[147] and so on. So, it is important for researchers to discover or design many more of these materials to meet the huge demand. The overall aim of this thesis was to investigate the response of some organic crystals when external stimuli such as thermal/heat and mechanical stress are applied. Consequently, the goals of this PhD project are;

1) To carry out a Cambridge Structural Database search of some known materials and to synthesise new materials as well;

2) To examine the physical properties including thermal, mechanical, photo etc. of some purely organic crystals and cocrystals;

3) To investigate the structure-property relationships of these organic materials;

4) To elucidate and understand the mechanism responsible for the established structure-property relationships essential for various applications.

1.8. Thesis outline

The subsequent chapters will address the above goals.

Chapter 2 emphasises the experimental procedures utilised during this study, with details of all the instruments and computational tools.

Chapter 3 centres on the thermal expansion of a novel cocrystal (ABN.2DMABN). The volumetric thermal expansion value observed is the largest reported for an organic cocrystal to date over the temperature range of 100 to 300 K (200 K difference) and it is comparable to those obtained for purely organic compounds, hydrates, solvates etc.

Chapter 4 discusses the mechanical responsiveness of a rigid small organic molecule 4-bromobenzonitrile (4-BBN). This material displays an unusual plastic bending on its two orthogonal faces that results in helical twisting due to the presence of anisotropic interactions and packing, a rare situation in crystals of rigid small organic molecules.

Chapter 5 describes the thermal behaviour of purely organic material, 4-aminobenzonitrile (ABN). Interestingly, the crystals of ABN exhibit reversible thermosalient behaviour upon cooling due to the sudden release of the accumulated strain. Here the structural and theoretical studies reveal the role of intermolecular interactions in understanding the mechanisms that govern this phenomenon.

Chapter 6 covers the summary and concluding remarks.

1.9. References

1. Manna, A. K. *IJSR.*, **2015**, *4*, 892 – 899.

2. Rebek, J. *Angew. Chem. Int. Ed. Engl.*, **1990**, *29*, 245 – 255.

3. Vögtle, F. *Supramolecular Chemistry*; John Wiley & Sons: New York, 1991.

4. Amabilino, D. B.; Stoddart, J. F. *Chem. Rev.*, **1995**, *95*, 2715 – 2828.

5. Fyfe, M. C. T.; Stoddart, J. F. *Acc. Chem. Res.* **1997**, *30*, 393 – 401.

6. Harada, A.; Li, J.; Kamachi, M. *Nature*, **1992**, *356*, 325 – 327.

7. Harada, A.; Li, J.; Kamachi, M. *Nature*, **1994**, *370*, 126 – 128.

8. "Chemistry and Physics Nobel's Hail Discoveries on Life and Superconductors; Three Share Prize for *Synthesis of Vital Enzymes*" Harold M. Schmeck Jr. *New York Times* October 15, 1987.

9. "Nanotechnology Star Fraser Stoddart to Join Northwestern". *NewsCenter*. Northwestern University. 2007-08-16. Retrieved 2009-01-19.

10. Coskun, A.; Banaszak, M.; Astumian, R. D.; Stoddart J. F.; Grzybowski, B. A. *Chem. Soc. Rev.*, **2012**, *41*, 19 – 30.

11. Coskun, A.; Spruell, J. M.; Barin, G.; Dichtel, W. R.; Flood, A. H.; Botros, Y. Y.; Stoddart, J. F. *Chem. Soc. Rev.*, **2012**, *41*, 4827 – 4859.

12. Ballardini, R.; Balzani, V.; Credi, A.; Gandolfi, M.T.; Venturi, M. *Acc. Chem. Res.*, **2001**, *34*, 445 – 455.

13. Balzani, V.; Gomez-Lopez, M.; Stoddart, J. F. *Acc. Chem. Res.*, **1998**, *31*, 405 – 414.

14. Supramolecular Chemistry: *From Molecules to Nanomaterials*, P. A. Gale and J. W. Steed (Eds) Wiley (2012).

15. Stryer, L. *Biochemistry*; Fourth Edition edn. W. H. Freeman and Company: New York, 1995.

16. Beijer, F. H.; Kooijman, H.; Spek, A. L.; Sijbesma R. P.; Meijer, E. W. *Angew. Chem. Int. Ed.*, **1998**, *37*, 75 – 78.

17. Kauzmann, W. *Advances in Protein Chemistry*, **1959**, *14*, 1 – 63.

18. Desiraju, G. R. *The Crystal as a Supramolecular Entity in Perspectives in Supramolecular Chemistry*, 1996, Vol. 2. New York: John Wiley and Sons.

19. Desiraju, G. R. *Nat. Mater*., **2002**, *1*, 77 – 79.

20. Desiraju, G. R. *Crystal engineering, the design of organic solids*, Elsevier, Amsterdam, 1989.

21. Varshey, D. B.; Sander J. R. G.; Friščić, T. in *Supramolecular chemistry: from molecules to nanomaterials*, eds. P. A. Gale and J. W. Steed, John Wiley & Sons, Ltd., Chichester, 2012, vol. 1, pp. 9 – 24.

22. Yilmaz, M. D. *Orthogonal Supramolecular Interaction Motifs for Functional Monolayer Architectures*, Springer Theses, DOI: 10.1007/978-3-642-30257-2_2, Springer-Verlag Berlin Heidelberg, 2012.

23. Bombicz, P.; Gruber, T.; Fischer, C.; Weber, E.; Kalman, A. *CrystEngComm*, **2014**, *16*, 3646 – 3654.

24. Etter, M. C. *Acc. Chem. Res*., **1990**, *23*, 120 – 126.

25. Subramanian, S.; Zaworotko, M. J. *Coord. Chem. Rev*., **1994**, *137*, 357 – 401.

26. MacDonald, J. C.; Whitesides, G. M. *Chem. Rev.*, **1994**, *94*, 2383 – 2420.

27. Desiraju, G. R. *Angew. Chem. Int. Ed*., **2011**, *50*, 52 – 59.

28. Desiraju, G. R. *Stimulating Concepts in Chemistry*, eds. F. Vögtle, J. F. Stoddart and M. Shibasaki, Wiley-VCH, Weinheim, 2000, pp. 293.

29. Pauling, L. *J. Am. Chem. Soc.*, **1931**, *53*, 1367 – 1400.

30. Pauling, L. *The nature of the chemical bond and the structure of molecules and crystals; an introduction to modern structural chemistry*, Oxford University Press, Ithaca, NY, 1939.

31. Arunan, E.; Desiraju, G. R.; Klein, R. A.; Sadlej, J.; Scheiner, S.; Alkorta, I.; Clary, D. C.; Crabtree, R. H.; Dannenberg, J. J.; Hobza, P.; Kjaergaard, H. G.; Legon, A. C.; Mennucci, B.; Nesbitt, D. J. *Pure Appl. Chem.*, **2011**, *83*, 1637 – 1641.

32. Desiraju, G. R. in *Encyclopaedia of supramolecular chemistry*, eds. J. L. Atwood and J. W. Steed, Marcel Dekker, Inc., New York, 2004, vol. 1, pp. 658 – 665.

33. Ward, M. D. in *Molecular networks*, ed. M. W. Hosseini, Springer-Verlag, Berlin, 2009, vol. 132, pp. 1 – 23.

34. Jeffrey, G. A. *An Introduction to Hydrogen Bonding*, oxford University Press, Oxford, 1997.

35. Aakeröy C. B.; Seddon, K. R. *Chem. Soc. Rev.*, **1993**, 397 – 407.

36. *http://homepage.univie.ac.at/jeanluc.mieusset/teaching.html*.

37. Jeffrey, G. A.; Mitra, J. *J. Am. Chem. Soc.*, **1984**, *106*, 5546 – 5553.

38. Jeffrey, G. A.; Maluszynska, H. *Int. J. Biol. Macromol.*, **1982**, *4*, 173 – 185.

39. Etter, M. C. *Acc. Chem. Res.*, **1990**, *23*, 120 – 126.

40. Desiraju, G. R. *Angew. Chem. Int. Ed. Engl.*, **1995**, *34*, 2311 – 2327.

41. Chatterjee, S.; Pedireddi, V. R.; Rao, C. N. R. *Tetrahedron Lett.*, **1998**, *39*, 2843 – 2846.

42. Benesi, H. A.; Hildebrand, J. H. *J. Am. Chem. Soc.*, **1949**, *71*, 2703 – 2707.

43. Hassel, O.; Rømming, C. *Quart. Rev.*, **1962**, *16*, 1 – 18.

44. Metrangolo, P.; Neukirch, H.; Pilati, T.; Resnati, G. *Acc. Chem. Res.*, **2005**, *38*, 386 – 395.

45. Desiraju, G. R.; Ho, P. S.; Kloo, L.; Legon, A. C.; Marquardt, R.; Metrangolo, P.; Politzer, P.; Resnati, G.; Rissanen, K. *Pure Appl. Chem.*, **2013**, *35*, 1711 – 1713.

46. Cavallo, G.; Metrangolo, P.; Milani, R.; Pilati, T.; Priimagi, A.; Resnati, G.; Terraneo, G. *Chem. Rev*, **2016**, *116*, 2478 – 2601.

47. Saccone, M.; Cavallo, G.; Metrangolo, P.; Pace, A.; Pibiri, I.; Pilati, T.; Resnati, G.; Terraneo, G. *CrystEngComm*, **2013**, *15*, 3102 − 3105.

48. Politzer, P.; Murray, J. S.; Clark, T. *Phys. Chem. Chem. Phys*. **2010**, *12*, 7748 – 7757.

49. Jorgensen, W. L.; Severance, D. L. *J. Am. Chem. Soc*., **1990**, *112*, 4768 – 4774.

50. Roesky, H. W.; Andruh, M. *Coord. Chem. Rev*., **2003**, *236*, 91 – 119.

51. IUPAC. *Compendium of Chemical Terminology*, 2nd ed. (the "Gold Book"). http://goldbook.iupac.org (2006).

52. Desiraju, G. R.; Vittal, J. J. and Ramanan, A. *Crystal engineering: a textbook*, World Scientific Publishing Co. Pte. Ltd., Singapore, 2011.

53. Castleman, A. W.; Hobza, P. *Chem. Rev*., **1994**, *94*, 1721 – 1722.

54. Nesbitt, D. J. *Chem. Rev*., **1988**, *88*, 843 – 870.

55. Reddy, C. M.; Gundakaram, R. C.; Basavoju, S.; Kirchner, M. T.; Padmanabhan, K. A.; Desiraju, G. R. *Chem. Commun.*, **2005**, 3945 – 3947.

56. Desiraju, G. R. *J. Chem. Sci.*, **2010**, *122*, 667 – 675.

57. Aakeröy, C. B.; Salmon, D. J. *CrystEngComm*, **2005**, *7*, 439 – 448.

58. Aakeröy, C. B.; Panikkattu, S. P.; Chopade, D.; Desper, J. *CrystEngComm*, **2013**, *15*, 3125 – 3136.

59. Mir, N. A.; Dubey, R.; Desiraju, G. R. *IUCrJ*, **2016**, *3*, 96 – 101.

60. Brittain, H. G. *Cryst. Growth Des.*, **2012**, *12*, 5823 – 5832.

61. Qiao, N.; Li, M. Z.; Schlindwein, W.; Malek, N.; Davies, A.; Trappitt, G. *Int. J. Pharm.*, **2011**, *419*, 1 – 11.

62. Good, D. J.; Rodríguez-Hornedo, N. *Cryst. Growth Des.*, **2009**, *9*, 2252 – 2264.

63. Schultheiss, N.; Newman, A. *Cryst. Growth Des.*, **2009**, *9*, 2950 – 2967.

64. Shan, N.; Zaworotko, M. J. *Drug Discov. Today*, **2008**, *13*, 440 – 446.

65. Trask, A. V.; Motherwell, W. D. S.; Jones, W. *Int. J. Pharm.*, **2006**, *320*, 114 – 123.

66. McNamara, D. P.; Childs, S. L.; Giordano, J.; Iarriccio, A.; Cassidy, J.; Shet, M. S.; Mannion, R.; O'Donnell, E.; Park, A. *Pharm. Res.*, **2006**, *23*, 1888 – 1897.

67. Trask, A. V.; Motherwell, W. D. S.; Jones, W. *Cryst. Growth Des.*, **2005**, *5*, 1013 - 1021.

68. Bolton, O.; Kim, J. *J. Mater. Chem.*, **2007**, *17*, 1981 – 1988.

69. Del Mauro, A. D. G.; Carotenuto, M.; Venditto, V.; Petraccone, V.; Scoponi, M.; Guerra, G. *Chem. Mat.*, **2007**, *19*, 6041 – 6046.

70. Choi, E. Y.; Jazbinsek, M.; Lee, S. H.; Günter, P.; Yun, H.; Lee, S. W.; Kwon, O. P. *CrystEngComm*, **2012**, *14*, 4306 – 4311.

71. Koshima, H.; Nagano, M.; Asahi, T. *J. Am. Chem. Soc.*, **2005**, *127*, 2455 – 2463.

72. Pan, F.; Wong, M. S.; Gramlich, V.; Bosshard, C.; Günter, P. *J. Am. Chem. Soc.*, **1996**, *118*, 6315 – 6316.

73. Frankenbach, G. M.; Etter, M. C. *Chem. Mat.*, **1992**, *4*, 272 – 278.

74. Skoko, Ž.; Zamir, S.; Naumov, P.; Bernstein, J. *J. Am. Chem. Soc.*, **2010**, *132*, 14191 – 14202.

75. Chen, J.; Hu, L.; Deng, J.; Xing, X. *Chem. Soc. Rev.*, **2015**, *44*, 3522 – 3567.

76. Evans, J. S. O. *J. Chem. Soc. Dalton Trans.*, **1999**, *19*, 3317 – 3326.

77. Barrera G. D.; Bruno, J. A. O.; Barron, T. H. K.; Allan, N. L. *J. Phys Condens. Matter*, **2005**, *17*, R217 – R252.

78. Chang, R. (2000) *Physical chemistry for the chemical and biological sciences*, 3rd edn. University Science Books, Sausalito.

79. Cliffe, M. J.; Goodwin, A. L. *Appl. Crystallogr*. **2012**, *45*, 1321 – 1329.

80. Miller, W.; Smith C. W.; Mackenzie, D. S.; Evans, K.E. *J. Mater Sci*., **2009**, *44*, 5441 – 5451.

81. Krishnan, R. S.; Srinivasan, R.; Devanarayanan, S.; (1979) *Thermal expansion of crystals*. Pergamon Press Ltd., Oxford OX3 0BW, England.

82. Sleight, A. W. *Mater. Sci.*, **1998**, *28*, 29 – 43.

83. Roy, R.; Agrawal, D. K.; McKinstry, H. A. *Mater. Sci.*, **1989**, *19*, 59 – 81.

84. Lightfoot, P.; Woodcock, D. A.; Maple, M. J.; Villaescusa, L. A.; Wright, P. A. *J. Mater. Chem.*, **2001**, *11*, 212 – 216.

85. Lind, C. *Materials*, **2012**, *5*, 1125 – 1154.

86. Takenaka, K. *Sci. Technol. Adv. Mater.*, **2012**, *13*, 013001 – 013011.

87. Phillips A. E.; Goodwin, A. L.; Halder, G. J.; Southon, P. D.; Kepert, C. J. *Angew. Chem. Int. Ed*., **2008**, *47*, 1396 – 1399.

88. Sahoo, P. P.; Sumithra, S.; Madras, G.; Guru Row, T. N. *Inorg. Chem*., **2011**, *50*, 8774 – 8781.

89. Loughrey, J. J.; Comyn, T. P.; Apperley, D. C.; Little, M. A.; Halcrow, M. A. *Chem. Commun*., **2014**, *50*, 7601 – 7603.

90. Yang, C.; Wang, X.; Omary, M. A. *Angew. Chem. Int. Ed*., **2009**, *48*, 2500 – 2505.

91. Panda, M. K.; Runčevski, T.; Sahoo, S. C.; Belik, A. A.; Nath, N. K.; Dinnebier, R. E.; Naumov, P. *Nat. Commun*., **2014**, *5*, 4811 – 4818.

92. Wu, Y.; Kobayashi, A.; Halder, G. J.; Peterson, V. K.; Chapman, K. W.; Lock, N.; Southon, P. D.; Kepert, C. J. *Angew. Chem. Int. Ed*., **2008**, *47*, 8929 – 8932.

93. Wu, Y.; Peterson, V. K.; Luks, E.; Darwish, T. A.; Kepert, C. J. *Angew. Chem. Int. Ed*., **2014**, *53*, 5175 – 5178.

94. Siegrist, T.; Besnard, C.; Haas, S.; Schiltz, M.; Pattison, P.; Chernyshov, D.; Batlogg, B.; Kloc, C. *Adv. Mater*., **2007**, *19*, 2079 – 2082.

95. Wójcik, G.; Mossakowska, I. *Acta Cryst*., **2006**, *B62*, 143 – 152.

96. Drebushchak, T. N.; Boldyreva, E. V.; Mikhailenko, M. A. *J. Struct. Chem*., **2008**, *49*, 84 – 94.

97. Kitaigorodsky, A. I. *Molecular crystals and molecules*, physical chemistry series no. 29. Academic Press, New York, 1973.

98. Weigel, D.; Beguemsi, T.; Garnier, P.; Berar, J. F. *J Solid State Chem*. **1978**, *23*, 241 – 251.

99. Garnier, P.; Calvarin, G.; Weigel D. *J. Chim. Phys. Phys. Chim. Biol*. **1972**, *69*, 1711 – 1718.

100. Binoy K. Saha, *J. Indian Inst. Sci*., **2017**, *97*, 177 – 191.

101. Bhattacharya, S.; Saha B. K. *Cryst Growth Des*., **2013**, *13*, 3299 – 3302.

102. Birkedal, H.; Chargeback, D.; Pattison, P. *Angew Chem. Int. Ed*., **2002**, *41*, 754 – 756.

103. Bolotina, N. B.; Hardie, M. J.; Speer, R. L. Jr; Pinkerton A. A. *J. Appl. Cryst*., **2004**, *37*, 808 – 814.

104. Bolotina, N. B.; Zhurova, E. A.; Pinkerton, A. A. *J. Appl. Cryst*., **2003**, *36*, 280 – 285.

105. Das, D.; Jacobs, T.; Barbour, L. J. *Nat. Mater.*, **2010**, *9*, 36 – 39.

106. Das. D.; Jacobs, T.; Pietraszkob, A.; Barbour, L. J. *Chem. Commun*., **2011**, *47*, 6009 – 6011.

107. Engel, E. R.; Smith, V. J.; Bezuidenhout, C. X.; Barbour, L. J. *Chem. Commun*., **2014**, *50*, 4238 – 4241.

108. Engel, E. R.; Smith, V. J.; Bezuidenhout, C. X.; Barbour, L. J. *Chem. Mater.*, **2016**, *28*, 5073 – 5079.

109. Saraswatula, V. G.; Saha, B. K. *New J. Chem.*, **2014**, *38*, 897 – 901.

110. Hutchins, K. M.; Groeneman, R. H.; Reinheimer, E. W.; Swenson, D. C.; MacGillivray, L. R. *Chem. Sci.*, **2015**, *6*, 4717 – 4722.

111. Hutchins, K. M.; Kummer, K. A.; Groeneman, R. H.; Reinheimer, W.; Sinnwell, M. A.; Swenson, D.C.; MacGillivray, L. R. *CrystEngComm*, **2016**, *18*, 8354 – 8357.

112. Reddy, C. M.; Padmanabhan K. A.; Desiraju, G. R. *Cryst. Growth Des.*, **2006**, *6*, 2720 – 2731.

113. Reddy, C. M.; Kirchner, M. T.; Gundakaram, R. C.; Padmanabhan K. A.; Desiraju, G. R. *Chem. Eur. J.*, **2006,** *12*, 2222 – 2234.

114. Reddy, C. M.; Krishna G. R.; Ghosh, S.; *CrystEngComm*, **2010**, *12*, 2296 – 2314.

115. Desiraju, G. R.; Sarma J. A. R. P.; Krishna, T. S. R., *Chem. Phys. Lett.*, **1986**, *131*, 124 – 128.

116. Desiraju, G. R.; Harlow, R. L. *J. Am. Chem. Soc.*, **1989**, *111*, 6757 – 6764.

117. Takaki, Y.; Sasada, Y.; Watanabe, T. *Acta Crystallogr.*, **1960**, *13*, 693 – 702.

118. Ro, G.; Sorum, H. *Acta Crystallogr.*, **1972**, *B28*, 991 – 998.

119. Desiraju G. R. *Science*, **1997**, *278*, 404 – 405.

120. Castro, R. A. E.; Maria, T. M. R.; Evora, A. O. L.; Feiteira, J. C.; Silva, M. R.; Beja, A. M.; Canotilho, J.; Eusebio, M. E. S. *Cryst. Growth Des.*, **2010**, *10*, 274 – 282.

121. Brown, G. M.; Strydom, O. A. W. *Acta Crystallogr., Sect. B: Struct. Crystallogr. Cryst. Chem.*, **1974**, *30*, 801 – 804.

122. Britton, D.; Gleason, W. B. *Acta Crystallogr., Sect. B*, **1977**, *33*, 3926 – 3928.

123. Tonogaki, M.; Kawata, T.; Ohba, S.; Iwata Y.; Shibuya, I. *Acta Crystallogr.*, **1993**, *B49*, 1031 – 1039.

124. Ghosh, S.; Reddy, C. M. *Angew. Chem. Int. Ed.*, **2012**, *51*, 10319 – 10323.

125. Saha S.; Desiraju, G. R. *J. Am. Chem. Soc.*, **2017**, *139*, 1975 – 1983.

126. Bernauer, F. "*Gedrillte" Kristalle*, Gebruder Borntraeger, Berlin, 1929.

127. Shtukenberg, A. G.; Punin, Y. O.; Gujral, A.; Kahr, B. *Angew. Chem. Int. Ed.*, **2014**, *53*, 672 – 699.

128. Gigg, J.; Gigg, R.; Payne, S.; Conant, R. *J. Chem. Soc.*, **1987**, 2411 – 2414.

129. Etter, M. C.; Siedle, A. R. *J. Am. Chem. Soc.*, **1983**, *105*, 641 – 643.

130. Edwards, J. W.; Kington, G. L.; Mason, R. *Trans. Faraday Soc.*, **1960**, *56*, 660 - 667.

131. Bodenheimer, J. S.; Low, W. *Phys. Lett. A.*, **1971**, *36*, 253 – 254.

132. Naruse, M.; Sorai, M.; Sakiyama, M. *Mol. Cryst. Liq. Cryst.*, **1983**, *101*, 219 – 234.

133. Naumov, P.; Chizhik, S. A.; Panda, M. K.; Nath, N. K.; Boldyreva, E. V. *Chem. Rev.*, **2015**, *115*, 12440 – 12490.

134. Zamir, S.; Bernstein, J.; Greenwood, D. J. *Mol. Cryst. Liq. Cryst. Sci. Technol., Sect. A.*, **1994**, *242*, 193 – 200.

135. Nath, N. K.; Panda, M. K.; Sahoo, S. C.; Naumov, P. *CrystEngComm*, **2014**, *16*, 1850 – 1858.

136. Zhang, M. X.; Kelly, P. M. *Prog. Mater. Sci.*, **2009**, *54*, 1101 – 1117.

137. Bhadeshia, H. K. D. H. *Worked Examples in the Geometry of Crystals. Institute of Metals*, 2001.

138. Wayman, C. M.; Bhadeshia, H. K. D. H. *Non-diffusive Phase Transformations. In Physical Metallurgy*, 4th ed.; Cahn, R. W., Haasen, P., Eds.; Elsevier Science BV: New York, 1996; pp 1507 – 1554.

139. Ghosh, S.; Mishra, M. K.; Ganguly, S.; Desiraju, G. R. *J. Am. Chem. Soc.*, **2015**, *137*, 9912 – 9921.

140. Fleischman, S. G.; Kuduva, S. S; McMahon, J. A; Moulton, B; Walsh, R. D. B; Rodriguez-Hornedo, N.; Zaworotko, M. J. *Cryst. Growth Des*., **2003**, *3*, 909 – 919.

141. Brittain, H. G. *Cryst. Growth Des*., **2012**, *12*, 5823 – 5832.

142. Commins, P.; Desta, I. T.; Karothu, D. P.; Panda, M. K.; Naumov, P. *Chem. Commun*., **2016**, *52*, 13941 – 13954.

143. Naumov, P.; Chizhik, S.; Panda, M. K.; Nath, N. K.; Boldyreva, E. Chem. Rev., 2015, *115*, 12440 – 12490.

144. Kinbara, K.; Aida, T. *Chem. Rev*., **2005**, *105*, 1377 − 1400.

145. Kahn, O. *Curr. Opin. Solid State Mater. Sci*., **1996**, *1*, 547 – 554.

146. Horiuchi, S.; Hasegawa, T.; Tokura, Y. *J. Phys. Soc. Jpn*., **2006**, *75*, 051016 – 051029.

147. Burgert, I.; Fratzl, P. *Philos. Trans. R. Soc. A.*, **2009**, *367*, 1541 − 1557.

Chapter 2: Experimental Techniques

2.1. Crystallisation

4-aminobenzonitrile (ABN), 4-(dimethylamino)benzonitrile (DMABN) and 4-bromobenzonitrile (4-BBN) were purchased from Sigma Aldrich and used without further purification.

ABN·2DMABN cocrystal was synthesised according to the procedure described in Chapter 3 of this thesis. All other chemical reagents were obtained from commercial sources.

2.1.1. Crystallisation by slow evaporation

Slow evaporation is a very common crystallisation technique. It is used to prepare molecular as well as multi-component crystals. Typically, a concentrated solution of the anticipated compound or mixture of components is prepared. The solution is then filtered and allowed to evaporate slowly at room temperature. The rate of crystallisation can be controlled by modifying the concentration of the solution, as well as the temperature at which the solution is kept.

2.1.2. Crystallisation by sublimation

Sublimation is another method of crystallisation which involves the heating of solid materials at a temperature just below their melting points. This can be carried out using different apparatus such as cold finger, glass oven etc. Figure 2.1 is the glass oven connected to vacuum pump (0.02 mbar) which is also attached to the cold trap used for sublimation.

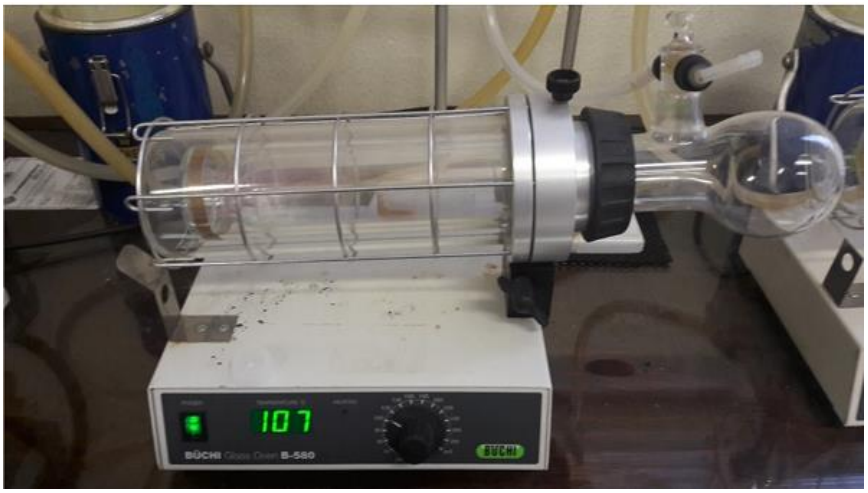

Figure 2.1. Photograph of the glass oven.

Here a known amount of the sample was placed in a glass weighing boat (Figure 2.2) and covered slightly with a glass slide. This was then carefully placed in the glass oven which is already connected to the vacuum pump and allowed for sublimation at a specific temperature depending on the melting point of the sample under investigation.

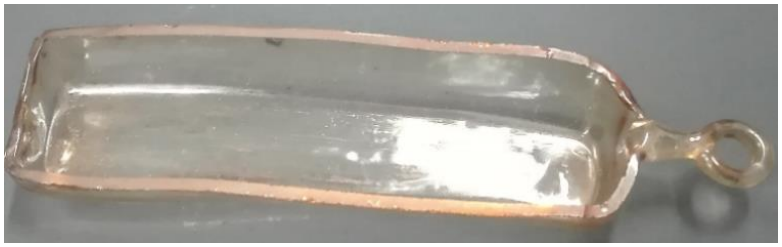

Figure 2.2. Photograph of the glass weighing boat for the sublimation.

2.2. Single-crystal X-ray diffraction

Intensity data were collected using two different diffractometers: a Bruker APEX-II DUO and a Bruker D8 Venture. The APEX-II DUO employs a multilayer monochromator with MoKα radiation (λ = 0.71073 Å) from an Incoatec IμS microfocus source and CCD area-detector. The diffractometer is equipped with an Oxford Cryosystems Cryostream 700Plus cryostat supplied with liquid nitrogen. The D8 Venture with Photon II CPAD detector also employs a multilayer monochromator with MoKα radiation (λ = 0.71073 Å) from an Incoatec IμS microfocus source. It is equipped with an Oxford Cryosystems Cryostream 800Plus cryostat supplied with liquid nitrogen.

Data reduction was carried out by means of a standard procedure using the Bruker software package SAINT[1] and the absorption corrections and the correction of other systematic errors were performed using SADABS.[2] The structures were solved by direct methods using SHELXS-2016 and refined using SHELXL-2016.[3] X-Seed[4] was used as the graphical interface for the SHELX program suite. Hydrogen atoms were placed in calculated positions using riding models. In the case of ABN, since there is no standard model for amine hydrogen atoms, these atoms were identified in difference electron density maps and refined with an N–H bond-length restraint of 1.02(2) Å (based on a survey of the CSD where structures were determined by means of neutron diffraction).

2.3. Powder X-ray diffraction

Routine powder X-ray diffraction (PXRD) data were collected using a Bruker D2 PHASER equipped with a Lynxeye 1D detector and Ni-filtered Cu Kα radiation (λ = 1.5418 Å; 30 kV, 10 mA generator parameters; restricted by a 1.0 mm divergence slit and a 2.5 Soller collimator).

Variable-temperature PXRD experiments were carried out using Cu Kα radiation (λ = 1.5418 Å, 40 kV and 30 mA) on a PANalytical X'pert PRO instrument operating in Bragg-Brentano geometry. Intensity data were recorded using an X'Celerator detector, and 2θ scans in the range of 5–40° were performed with a step size of 0.02° at a scan speed of 0.02 (°/s). The sample was sealed within a glass capillary and the capillary spinner configuration (with focusing mirror) of the instrument was used since the setup allows for very accurate temperature control using a short-nozzle Oxford Cryosystems Cryostream 700Plus cryostat. Data were recorded from 300 to 100 K at 20 K intervals for some of the samples investigated. TOPAS[5] version 4.2 was also used for Pawley refinement where required.

2.4. Hot stage microscopy

The thermal behaviour of the crystals was observed using a Linkam DSC-600 equipped with a Meiji MS-45D Unicam zoom macroscope and a PixelLink digital camera. A single crystal of all the samples (ABN.2DMABN, 4-BBN and ABN) was cooled from 300 to 100 K and then heated back to 300 K at a constant rate of 5 K min^{-1}.

2.5. Differential scanning calorimetric analysis

The two instruments used for differential scanning calorimetry (DSC) were a TA Instruments Q100 with Liquid Nitrogen Cooling Accessory (LNCS) and a TA Instruments Q20 with Refrigerated Cooling System (RCS90). The former has a minimum operating temperature of 93 K while the latter is limited to a minimum of 183 K. Both instruments measure heat flow to and from a sample pan, relative to a reference pan, as a function of temperature. DSC thermograms will display thermal events as endothermic and exothermic peaks. The pans are standard aluminium pans supplied by TA Instruments. Typically, a sample of 0.5–6 mg was subjected to a temperature ramp rate of 5 K min^{-1}. Experiments were conducted under constant purge of dry nitrogen gas at a flow rate of 50 ml min^{-1}.

2.6. Fourier transform infrared

IR adsorption spectra were recorded using Bruker alpha P ATR-IR. A background scan was collected immediately before the sample scan.

2.7. PASCal

The programme PASCal[6] (Principal Axis Strain Calculator) was accessed at http://pascal.chem.ox.ac.uk. It is used to determine a set of principal axes and calculates linear and volumetric coefficients of thermal expansion. The thermal expansion coefficients were calculated from the lattice parameters obtained from variable temperature single-crystal diffraction data collected for all the materials examined.

2.8. Hirshfeld surface analysis

The program CrystalExplorer[7] (Version 3.1) was used to generate Hirshfeld surfaces (d_{norm}) for the crystal structures of some materials used during the study.

2.9. Materials Studio

Biovia Materials Studio is a modelling and simulation program well suited for the study of crystalline materials that enhances the prediction and understanding of the structure-property relationships of a material.[8]

Refined single-crystal X-ray structures were used along with the Morphology module within the Biovia Materials Studio 7.0 software suite[8] to simulate the crystal habit. The crystal structure was then overlaid with the crystal habit to correlate the packing arrangement responsible for bending within the crystal to crystal faces/facets.

DMol^3 is an all-electron numerical method for solving density functional theory (DFT) to model the electronic structures and energetics of molecules, solids, and surfaces.[9,10] In this work, periodic H-atom position was optimised in DMol^3 and was used to perform single-point energy calculations. Forcite is a collection of molecular mechanics and dynamics tools for the investigation of a wide range of systems across various time scales.

2.10. References

1. *SAINT Data Reduction Software*, Version 6.45; Bruker AXS Inc.: Madison, WI, 2003.

2. *SADABS*, Version 2.05; Bruker AXS Inc.: Madison, WI, 2002.

3. Sheldrick, G. M. *A Short History of SHELX*. *Acta Crystallogr*. **2008**, A*64*, 112 – 122.

4. Barbour, L. J. *Supramol. Chem.* **2001**, *1*,189 – 191.

5. *TOPAS, V4.2, General Profile and Structure Analysis Software for Powder Diffraction Data Users' Manual*; Bruker, AXS: Karlsruhe, 2009

6. Cliffe, M. J.; Goodwin, A. L. *J. Appl. Crystallogr*. **2012**, *45*, 1321 – 1329.

7. Spackman, M.A.; Jayatilaka, D. *CrystEngComm*, **2009**, *11* ,19 – 32.

8. *Dassault Systèmes BIOVIA Materials Studio*, Release 18, San Diego: Dassault Systèmes, 2017.

9. Delley, B. *J. Chem. Phys*., **1990**, *92*, 508 – 517.

10. Delley, B. *J. Chem. Phys*., **2000**, *113*, 7756 – 7764.

Chapter 3: Large volumetric thermal expansion of a novel cocrystal over a wide temperature range

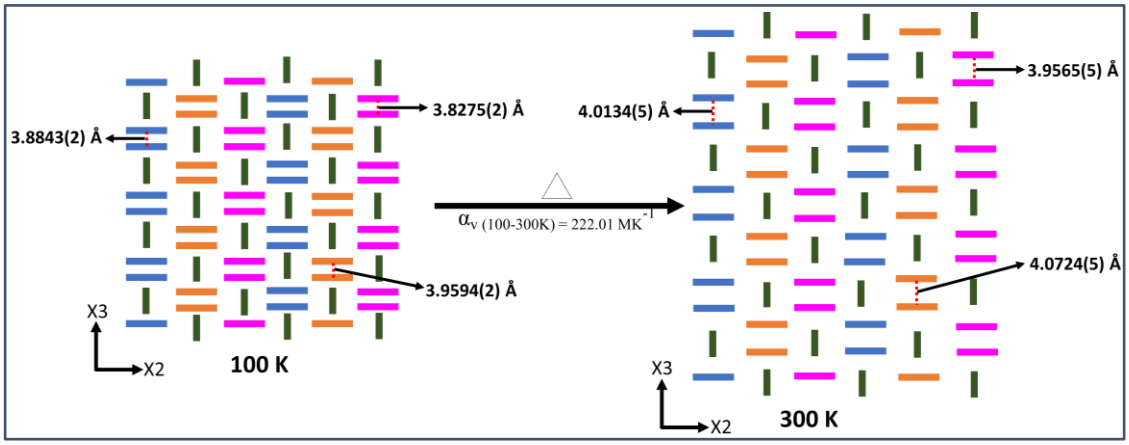

3.1. Communication in crystal engineering communications (Published)

Contributions of the main author:

- Design of the project
- Preparation of the cocrystals
- Collection of variable-temperature single-crystal X-ray data
- Solution and refinement of single-crystal X-ray structures
- Determination of principal axes and thermal expansion coefficients
- Recording of PXRD patterns
- Recording of Hot stage micrographs
- Recording of DSC thermograms
- Interpretation of results with Dr Prem Lama and Dr Vincent J. Smith
- Writing the first draft of the article

CrystEngComm

PAPER

Cite this: *CrystEngComm*, 2018, **20**, 631

Received 23rd October 2017,
Accepted 5th January 2018

DOI: 10.1039/c7ce01848g

rsc.li/crystengcomm

Large volumetric thermal expansion of a novel organic cocrystal over a wide temperature range†

Lukman O. Alimi, Prem Lama, Vincent J. Smith ‡ and Leonard J. Barbour *

An organic cocrystal consisting of 4-aminobenzonitrile and 4-(dimethylamino) benzonitrile (**ABN-2DMABN**) undergoes positive linear thermal expansion along its three principal axes over the temperature range 100–300 K. The associated volumetric thermal expansion coefficient is the largest reported to date for a cocrystal in the wide temperature range investigated.

We are interested in crystalline solids with tuneable thermal expansion behaviour[1] since this property can potentially be exploited for the design of thermomechanical actuators, sensors and composites.[2] The relatively modest thermal expansion experienced by most materials on heating is usually due to increasing anharmonic vibrational amplitudes of the constituent atoms, ions, or molecules.[3] However, thermal expansion due to other factors has been reported for several different types of materials. For example, we have shown that the purely organic material (*S*,*S*)-octa-3,5-diyn-2,7-diol[2a] undergoes exceptionally large positive (515 MK^{-1}) and negative (−204 MK^{-1}) anisotropic thermal expansion. More recently we reported large uniaxial NTE and large biaxial PTE of the inclusion compound 18-crown-6-nitromethane.[4] Notably, this material also displays exceptionally large volumetric thermal expansion (α_V = 378 × MK^{-1}) over the temperature range 180–273 K.[4b] Other types of materials that have been shown to experience anomalous thermal expansion behaviour include inorganic salts,[5] inclusion compounds,[4] cocrystals[1] and coordination polymers (including metal–organic frameworks).[6,7] A cocrystal is a solid composed of two or more molecular components associated by non-covalent interactions to form a periodic material with distinct properties.[8] Cocrystal research is relevant to pharmaceutical[8] and energetic[9] materials and is also poised to make significant contributions to other areas of interest such as non-linear optics,[10] ferroelectric[11] and organic electronic materials.[12] However, relatively few studies of the thermal expansion properties of cocrystals have been reported to date.[8]

Merlino *et al.* reported a comparison of the crystal structure of ABN[13] (Scheme 1a) with that of its 3-aminobenzonitrile analogue.[13a] In a separate study, Heine *et al.* reported the phase transition of ABN from monoclinic to orthorhombic upon cooling from 293 to 255 K when investigating the crystal structure at various temperatures.[14a] Another article by Islor *et al.* describes the crystal structure of ABN determined at 200 K after rapid cooling from room temperature.[13b] They did not observe the phase transition reported by Heine *et al.* and suggested that the process of rapid cooling could have preserved the monoclinic phase observed at 293 K.

Heine *et al.* also reported the crystal structures of DMABN[14] (Scheme 1b) at various temperatures and revealed that the material undergoes a solid–solid phase transition upon cooling. However, they could not elucidate the nature of the phase transition due to their failure to grow crystals at temperatures below the transition.[14a] Subsequently, Jameson *et al.* reported the low-temperature (LT) crystal structure of DMABN and compared it to that of the high-temperature (HT) phase.[14b] They revealed that the LT phase has dramatically different unit cell dimensions as compared to the HT phase, even though the two forms have the same space group. Since the crystals of these two chemically related compounds have shown interesting structural responses to

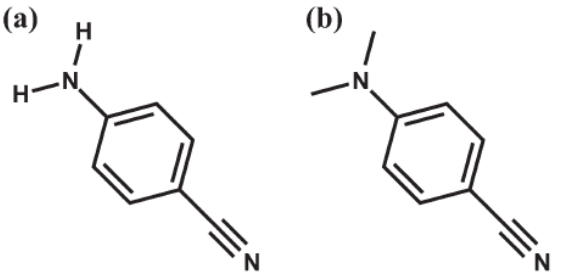

Scheme 1 Chemical structures of (a) 4-aminobenzonitrile (ABN) and (b) 4-(dimethylamino)benzonitrile (DMABN).

Department of Chemistry and Polymer Science, University of Stellenbosch, Matieland, 7602, South Africa. E-mail: ljb@sun.ac.za

† Electronic supplementary information (ESI) available. Crystallographic information files CCDC 1555122–1555132, experimental methods, PXRD, hot stage microscopy images, DSC, thermal expansion coefficients and intermolecular interaction details. For ESI and crystallographic data in CIF or other electronic format see DOI: 10.1039/c7ce01848g

‡ Current address: Department of Chemistry, Rhodes University, Grahamstown, 6140, South Africa. E-mail: v.smith@ru.ac.za.

temperature, we decided to investigate the thermal behaviour of their cocrystal form.

In an attempt to grow cocrystals of ABN and DMABN, the two compounds were co-dissolved in acetone at different molar ratios (1 : 1, 2 : 1, 1 : 2, respectively), and each solution was allowed to evaporate slowly over a period of several days. Both single crystals and polycrystalline material were obtained from the 1 : 1 mixture. The 1 : 2 mixture yielded only single crystals while the 2 : 1 mixture produced only polycrystalline material. Two crystals were harvested from the 1 : 1 mixture and subjected to single-crystal X-ray diffraction (SCXRD) analysis; in both cases the crystal structure was that of a 1 : 2 cocrystal of ABN and DMABN. A crystal harvested from the 1 : 2 mixture yielded the same structure (hereafter referred to as **ABN·2DMABN**). Visual comparison of the simulated PXRD pattern for **ABN·2DMABN** with that recorded for the product of the 1 : 2 mixture indicates that these two materials have the same crystal structure (Fig. S1 ESI†) – *i.e.* phase purity of the crystals harvested from the 1 : 2 mixture. From the abovementioned experiments, we conclude that the formation of a 1 : 2 adduct is the most favourable cocrystal form for the three ABN : DMABN molar ratios tested.

The cocrystal **ABN·2DMABN** packs in the space group $P2_1/n$, with two molecules of ABN and four molecules of DMABN in the asymmetric unit (Scheme S1 ESI†). SCXRD analysis was first carried out at 300 K, and then repeated at 100 K. Comparison of packing modes suggests that no phase change occurs in this temperature range, but that the volumetric thermal expansion coefficient appears to be unusually large. Hot stage microscopy (Fig. S2 ESI†) and differential scanning calorimetry (Fig. S3 ESI†) were also carried out over the same temperature range; no discernible change in the appearance of the crystals was observed and no energetic events were recorded. In order to carry out a detailed investigation of the thermal expansion behaviour of **ABN·2DMABN**, additional SCXRD data were recorded at 20 K intervals in the range 100 to 300 K (Tables S1 and S2 ESI†). Since **ABN·2DMABN** crystallises in the monoclinic system, the program PASCal[15] was used to determine the linear and volumetric thermal expansion coefficients. As is usual for most crystalline materials, the crystal undergoes positive linear thermal expansion in all three directions. The coefficients of thermal expansion along the principal axes *X*1 (0.9936, 0.0, 0.1131), *X*2 (0.0499, 0.0, 0.9988) and *X*3 (0.0, 1.0, 0.0) are α_{X1} = 24.3, α_{X2} = 90.9 and α_{X3} = 105.0 MK^{-1}, respectively (Fig. 1). The volumetric thermal expansion coefficient (α_V = 222 MK^{-1}) represents an increase of approximately 4.4% in the overall volume of the material (Fig. 2) during heating from 100 to 300 K.

Over the temperature range investigated, the principal axis *X*1 experiences the smallest increase (0.45%) in length with heating, while substantially larger increases are observed for *X*2 (1.82%) and *X*3 (2.14%). The volumetric thermal expansion coefficient (222 MK^{-1}) recorded for **ABN·2DMABN** over the temperature range 100–300 K is similar to other large α_V values reported for organic multicomponent crystals over a relatively narrow temperature range (Table 1; we note that very few such coefficients have been reported to date for cocrystals). However,

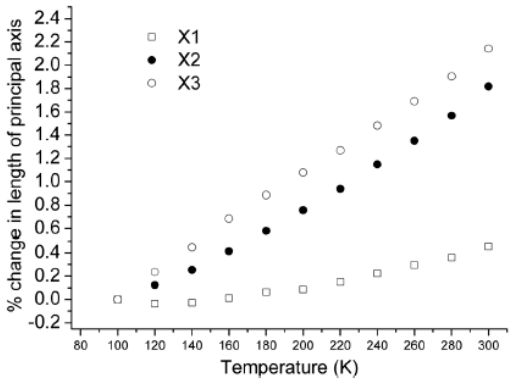

Fig. 1 Percentage changes in principal axis lengths of **ABN·2DMABN** in the temperature range 100–300 K (relative to the parameters recorded at 100 K).

it is also important to note that the volumetric thermal expansion coefficient observed for the cocrystal **ABN·2DMABN** in this study is over a relatively wide temperature range (100–300 K). Bhattacharya *et al.* reported an overall volumetric expansion coefficient of 183 MK^{-1} for a monoclinic form of the cocrystal **CBTA·BPE** and 158 MK^{-1} for the triclinic form over the temperature range of 120–298 K.[16] Hutchins *et al.* recently reported coefficients of 229 MK^{-1} (260–290 K) for the cocrystal **2(4PAzP)·(4,6-diCl res)** and 249 MK^{-1} (170–250 K) for the cocrystal **2(4PAzP)·(4,6-diBr res)**.[1a] In a separate article, the same group reported volumetric coefficients of 185, 181 and 196 MK^{-1}, respectively, for cocrystals **2(4,6-diX res)·2(4,4′-AP)** (where: X = Cl, Br, and I) over the temperature range 190–290 K.[1a] For comparison, the volumetric thermal expansion coefficients of **ABN·2DMABN** over the truncated temperature ranges of 200–300, 220–300, 240–300 and 260–300 K are 245 MK^{-1}, 251 MK^{-1}, 254 $MK^{-1}$and 262 MK^{-1}, respectively (Tables S3 and S4 ESI†). These values are significantly higher than that calculated over the full temperature range of 100–300 K.

To elucidate the mechanism responsible for the large volumetric thermal expansion coefficient of **ABN·2DMABN**, all of the crystal structures were analysed carefully. The largest

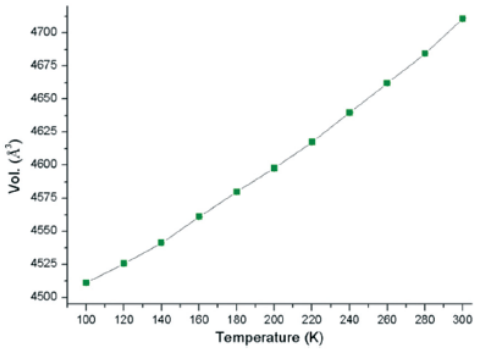

Fig. 2 Variation in unit cell volume of **ABN·2DMABN** with temperature.

Table 1 Large volumetric thermal expansion coefficients (α_v) reported for some multicomponent organic materials

		Temperature range (K)	α_v (MK^{-1})	Ref.
Cocrystals	ABN·2DMABN (present study)	100–300	222	—
	4PAzP·(4,6-diCl res)	260–290	229	1*a*
	4PAzP·(4,6-diBr res)	170–250	249	1*a*
Purely organic	Pyridine·IBr	110–298	226	18
	$HOOC(CH_2)_3COOH$	120–298	264	25*b*
	$HOOC(CH_2)_4COOH$	140–298	228	25*b*
	$HOOC(CH_2)_5COOH$	180–298	283	25*b*
	$HOOC(CH_2)_7COOH$	120–298	261	25*b*
	2-Butynoic acid (0D)	118–226	332	19
	2-Butynoic acid (1D)	118–298	265	19
	4,4′-Methylenebis(2,6-dimethylaniline) (MBDA)	148–298	235	20
	4-Azopyridine (4,4′-AP)	210–250	312	1*b*
Hydrates	Methanol monohydrate	4.2–160 (max. at 155 K)	494	21
	$(C_6H_{12}N_2)$ $HCl·3H_2O$	270–300	−386	22
Solvates	18C6·Nitromethane	90–273	311	4*a*
	18C6·Nitromethane	180–273	378	4*b*
	18C6·Acetonitrile	180–273	226	4*b*
	18C6·Iodomethane	180–273	256	4*b*
	1,1,4,4-Tetrakis(4-hydroxyphenyl)-cyclohexane ·phenol	108–298	228	23

positive linear thermal expansion coefficient, α_{X3} (105 MK^{-1}) is collinear with the crystallographic *b* axis, and it is therefore useful to evaluate the intermolecular interactions that propagate predominantly in this direction. There are three crystallographically unique π···π interactions approximately along *X*3 (i1···i2, i3···i3 and i4···i4, where i1–i4 are the centroids of C26 → C31, C42 → C47, C1 → C6 and C17 → C22, respectively. There are also four different C–H···π interactions (C–H···i1, C–H···i2, C–H···i3 and C–H···i4) that propagate in the same direction. All of these intermolecular interaction distances increase with an increase in temperature from 100 to 300 K (Fig. 3, S4 and S5 and Table S5 ESI†), thus accounting for the colossal positive linear thermal expansion coefficient along *X*3. This increase is due to increased parallel/longitudinal motion/vibration within the molecules with an increase in temperature (Fig. S6 and Movie S1 ESI†).[17]

The principal axis *X*2, which is approximately collinear with the crystallographic *c* axis, has a thermal expansion coefficient of *ca.* 91 MK^{-1}. Several weak C–H···π interactions propagate along *X*2; these are between C8–H8C, C24–H24C, C25–H25B and the centroid i5 (i5 = C35 → C40) of the phenyl ring (Table S6 ESI†).

The C–H···π interaction distances along *X*2 increase with an increase in temperature and result in the observed thermal expansion along this direction (Fig. 4 and Fig. S7 ESI†). We propose that the considerably smaller thermal expansion coefficient α_{X1} is due to the presence of strong three-centre bifurcated[24] N–H···N hydrogen bonding interactions that occur parallel to the crystallographic *a* axis, which primarily influences *X*1.

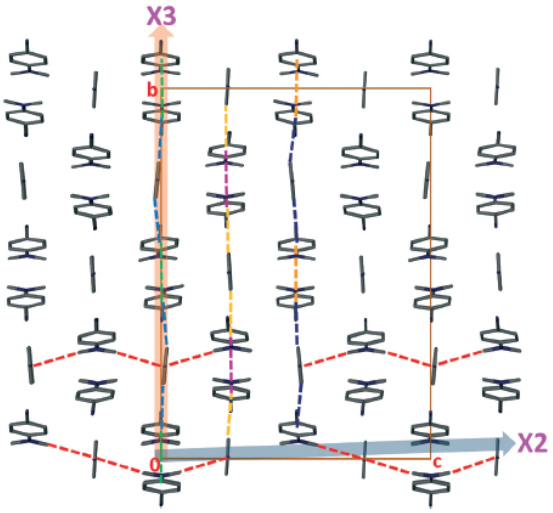

Fig. 3 A packing diagram of ABN·2DMABN showing both π···π (green, purple and orange) and C–H···π (grey, yellow and blue) interactions along the principal axis *X*3, only C–H···π (red) interactions are evident along *X*2 axis (hydrogen atoms are omitted for clarity).

These hydrogen bonds involve the amine moiety of an ABN molecule and the nitrogen atom of the nitrile moiety of a second ABN molecule; both of the hydrogen atoms of the amine moiety are hydrogen bonded to the nitrile moiety. A second set of hydrogen bonds is formed between an amine moiety of the ABN molecule and the nitrile moieties of two different molecules of DMABN. That is, the amine moiety of a single molecule of ABN forms four hydrogen bonds with three different molecules simultaneously with only one hydrogen bond donor group ($-NH_2$) and three different hydrogen bond acceptors (–CN groups) involved (Fig. 5 and S8 ESI†) (two bifurcated donors and one bifurcated acceptor). Thus, owing to the hydrogen bonding interactions (*i.e.* stronger interactions in comparison to the relatively weaker interactions propagating along the other two directions) (D···A = 3.259(4) to 3.370(5) Å, D–H···A = 160.22(17) to 168.33(17)°)

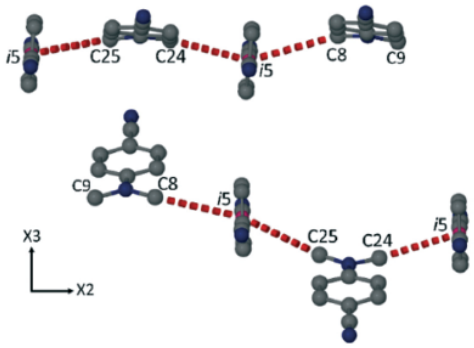

Fig. 4 Perspective view showing non-covalent interactions along the principal axis *X*2 (hydrogen atoms are omitted for clarity).

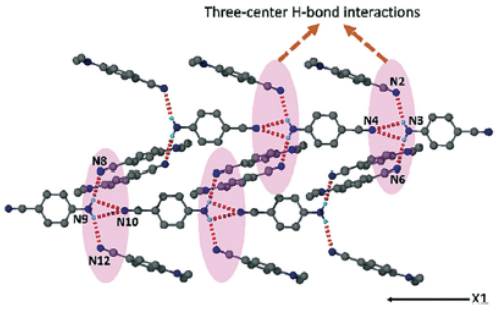

Fig. 5 Packing arrangement of ABN·2DMABN showing the three-centre "bifurcated" N–H···N hydrogen bonding interactions along the principal axis *X*1.

along *X*1, the packing arrangement along *X*1 remains almost unchanged (Tables S7–S9 ESI†) and results in the modest thermal expansion observed along *X*1. It is well known that the directions along which hydrogen bonds or other intermolecular interactions occur usually experience very small or even negative thermal expansion owing to the presence of liberation/transverse vibration effects, while the directions in which the interactions are weak exhibit large thermal expansion.[25,26]

The thermal expansion behaviour of the organic cocrystal **ABN·2DMABN** has been explored; the material undergoes positive linear thermal expansion when heated from 100 to 300 K without any evidence of a phase transition. The combined effects and the directionality of all the intermolecular interactions lead to distinct positive linear thermal expansion coefficients along *X*1, *X*2 and *X*3. This results in large volumetric thermal expansion of the cocrystal over this wide temperature range. Our findings imply that understanding the intermolecular interactions between molecules using cocrystallisation could be helpful in the design of new solid materials with the desired thermal expansion properties.

Conflicts of interest

There are no conflicts to declare.

Acknowledgements

We thank the National Research Foundation, the Department of Science and Technology (SARCHI Program) and Stellenbosch University for financial support. LOA and PL also acknowledge UMYU (TETFund) and the Claude Leon Foundation, respectively, for financial support.

Notes and references

1 (*a*) K. M. Hutchins, R. H. Groeneman, E. W. Reinheimer, D. C. Swenson and L. R. MacGillivray, *Chem. Sci.*, 2015, 6, 4717; (*b*) K. M. Hutchins, K. A. Kummer, R. H. Groeneman, E. W. Reinheimer, M. A. Sinnwell, D. C. Swensona and L. R. MacGillivray, *CrystEngComm*, 2016, 18, 8354.

2 (*a*) D. Das, T. Jacobs and L. J. Barbour, *Nat. Mater.*, 2010, 9, 36; (*b*) T. A. V. Khuong, J. E. Nunez, C. E. Godinez and M. A. Garcia-Garibay, *Acc. Chem. Res.*, 2006, 39, 413; (*c*) A. L. Goodwin, M. Calleja, M. J. Conterio, M. T. Dove, J. S. O. Evans, D. A. Keen, L. Peters and M. G. Tucker, *Science*, 2008, 319, 794.

3 N. W. Ashcroft and N. D. Merwin, *Solid State Physics*, Holt, Rinehart & Winston, 1976.

4 (*a*) E. R. Engel, V. J. Smith, C. X. Bezuidenhout and L. J. Barbour, *Chem. Commun.*, 2014, 50, 4238; (*b*) E. R. Engel, V. J. Smith, C. X. Bezuidenhout and L. J. Barbour, *Chem. Mater.*, 2016, 28, 5073.

5 T. Matsuda, J. E. Kim, K. Ohoyama and Y. Yoritomo, *Phys. Rev. B: Condens. Matter Mater. Phys.*, 2009, 79, 172302.

6 P. Lama, L. O. Alimi, R. K. Das and L. J. Barbour, *Chem. Commun.*, 2016, 52, 3231.

7 (*a*) V. K. Peterson, G. J. Kearly, Y. Wu, A. J. Ramirez-Cuesta, E. Kemner and C. J. Kepert, *Angew. Chem., Int. Ed.*, 2010, 49, 585; (*b*) Y. Wu, A. Kobayashi, G. J. Halder, V. K. Peterson, K. W. Chapman, N. Lock, P. D. Southon and C. J. Kepert, *Angew. Chem.*, 2008, 120, 9061.

8 (*a*) S. G. Fleischman, S. S. Kuduva, J. A. McMoulton, R. D. B. Walsh, N. Rodriguez-Hornedo and M. J. Zaworotko, *Cryst. Growth Des.*, 2003, 3, 909; (*b*) A. V. Trask, W. D. S. Motherwell and W. Jones, *Cryst. Growth Des.*, 2005, 5, 1013; (*c*) N. Shan and M. J. Brittain, *Cryst. Growth Des.*, 2012, 12, 5823.

9 (*a*) K. B. Landenberger and A. J. Matzger, *Cryst. Growth Des.*, 2010, 10, 5341; (*b*) V. Thottempudi and J. M. Shreeve, *J. Am. Chem. Soc.*, 2011, 133, 19982; (*c*) D. I. A. Millar, H. E. Maynard- Casely, D. R. Allan, A. S. Cumming, A. R. Lennie, A. J. Mackay, I. D. H. Oswald, C. C. Tang and C. R. Pulham, *CrystEngComm*, 2012, 14, 3742; (*d*) K. B. Landenberger and A. J. Matzger, *Cryst. Growth Des.*, 2012, 12, 3603.

10 (*a*) S. R. Marder, J. W. Perry and W. P. Schaefer, *Science*, 1989, 245, 626; (*b*) F. Pan, M. S. Wong, V. Gramlich, C. Bosshard and P. Gunter, *J. Am. Chem. Soc.*, 1996, 118, 6315; (*c*) E. Y. Choi, M. Jazbinsek, S. H. Lee, P. Gunter, H. Yun, S. W. Lee and O. P. Kwon, *CrystEngComm*, 2012, 14, 4306.

11 (*a*) S. Horiuchi and Y. Tokura, *Nat. Mater.*, 2008, 7, 357; (*b*) A. S. Tayi, A. K. Shveyd, A. C. H. Sue, J. M. Szarko, B. S. Rolczynski, D. Cao, T. J. Kennedy, A. A. Sarjeant, C. L. Stern, W. F. Paxton, W. Wu, S. K. Dey, A. C. Fahrenbach, J. R. Guest, H. Mohseni, L. X. Chen, K. L. Wang, J. F. Stoddart and S. I. Stupp, *Nature*, 2012, 488, 485.

12 (*a*) S. Horiuchi, T. Hasegawa and Y. Tokura, *J. Phys. Soc. Jpn.*, 2006, 75, 051016; (*b*) L. Zhu, L. Yi, L. Li, L. Kim, L. Coropceanu and L. Bredas, *J. Am. Chem. Soc.*, 2012, 134, 2340.

13 (*a*) S. Merlino and F. Sartori, *Acta Crystallogr., Sect. B: Struct. Crystallogr. Cryst. Chem.*, 1982, 38, 1476; (*b*) A. M. Islor, B. Chandrakantha, T. Gerber, E. Hosten and R. Betz, *Z. Kristallogr. – Cryst. Mater.*, 2013, 228, 217; (*c*) G. Smith, R. C. Bott and D. E. Lynch, *Acta Crystallogr., Sect. C: Cryst. Struct. Commun.*, 2000, 56, 1155.

14 (*a*) A. Heine, R. Herbst-Irmer, D. Stalke, W. Kuhnle and K. A. Zachariasse, *Acta Crystallogr., Sect. B: Struct. Sci.*, 1994, 50, 363; (*b*) G. B. Jameson, B. M. Sheikh-Ali and R. G. Weiss, *Acta Crystallogr., Sect. B: Struct. Sci.*, 1994, 50, 703.
15 J. Cliffe and A. L. Goodwin, *J. Appl. Crystallogr.*, 2012, 45, 1321.
16 S. Bhattacharya and B. K. Saha, *Cryst. Growth Des.*, 2013, 13, 3299.
17 (*a*) Y. K. Godovskiy, *Thermophysics of Polymer*, 1982, Moscow; (*b*) H. Aggarwal, R. K. Das, E. R. Engel and L. J. Barbour, *Chem. Commun.*, 2017, 53, 861.
18 R. H. Jones, K. S. Knight, W. G. Marshall, J. Clews, R. J. Darton, D. Pyatt, S. J. Coles and P. N. Horton, *CrystEngComm*, 2014, 16, 237.
19 V. G. Saraswatula, S. Bhattacharya and B. K. Saha, *New J. Chem.*, 2015, 39, 3345.
20 S. Bhattacharya and B. K. Saha, *CrystEngComm*, 2014, 16, 2340.
21 D. Fortes, E. Suard and K. S. Knight, *Science*, 2011, 331, 742.
22 M. Szafranski, *J. Mater. Chem. C*, 2013, 1, 7904.
23 V. G. Saraswatula and B. K. Saha, *Cryst. Growth Des.*, 2015, 15, 593.
24 (*a*) G. A. Jeffrey and J. Mitra, *J. Am. Chem. Soc.*, 1984, 106, 5546; (*b*) G. A. Jeffrey and H. Maluszynska, *Int. J. Biol. Macromol.*, 1982, 4, 173.
25 (*a*) A. I. Kitaigorodsky, In *Molecular Crystals and Molecules Physical Chemistry Series No. 29*; ed. E. M. Loebl, Academic Press, New York, 1973; (*b*) S. Bhattacharya, V. G. Saraswatula and B. K. Saha, *Cryst. Growth Des.*, 2013, 13, 3651; (*c*) J. Salud, M. Barro, D. O. Lopéz, J. L. Tamarit and X. Alcobé, *J. Appl. Crystallogr.*, 1998, 31, 748.
26 C. M. Reddy, G. R. Krishna and S. Ghosh, *CrystEngComm*, 2010, 12, 2296.

3.2. Supporting Information

Large volumetric thermal expansion for a novel organic cocrystal over a wide temperature range.

Lukman O. Alimi, Prem Lama, Vincent J. Smith and Leonard J. Barbour*

Materials

The 4-aminobenzonitrile (ABN) and 4-(dimethylamino)benzonitrile (DMABN) used in the preparation of **ABN·2DMABN** cocrystal were purchased from Sigma-Aldrich and used without further purification.

Preparation of ABN·2DMABN cocrystal:

Method 1

Cocrystals were obtained by dissolving ABN (59.07 mg, 0.5 mmol) and DMABN (146.19 mg, 1.0 mmol) in 1ml of acetone. Slow evaporation over several days yielded single crystals suitable for X-ray diffraction.

Method 2

The mechanochemical method was also used for cocrystallisation. ABN (100 mg, 0.85 mmol) was ground with DMABN (248.5 mg, 1.7 mmol) in a pre-washed and dried agate mortar and pestle. The combination was ground for 2 h; the formation of the new materials was monitored by periodically measuring the PXRD pattern until a new pattern emerged. Cocrystals were obtained by dissolving (20 mg, 0.049 mmol) of ground materials in 1ml of acetone. Slow evaporation over 5-7 days yielded single crystals suitable for X-ray diffraction.

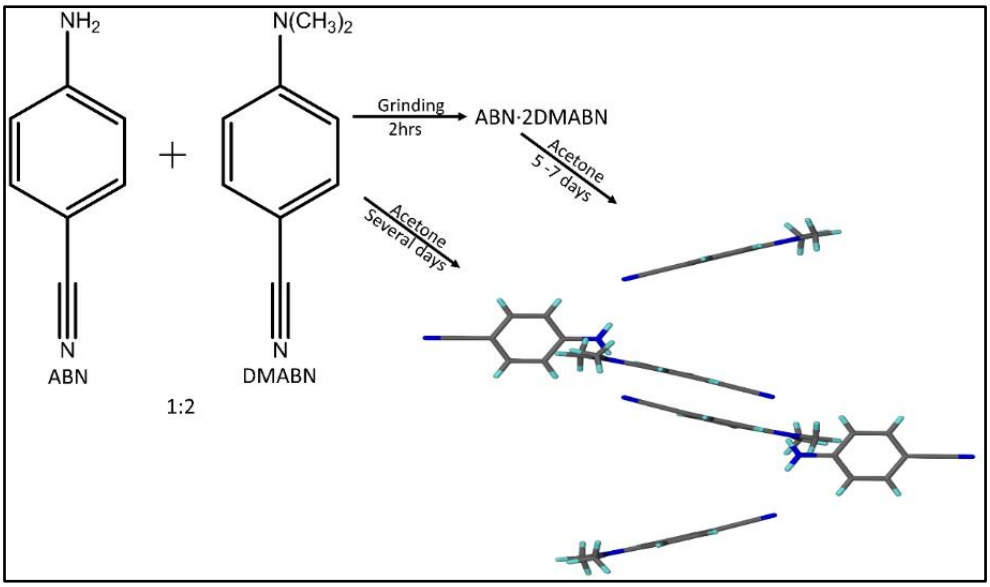

Scheme S1: Formation of the **ABN·2DMABN** cocrystal.

Single crystal X-ray diffraction measurements

Single-crystal X-ray diffraction data were collected using a Bruker APEX-II DUO CCD area detector diffractometer equipped with an Oxford Cryosystems 700Plus cryostat. A multilayer monochromator with Mo Kα radiation (λ = 0.71073 Å) from an Incoatec IμS micro source was

used. Data reduction was carried out by means of a standard procedure using the Bruker software package SAINT.[1] Absorption corrections and correction of other systematic errors were performed using SADABS.[2,3] The structures were solved by direct methods using SHELXS-2016 and refined using SHELXL-2016.[4] X-Seed was used as the graphical interface for the SHELX program suite.[5] Hydrogen atoms were placed in calculated positions using riding models.

Table S1. Crystallographic details for **ABN·2DMABN** cocrystal

Identification code	**ABN·2DMABN_ 300 K**	**ABN·2DMABN_ 280 K**	**ABN·2DMABN_ 260 K**	**ABN·2DMABN_ 240 K**	**ABN·2DMABN_ 220 K**	**ABN·2DMABN_ 200 K**
Empirical formula	$C_{25}H_{26}N_6$	$C_{25}H_{26}N_6$	$C_{25}H_{26}N_6$	$C_{25}H_{26}N_6$	$C_{25}H_{26}N_6$	$C_{25}H_{26}N_6$
Formula weight/g/mol	410.52	410.52	410.52	410.52	410.52	410.52
Temperature/K	300(2)	280(2)	260(2)	240(2)	220(2)	200(2)
Crystal system	Monoclinic	Monoclinic	Monoclinic	Monoclinic	Monoclinic	Monoclinic
Space group	$P2_1/n$	$P2_1/n$	$P2_1/n$	$P2_1/n$	$P2_1/n$	$P2_1/n$
a/Å	9.8177(10)	9.8071(2)	9.7994(2)	9.7912(2)	9.7836(2)	9.7770(3)
b/Å	25.6597(31)	25.6011(7)	25.5488(7)	25.4967(8)	25.4438(8)	25.3964(10)
c/Å	19.3047(23)	19.2577(5)	19.2173(5)	19.1789(5)	19.1399(6)	19.1058(7)
α/°	90	90.00	90.00	90.00	90.00	90.00
β/°	104.384(4)	104.347(1)	104.313(1)	104.291(1)	104.278(1)	104.272(1)
γ/°	90	90.00	90.00	90.00	90.00	90.00
Volume/Å^3	4710.8(9)	4684.3(2)	4662.0(2)	4639.7(2)	4617.4(2)	4597.6(3)
Z	8	8	8	8	8	8
ρ_{calc}g/cm^3	1.158	1.164	1.170	1.175	1.181	1.186
μ/mm^{-1}	0.072	0.072	0.072	0.073	0.073	0.073
F(000)	1744	1744	1744	1744	1744	1744
Crystal size/mm^3	0.335 × 0.242 × 0.116	0.334 × 0.241 × 0.115	0.333 × 0.24 × 0.114	0.332 × 0.239 × 0.113	0.331 × 0.238 × 0.112	0.33 × 0.237 × 0.111
Radiation	MoKα (λ = 0.71073)	MoKα (λ = 0.71073)	MoKα (λ = 0.71073)	MoKα (λ = 0.71073)	MoKα (λ = 0.71073)	MoKα (λ = 0.71073)
θ range for data collection/°	1.35 to 28.44	1.35 to 28.34	1.35 to 28.51	1.36 to 28.39	1.36 to 28.29	1.36 to 28.32
Index ranges	-13 ≤ h ≤ 11, -34≤ k ≤ 34, -25 ≤ l ≤ 25	-11 ≤ h ≤ 13, -34≤ k ≤ 34, -25 ≤ l ≤ 25	-11 ≤ h ≤ 13, -34≤ k ≤ 34, -25 ≤ l ≤ 25	-11 ≤ h ≤ 13, -34≤ k ≤ 34, -25 ≤ l ≤ 25	-11 ≤ h ≤ 13, -33≤ k ≤ 33, -25 ≤ l ≤ 25	-11 ≤ h ≤ 13, -33≤ k ≤ 33, -25 ≤ l ≤ 25
Reflections collected	166146	165295	163100	163738	162781	147347
Independent reflections	11782 [R_{int} = 0.0759, R_{sigma} = 0.0349]	11659 [R_{int} = 0.0854, R_{sigma} = 0.0394]	11736 [R_{int} = 0.0836, R_{sigma} = 0.0396]	11588 [R_{int} = 0.0808, R_{sigma} = 0.0384]	11444 [R_{int} = 0.0788, R_{sigma} = 0.0361]	11422 [R_{int} = 0.0768, R_{sigma} = 0.0374]
Data/restraints/parameters	11782/0/567	11659/0/567	11736/0/567	11588/0/567	11444/0/567	11422/0/567
Goodness-of-fit on F^2	1.035	1.061	1.066	1.046	1.046	1.051
Final R indexes [I>=2σ (I)]	R_1 = 0.0727, wR_2 = 0.2049	R_1 = 0.0703, wR_2 = 0.1864	R_1 = 0.0683, wR_2 = 0.1839	R_1 = 0.0647, wR_2 = 0.1615	R_1 = 0.0639, wR_2 = 0.1606	R_1 = 0.0613, wR_2 = 0.1490
Final R indexes [all data]	R_1 = 0.1592, wR_2 = 0.2735	R_1 = 0.1653, wR_2 = 0.2595	R_1 = 0.1578, wR_2 = 0.2543	R_1 = 0.1472, wR_2 = 0.2279	R_1 = 0.1359, wR_2 = 0.2171	R_1 = 0.1337, wR_2 = 0.2041
Largest diff. peak/hole / e Å^{-3}	0.14/-0.16	0.188/-0.191	0.17/-0.19	0.18/-0.22	0.18/-0.21	0.21/-0.21
Mosaicity	0.39	0.38	0.38	0.38	0.38	0.38

Table S1. Crystallographic details for **ABN·2DMABN** cocrystal continued.

Identification code	**ABN·2DMABN_ 180 K**	**ABN·2DMABN_ 160 K**	**ABN·2DMABN_ 140 K**	**ABN·2DMABN_ 120 K**	**ABN·2DMABN_ 100 K**
Empirical formula	$C_{25}H_{26}N_6$	$C_{25}H_{26}N_6$	$C_{25}H_{26}N_6$	$C_{25}H_{26}N_6$	$C_{25}H_{26}N_6$
Formula weight	410.52	410.52	410.52	410.52	410.52
Temperature/K	180(2)	160(2)	140(2)	120(2)	100(2)
Crystal system	Monoclinic	Monoclinic	Monoclinic	Monoclinic	Monoclinic
Space group	$P2_1/n$	$P2_1/n$	$P2_1/n$	$P2_1/n$	$P2_1/n$
a/Å	9.7754(3)	9.7730(3)	9.7661(3)	9.7650(3)	9.7654(4)
b/Å	25.3489(8)	25.2982(8)	25.2392(8)	25.1863(9)	25.1269(11)

c/Å	19.0721(6)	19.0409(6)	19.0103(6)	18.9850(7)	18.9626(8)
α/°	90.00	90.00	90.00	90.00	90.00
β/°	104.284(10)	104.279(1)	104.274(1)	104.254(1)	104.199 (1)
γ/°	90.00	90.00	90.00	90.00	90.00
Volume/Å^3	4579.9(2)	4561.0(2)	4541.2(2)	4525.5(3)	4510.8(3)
Z	8	8	8	8	8
ρ_{calc}g/cm^3	1.191	1.196	1.201	1.205	1.209
μ/mm^{-1}	0.074	0.074	0.074	0.074	0.075
F(000)	1744.0	1744.0	1744.0	1744.0	1744.0
Crystal size/mm^3	0.329 × 0.236 × 0.11	0.328× 0.235 × 0.109	0.327 × 0.234 × 0.108	0.326 × 0.233 × 0.107	0.325 × 0.232 × 0.106
Radiation	MoKα (λ = 0.71073)	MoKα (λ = 0.71073)	MoKα (λ = 0.71073)	MoKα (λ = 0.71073)	MoKα (λ = 0.71073)
θ range for data collection/°	1.61 to 28.37	2.66 to 28.35	138 to 28.36	1.37 to 28.38	1.37 to 28.34
Index ranges	-11 ≤ h ≤ 13, -33 ≤ k ≤ 33, -25 ≤ l ≤ 25	-11 ≤ h ≤ 13, -33 ≤ k ≤ 33, -25 ≤ l ≤ 25	-11 ≤ h ≤ 13, -33 ≤ k ≤ 33, -25 ≤ l ≤ 25	-11 ≤ h ≤ 13, -33 ≤ k ≤ 33, -25 ≤ l ≤ 25	-11 ≤ h ≤ 13, -33 ≤ k ≤ 33, -25 ≤ l ≤ 25
Reflections collected	211399	210216	209426	154099	178039
Independent reflections	11269 [R_{int} = 0.0948, R_{sigma} = 0.0359]	11218 [R_{int} = 0.0952, R_{sigma} = 0.0354]	11237 [R_{int} = 0.0954, R_{sigma} = 0.0352]	11236[R_{int} = 0.0909, R_{sigma} = 0.0389]	11176 [R_{int} = 0.0952, R_{sigma} = 0.0379]
Data/restraints/parameters	11269/0/567	11218/0/567	11237/0/567	11236/0/567	11176/0/567
Goodness-of-fit on F^2	1.026	1.020	1.037	1.026	1.033
Final R indexes [I>=2σ (I)]	R_1 = 0.0898, wR_2 = 0,2265	R_1 = 0.0953, wR_2 = 0.2229	R_1 = 0.0888, wR_2 = 0.2262	R_1 = 0.0876, wR_2 = 0.2192	R_1 = 0.0886, wR_2 = 0.2249
Final R indexes [all data]	R_1 = 0.1472, wR_2 = 0.3061	R_1 = 0.1425, wR_2 = 0.2958	R_1 = 0.1366, wR_2 = 0.2896	R_1 = 0.1383, wR_2 = 0.2858	R_1 = 0.1321, wR_2 = 0.2833
Largest diff. peak/hole / e Å^{-3}	0.29/-0.36	0.29/-0.40	0.39/-0.42	0.34/-0.45	0.49/-0.48
Mosaicity	0.38	0.38	0.38	0.38	0.38

Unit cell parameters for ABN·2DMABN cocrystal from 300 to 100 K at 20 K intervals

Table S2. Unit cell axes and cell volume at variable temperatures for **ABN·2DMABN** Cocrystal

T (K)	*a* (Å)	St. dev.*	*b* (Å)	St. dev.*	*c* (Å)	St. dev.*	β(°)	St. dev.*	V(Å^3)	St. dev.*	Crystal mosaicity
300	9.8177	0.001	25.6597	0.0031	19.3047	0.0023	104.384	0.004	4710.78	0.09	0.39
280	9.8071	0.0002	25.6011	0.0007	19.2577	0.0005	104.347	0.001	4684.29	0.02	0.38
260	9.7994	0.0002	25.5488	0.0007	19.2173	0.0005	104.313	0.001	4661.95	0.02	0.38
240	9.7912	0.0002	25.4967	0.0008	19.1789	0.0005	104.291	0.001	4639.72	0.02	0.38
220	9.7836	0.0002	25.4438	0.0008	19.1399	0.0006	104.278	0.001	4617.36	0.02	0.38
200	9.7770	0.0003	25.3964	0.001	19.1058	0.0007	104.272	0.001	4597.56	0.03	0.38
180	9.7754	0.0003	25.3489	0.0008	19.0721	0.0006	104.284	0.001	4579.88	0.02	0.38
160	9.7703	0.0003	25.2982	0.0008	19.0409	0.0006	104.279	0.001	4560.96	0.02	0.38
140	9.7661	0.0003	25.2392	0.0008	19.0103	0.0006	104.270	0.001	4541.16	0.02	0.38
120	9.7650	0.0003	25.1863	0.0009	18.9850	0.0007	104.254	0.001	4525.50	0.03	0.38
100	9.7654	0.0004	25.1269	0.0011	18.9626	0.0008	104.199	0.001	4510.75	0.03	0.38

*Standard deviation calculated from unit cell refinement using the Apex III software suite.

Powder X-ray diffraction measurements

Powder X-ray diffraction data were collected using a Bruker D2 PHASER equipped with Lynxeye 1D detector and Ni-filtered Cu Kα radiation (λ = 1.5418 Å; 30 kV, 10 mA generator parameters; restricted by a 1.0 mm divergence slit and a 2.5 Soller collimator). The high resolution PXRD pattern was recorded using Cu Kα radiation (λ = 1.5418 Å, 40 kV and 30 mA) on a PANalytical X'pert PRO instrument operating in Bragg-Brentano geometry. Samples were placed in sealed glass capillaries and analysed at room temperature.

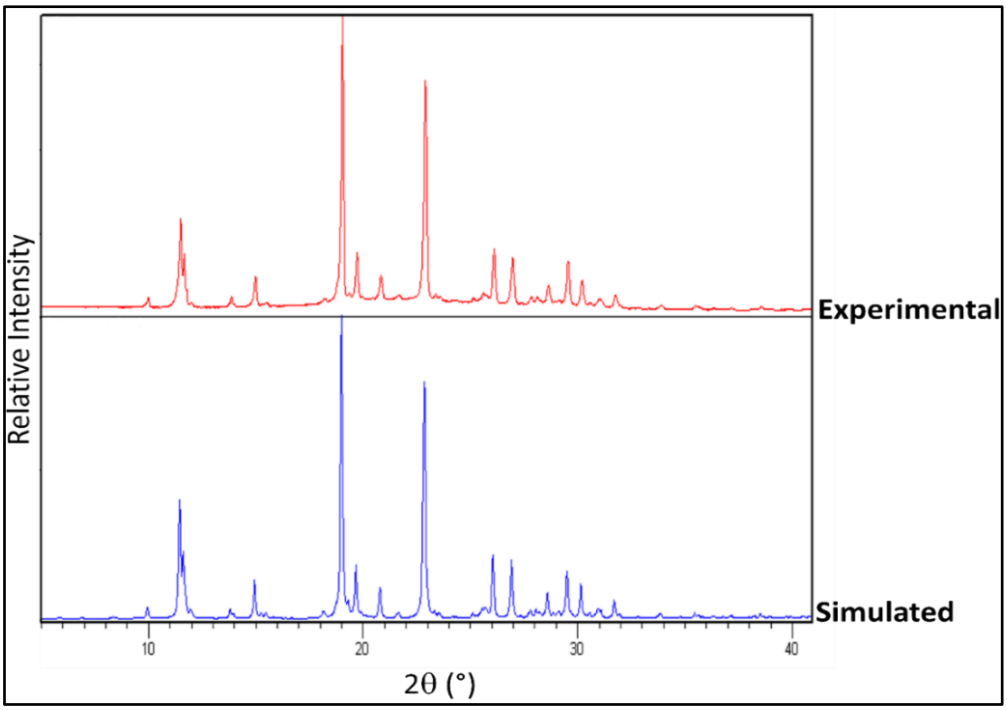

Figure S1: PXRD patterns of the experimental and simulated **ABN·2DMABN** cocrystal.

Hot stage microscopy

A Linkam DSC600 temperature-controlled hot stage equipped with a digital video camera and LNP95 liquid nitrogen cooling pump was used to record temperature-dependent changes in the appearance of cocrystal **ABN·2DMABN**. The stage was operated via a T95-System Controller. The temperature was ramped from 300 to 100 K and back to 300 K at a ramp rate of 5 K min^{-1}.

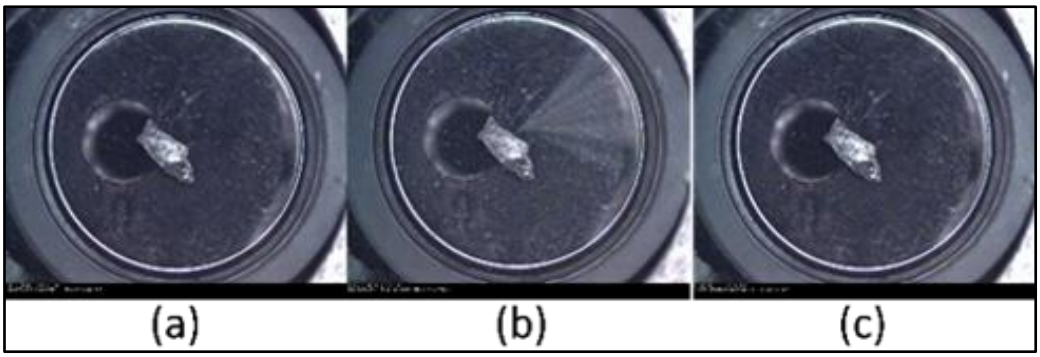

Figure S2: The micrographs of **ABN·2DMABN** at a) 300 K cooled to b) 100 K and reheated to c) 300 K.

Differential Scanning Calorimetry

Differential scanning calorimetry of **ABN·2DMABN** was carried out on TA DSC-Q100 instrument. Crystals were taken on a Tzero aluminium pan and connected to LNG cryostat for low temperature analysis. The low temperature DSC analysis was carried out by cooling from

300 to 100 K and heated back to 300 K at the heating rate of 5 K min^{-1}. Also, the crystal was analysed by heating from room temperature (300 K) to the selected temperature at rate of 5 K min^{-1}.

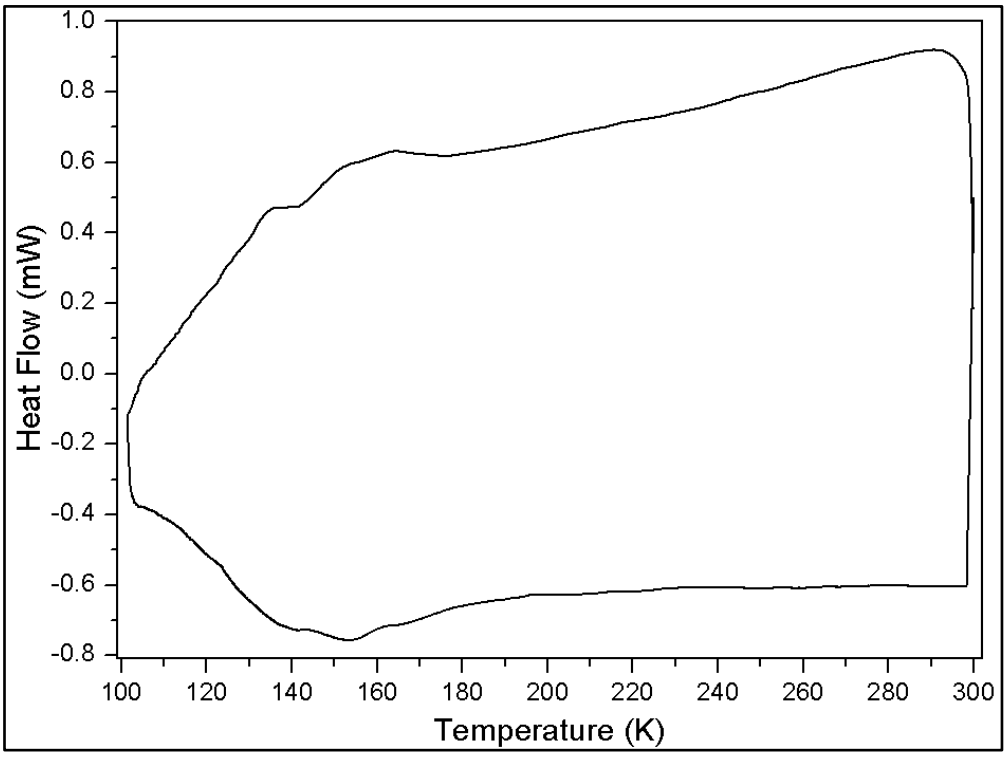

Figure S3: The DSC thermogram of the cocrystal **ABN·2DMABN** for the range 100 to 300 K showing no thermal events (no phase change).

Thermal expansion coefficients

Table S3. Linear and volumetric thermal expansion coefficients for **ABN·2DMABN** over different temperature ranges.

Temperature Range (K)	α_{X1} (MK^{-1})	α_{X2} (MK^{-1})	α_{X3} (MK^{-1})	α_v (MK^{-1})
100 – 120	-17.66	62.55	118.34	163.14
120 – 140	2.07	66.69	105.13	173.88
140 – 160	19.30	80.76	117.02	217.13
160 – 180	24.57	82.42	100.31	207.38
180 – 200	7.89	91.40	93.78	193.10
200 – 220	32.09	89.66	93.41	215.27
220 – 240	35.88	102.07	104.06	242.15
240 – 260	36.91	100.29	102.27	239.61
260 – 280	31.15	102.46	105.79	239.52
280 – 300	45.06	114.58	122.90	282.74

Table S4. Linear and volumetric thermal expansion coefficients for **ABN·2DMABN** over different temperature ranges that include 300 K.

Temperature Range (K)	α_{X1}(MK^{-1})	α_{X2} (MK^{-1})	α_{X3} (MK^{-1})	α_{v} (MK^{-1})
100 – 300	24.26	90.88	105.01	222.01
120 – 300	27.13	94.22	103.68	226.72
140 – 300	29.53	96.91	102.90	230.93
160 – 300	31.33	99.08	101.93	233.93
180 – 300	33.46	101.42	102.54	238.85
200 – 300	36.26	103.84	104.41	245.61
220 – 300	36.90	105.89	107.21	250.91
240 – 300	37.16	106.69	109.49	254.28
260 – 300	38.14	108.75	114.60	262.44
280 – 300	45.06	114.58	122.90	282.74

Intermolecular interactions in the structure

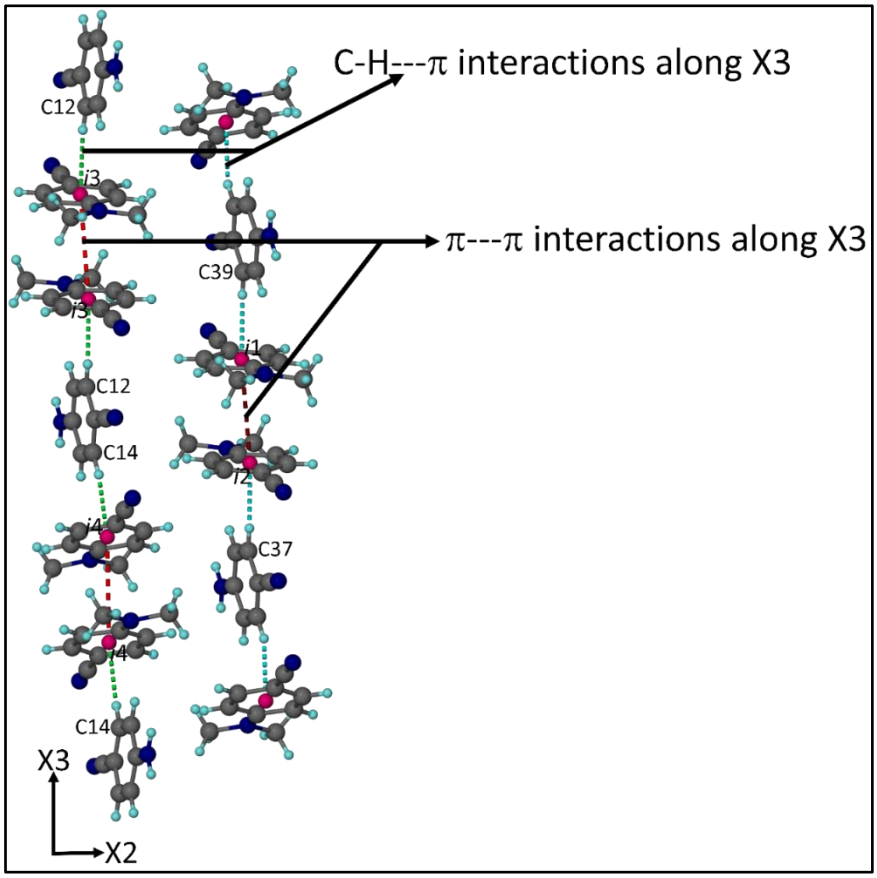

Figure S4: Perspective view showing C-H···π and π···π interactions along the principal axis X3.

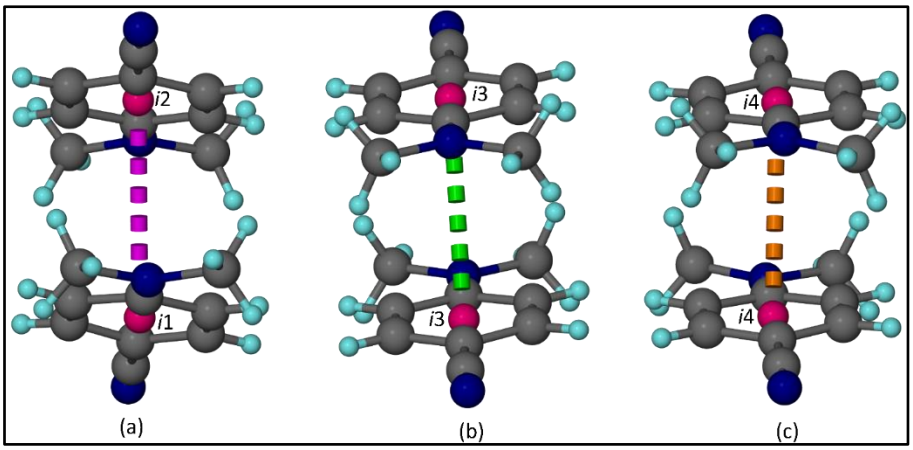

Figure S5: Views showing all the centroid-to-centroid distances (Å) along the principal axis X3 with (a) ***i*1---*i*2** (b) ***i*3---*i*3** and (c) ***i*4---*i*4**. ***i*1** is the centroid of C26-C31, ***i*2** is the centroid of C42-C47, ***i*3** is the centroid of C1-C6 and ***i*4** is the centroid of C17-C22.

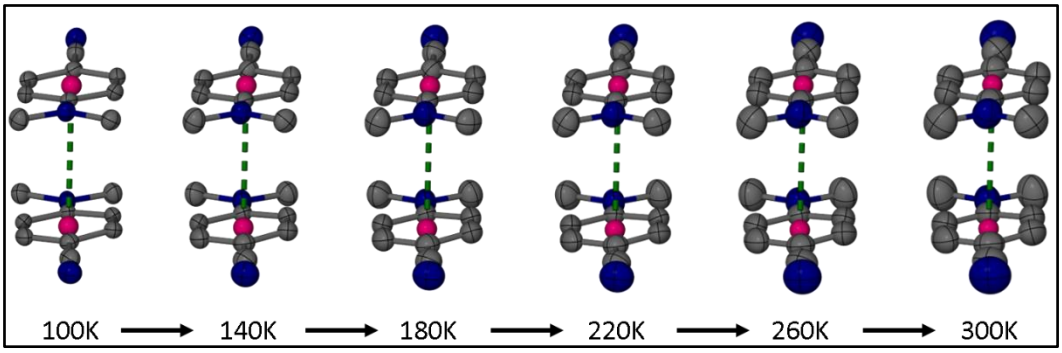

Figure S6: Views showing the increase in ellipsoids as the temperature increases along the principal axis X3 (30% probability).

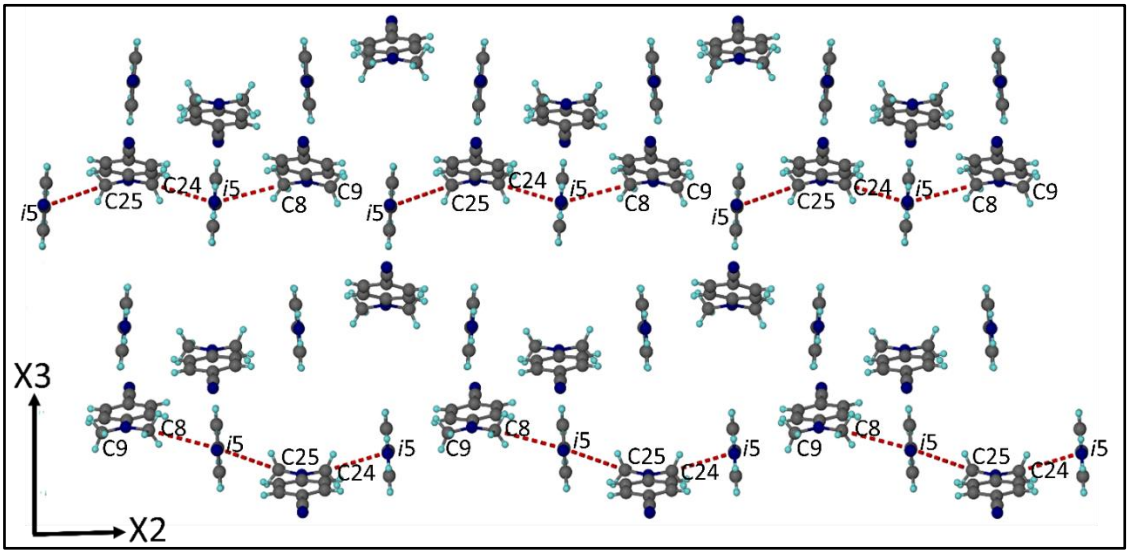

Figure S7: Perspective view showing C-H···π interactions along the principal axis X2.

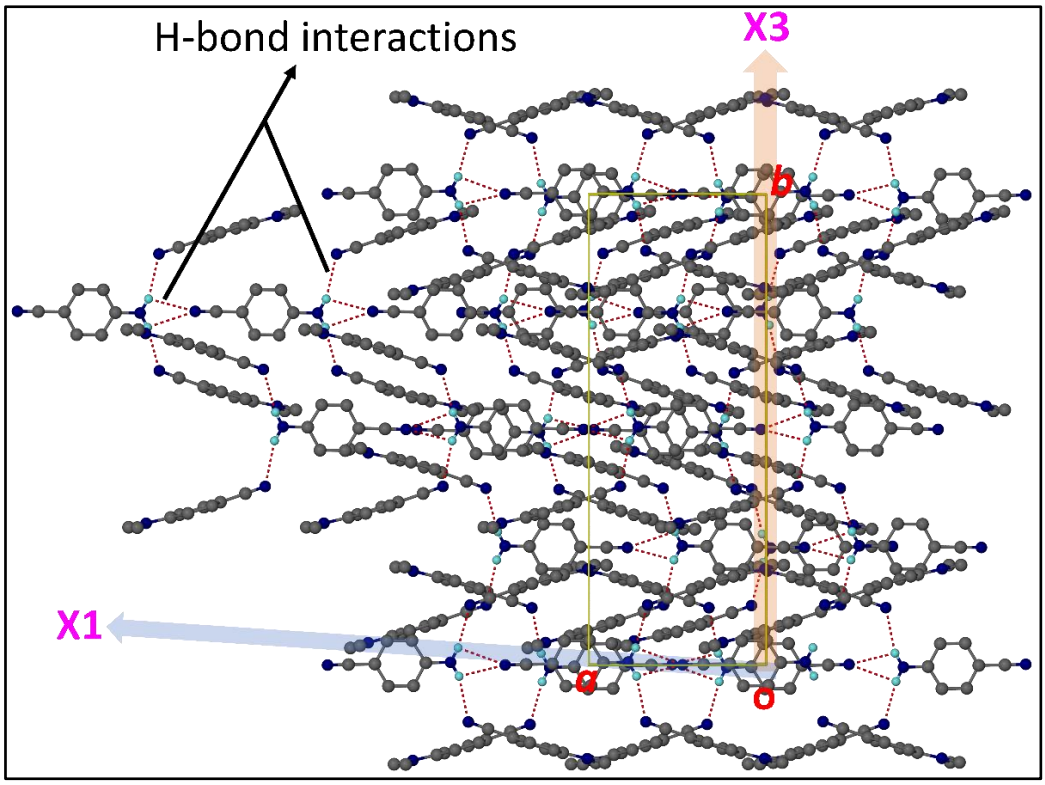

Figure S8: Perspective view of the **ABN·2DMABN** cocrystal showing N-H···N hydrogen bonding interactions along the principal axis X1.

The program PLATON was used to generate a list of hydrogen bond distances (D···A) (Å) in the **ABN·2DMABN** cocrystal from 100 to 300 K.

Table S5. Some intermolecular interaction distances (Å) within the molecules at different temperatures for **ABN·2DMABN** cocrystal along the principal axis X3.

Distance (Å)	T (K)											
	100	120	140	160	180	200	220	240	260	280	300	RC
π···π (*i*1---*i*2)	3.8843(2)	3.9064(1)	3.9241(1)	3.9293(1)	3.9536(1)	3.9615(2)	3.9704(1)	3.9819(1)	3.9910(1)	4.0021(1)	4.0134(5)	0.0332
π···π (*i*3---*i*3)	3.9594(2)	3.9801(1)	3.9960(1)	4.0109(1)	4.0209(1)	4.0286(2)	4.0384(1)	4.0472 (1)	4.0526(1)	4.0612(1)	4.0724(5)	0.0285
π···π (*i*4---*i*4)	3.8275(2)	3.8488(1)	3.8679(1)	3.8845(1)	3.8948(1)	3.9062(2)	3.9156(1)	3.9261(1)	3.9360(1)	3.9360(1)	3.9565(5)	0.0337
C12-H12···π (C12---*i*3)	3.4874(1)	3.4948(1)	3.5032(1)	3.5130(1)	3.5247(1)	3.5329(1)	3.5429(1)	3.5575(1)	3.5710(1)	3.5847(1)	3.5969(4)	0.0314
C14-H14···π (C14---*i*4)	3.4770(1)	3.4852(1)	3.4983(1)	3.5091(1)	3.5226(1)	3.5298(1)	3.5425(1)	3.5543(1)	3.5679(1)	3.5809(1)	3.5956(4)	0.0341
C37-H37···π (C37---*i*2)	3.5245(1)	3.5307(1)	3.5404(1)	3.5500(1)	3.5649(1)	3.5688(1)	3.5813(1)	3.5917(1)	3.6064(1)	3.6202(1)	3.6324(4)	0.0306
C39-H39···π (C39---*i*1)	3.4453(1)	3.4530(1)	3.4644 (1)	3.4760(1)	3.4870(1)	3.4989(1)	3.5097(1)	3.5228(1)	3.5351(1)	3.5463(1)	3.5619(4)	0.0338

*i*1= centroid of C26-C31, *i*2= centroid of C42-C47, *i*3= centroid of C1-C6 and *i*4= centroid of C17-C22.
RC= Relative change with respect to 100 K.

Table S6. Some important C-H···π interactions within the molecules at different temperatures for **ABN·2DMABN** cocrystal along X2.

Distance (Å)	T (K)											RC
	100	120	140	160	180	200	220	240	260	280	300	
C8-H8C···π (C8···*i*5)	4.0048(1)	3.9943(1)	3.9899(1)	3.9897(1)	3.9966(1)	4.0138(1)	4.0259(1)	4.0425(1)	4.0587(1)	4.0707(1)	4.0872(4)	0.0206
C24-H24C···π (C24···*i*5)	3.6578(1)	3.6650(1)	3.6738(1)	3.6845(1)	3.6908(1)	3.6948(1)	3.7015(1)	3.7064(1)	3.7111(1)	3.7171(1)	3.7243(4)	0.0182
C25-H25B···π (C25···*i*5)	4.1145(1)	4.1292(1)	4.1453(1)	4.1590(1)	4.1766(1)	4.1904(1)	4.2075(1)	4.2266(1)	4.2455(1)	4.2657(1)	4.2837(4)	0.0411

*i*5= centroid of C35-C40.
RC= Relative change with respect to 100 K.

Table S7. Hydrogen bond parameter, D (distance (Å) between H-bond donor and H-bond acceptor) at different temperatures for **ABN·2DMABN** cocrystal along X1.

D···A (Å)	T (K)										
	100	120	140	160	180	200	220	240	260	280	300
N3-H3D…N6	3.275(3)	3.274(4)	3.275(4)	3.278(4)	3.286(4)	3.288(4)	3.296(3)	3.301(4)	3.304(4)	3.316(4)	3.326(5)
N3-H3E…N2	3.334(3)	3.343(4)	3.341(4)	3.346(4)	3.350(4)	3.350(4)	3.352(3)	3.356(4)	3.359(4)	3.362(4)	3.358(5)
N9-H9E…N8	3.259(4)	3.264(4)	3.267(4)	3.268(4)	3.276(4)	3.284(4)	3.287(3)	3.297(4)	3.310(4)	3.309(4)	3.323(5)
N9-H9D…N12	3.344(4)	3.340(4)	3.345(4)	3.344(4)	3.346(4)	3.346(4)	3.350(3)	3.351(3)	3.360(4)	3.362(4)	3.370(5)

Table S8. Hydrogen bond parameter showing bond angle (°) between H-bond donor and H-bond acceptor at different temperatures for **ABN·2DMABN** cocrystal along X1.

>D-H···A (°)	T (K)										
	100	120	140	160	180	200	220	240	260	280	300
N3-H3D···N6	166.77(17)	167.16(18)	166.74(20)	166.71(21)	166.41(21)	166.30(17)	166.01(19)	166.15(19)	166.71(21)	165.87(23)	166.14(24)
N3-H3E···N4	161.65(17)	161.66(18)	161.75(19)	161.88(21)	161.93(21)	161.90(17)	162.09(19)	161.97(19)	161.56(20)	161.98(23)	161.91(24)
N9-H9E···N8	168.33(17)	168.09(18)	168.02(20)	167.68(21)	167.32(21)	167.45(17)	167.24(19)	166.96(19)	166.13(20)	166.67(22)	165.80(26)
N9-H9D··N12	160.22(17)	160.23(18)	160.70(19)	160.86(21)	161.15(21)	161.02(17)	161.27(19)	161.42(19)	162.00(20)	161.47(22)	161.74(26)

Table S9. Showing bond distance (Å) between H-donor Nitrogen and H-acceptor Nitrogen at different temperature for **ABN·2DMABN** cocrystal along the principal axis X1.

Distance (Å)	T (K)											
N···N(Å)	100	120	140	160	180	200	220	240	260	280	300	RC
N3···N4	3.0106(1)	3.0192(1)	3.0207(1)	3.0295(1)	3.0376(1)	3.0459(1)	3.0533(1)	3.0639(1)	3.0739(1)	3.0853(1)	3.0990 (3)	0.0296
N9···N10	3.0171(1)	3.0174(1)	3.0217(1)	3.0281(1)	3.0342(1)	3.0434(1)	3.0528(1)	3.0627(1)	3.0717(1)	3.0834(1)	3.0931 (3)	0.0252

RC= Relative change with respect to 100 K.

3.3. References

1. *SAINT Data Reduction Software*, Version 6.45; Bruker AXS Inc.: Madison, WI, 2003.

2. *SADABS*, Version 2.05; Bruker AXS Inc.: Madison, WI, 2002.

3. R. H. Blessing, An Empirical Correction for Absorption Anisotropy. *Acta Crystallogr., Sect. A: Found. Crystallogr*. 1995, **51**, 33.

4. G. M. Sheldrick, A Short History of SHELX. *Acta Crystallogr., Sect. A: Found. Crystallogr*. 2008, **64**, 112.

5. L. Barbour, X-Seed − A Software Tool for Supramolecular Crystallography. *J. Supramol. Chem*. 2001, **1**, 189.

Chapter 4: Hand-twistable plastically deformable crystals of a rigid small organic molecule

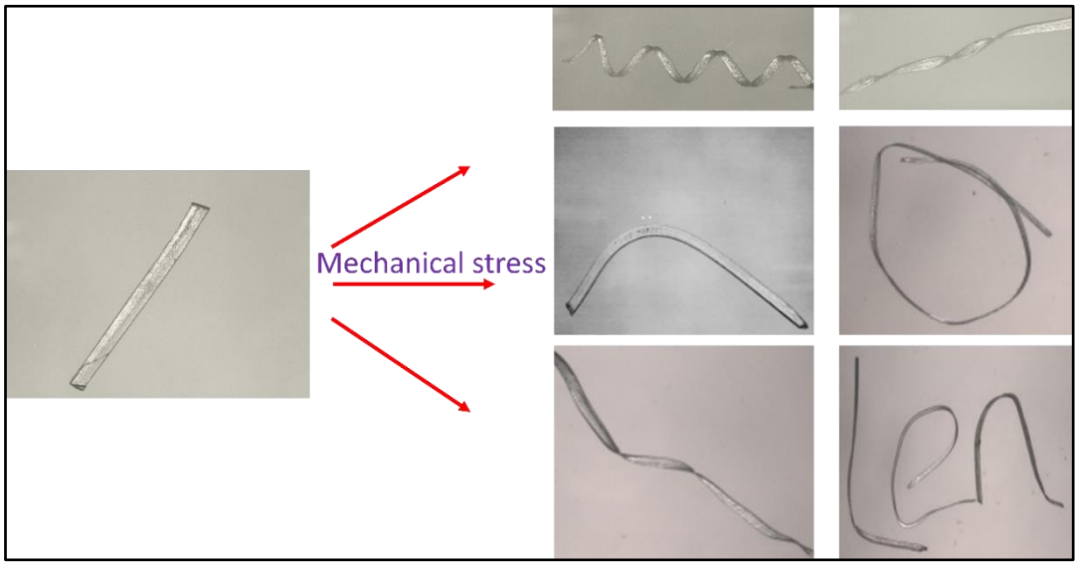

4.1. Communication in chemical communications (Published)

Contributions of the main author:

- Design of the project
- Crystallisation of the material
- Preparation of the crystals (straight and bent crystals)
- Collection of single-crystal X-ray data
- Solution and refinement of single-crystal X-ray structure
- Determination of face indices
- Generation of the crystal habit
- Recording of PXRD patterns
- Recording of IR spectra
- Recording of Hot stage micrographs
- Recording of DSC and TGA thermograms
- Interpretation of results with Dr Prem Lama and Dr Vincent J. Smith
- Writing the first draft of the article

ChemComm

COMMUNICATION

Cite this: *Chem. Commun.*, 2018, 54, 2994

Received 29th January 2018, Accepted 26th February 2018

DOI: 10.1039/c8cc00775f

rsc.li/chemcomm

Hand-twistable plastically deformable crystals of a rigid small organic molecule†

Lukman O. Alimi, Prem Lama, Vincent J. Smith ‡ and Leonard J. Barbour *

4-Bromobenzonitrile was crystallised by sublimation under vacuum. The crystals show highly flexible plastic bending along two perpendicular faces when a mechanical force is applied. The rare occurrence of bending along two perpendicular faces results in twisting or helix formation.

Ordered molecular crystals that bend, twist, or coil like soft materials such as polymers, elastomers and liquid crystals are unusual.[1] Much attention has recently been devoted to understanding the mechanical flexibility of molecular crystals because of possible applications in areas such as pharmaceuticals,[2] muscle mimetic biomaterials,[3] artificial mechanosensors,[4] molecular machinery,[5] optical devices,[6] organic electronics[7] and smart nanomaterials.[8] Desiraju and co-workers were the first to report on mechanical bending in molecular crystals of hexachlorobenzene, a phenomenon that has since become recognised as a relatively widespread phenomenon.[9]

Deformation of an organic crystal can be either elastic or plastic.[10] Elastic materials undergo reversible distortion while plastic deformation occurs when a material undergoes permanent, irreversible distortion upon the application of mechanical stress. Generally, plastic behaviour is affected by several features of crystal packing, such as slip-planes,[11,12] dislocation motion,[13,14] twinning,[14,15] kinking,[16] and perturbation of the lattice stability.[14] Indeed, it has been postulated that the plasticity of crystal deformation depends on the mobility of dislocations, which are governed by slip-planes and the strengths of intermolecular interactions.[9a,b]

Plasticity can offer some distinctive and varied advantages in functional molecular crystals. These include excellent mechanochromic luminescence[2a,17–19] in solid-state fluorophores,[17–19] good tabletability in API solid forms[19,20] and lower detonation sensitivity in explosives.[19] Recent studies of the mechanisms[18a,20] of plastic deformation have suggested that bending progresses by separation of the bent region into flexible layers that move smoothly over one another through the rearrangement of weak intermolecular interactions, thus producing areas with slightly different lattice orientations.[18a,20]

Desiraju and co-workers have reported[9] plastic bending of crystals composed of the 4-halobenzonitrile compounds 4-chlorobenzonitrile (4-CBN) and 4-flourobenzonitrile (4-FBN). However, to our knowledge there have been no reports to date on the plasticity of 4-bromobenzonitrile (4-BBN), although its crystal structure has been published three times.[21] This prompted us to carry out a detailed investigation of the mechanical and physical properties of 4-bromobenzonitrile.

Elongated cuboid (orthogonal parallelepiped) crystals of 4-BBN were obtained by sublimation under dynamic vacuum (0.02 mbar) at 323 K for 3 hours. It is noteworthy that the formation of well-shaped crystals suitable for single-crystal X-ray diffraction (SCXRD) could only be obtained under the above-mentioned conditions of temperature, pressure and duration of sublimation (Scheme S1, ESI†). Some of the as-grown crystals were curved along their long axes, implying that the crystals might exhibit plastic deformation. This was confirmed by selecting several straight crystals and then testing for plasticity. We noted that the crystals can be bent on two different long faces, and that they could also be twisted to form helices.

SCXRD analysis was carried out on 4-BBN at 273 K. 4-BBN crystallises in the polar monoclinic space group *Cm*, with half a molecule in the asymmetric unit ($Z' = 0.5$) (Table S1, ESI†). The benzene moieties of 4-BBN are arranged in offset π-stacks, forming columns parallel to [001] (Fig. 1a and b). Consecutive columns are linked by catemeric (C)N···Br(C) halogen bonds[22] ($d_{N\cdots X}$ = 3.25 Å, θ_1 = 166.5°) to yield layers parallel to [100] (Fig. 1b). These layers propagate in an ···ABAB··· manner along [010]. The stacks are also held together by halogen···π ($d_{X\cdots\pi}$) stacking interactions, and other weak electrostatic ($d_{C\cdots\pi}$)

Department of Chemistry and Polymer Science, University of Stellenbosch, Matieland, 7602, Stellenbosch, South Africa. E-mail: ljb@sun.ac.za

† Electronic supplementary information (ESI) available: Experimental methods, PXRD, Hot stage microscopy images, DSC, and intermolecular interactions details. CCDC 1587640 and 1587641. For ESI and crystallographic data in CIF or other electronic format see DOI: 10.1039/c8cc00775f

‡ Current address: Department of Chemistry, Rhodes University, Grahamstown, 6140, South Africa.

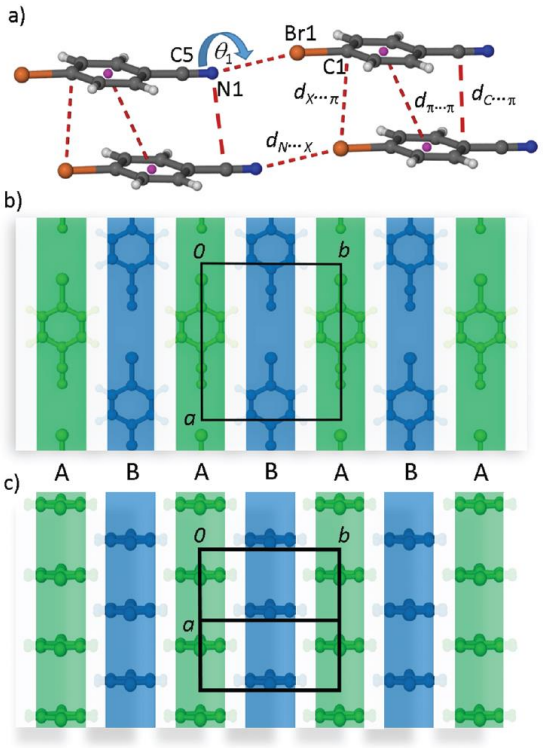

Fig. 1 (a) Perspective view showing C–N···Br halogen bonding, halogen···π, π···π and nitrile···π interactions. (b) The white inserts represent weak van der Waals close contacts (C)H···Br(C) and (C)H···C(N) between columns parallel to [100]. (c) Columnar molecular arrays of 4-BBN viewed along the diagonal [10−1], which also coincides with the direction of the ((C)Br···N(C)) halogen bonds. The white inserts represent the weak van der Waals close contacts between columns. Hydrogen (white), bromine (brown), carbon (grey), nitrogen (blue) and centroids (pink).

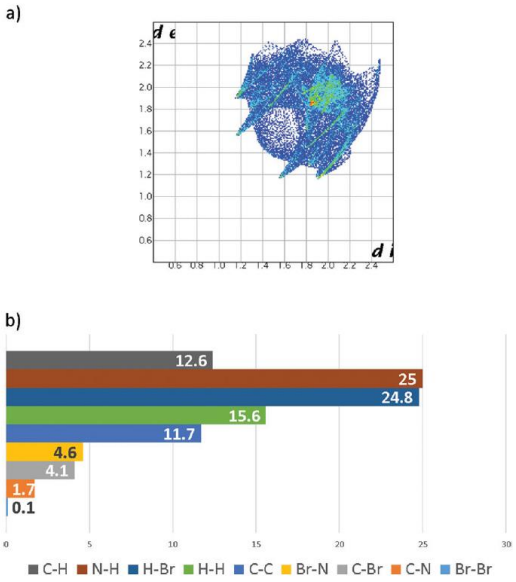

Fig. 2 (a) Fingerprint plot of all the intermolecular interactions in 4-BBN. (b) Histogram showing a breakdown of the interatomic contacts by percentage.

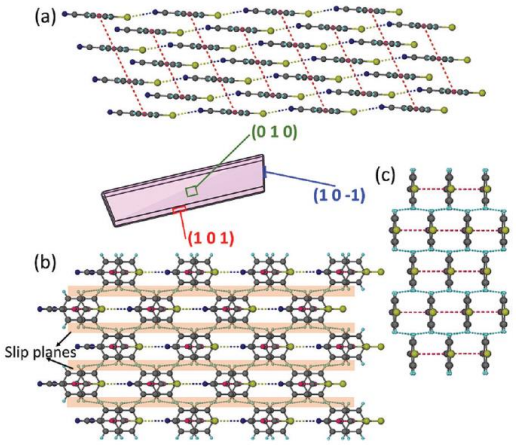

Fig. 3 Face indices of the crystal with the crystal habit showing the packing in (a) and (b) bendable facets and unbendable facet (c). Some of the Br atoms and C≡N group have been omitted for clarity.

interactions parallel to [001] (see Fig. 1(a), Fig. S2 and Tables S2, S3, ESI†).[23] Additionally, several van der Waals interactions (C–H···Br and C–H···C(N)) propagate parallel to [010] Fig. 1(c) (Table S3, ESI†). Fig. 2 shows the fingerprint plot as well as a quantitative summary of the interatomic contacts in the system. We note that Desiraju *et al.*[21a,24] obtained very similar data for 4-CBN in which only weak halogen bonding (C)N···Cl(C) and van der Waals close contacts were observed.[9c,18a,22]

According to Reddy *et al.*,[9c,18a,22] such interactions facilitate flexibility/bending. This was further supported by Krishna *et al.*,[18a] who found that the presence of halogen bonding, π···π interactions as well as van der Waals close contacts in the absence of an extended rigid hydrogen bonding network may facilitate flexibility in crystals.

In order to correlate the packing arrangement and intermolecular interactions with the crystal faces, a single crystal of 4-BBN was face-indexed, as shown in Fig. 3 and 4. The Miller indices and the associated crystal face distances obtained from the APEX III software[25] were used to simulate the crystal habit using the morphology module within the Biovia Materials Studio 7.0 software suite.[26] The single-crystal structure was then superimposed on the crystal habit.

The molecules are oriented edge-on relative to the (010) plane, which also coincides with one of the external faces of the crystal; the halogen bonds and π···π stacking interactions propagate parallel to this face (Fig. 3 and Fig. S3, ESI†). It is also relevant to consider the packing with respect to the (101) plane, which corresponds to another crystal face. The molecules are arranged in 1D halogen bonded (C)N···Br(C) chains along [10−1]. If we then consider weak van der Waals interactions between these chains along [010], the molecules form

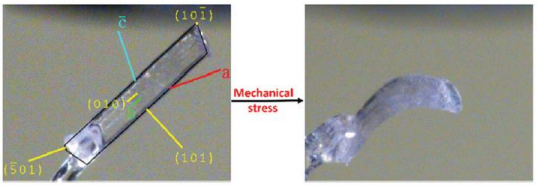

Fig. 4 Face indexing of a crystal of 4-BBN (left) and bending on the (010) face.

2D sheets parallel to the (101) face. The aromatic rings of the 4-BBN molecules are aligned almost parallel to these 2D sheets (Fig. S4, ESI†). When viewed along [10−1] the molecules are arranged in columnar molecular arrays that are interleaved by van der Waals contacts, see Fig. 1c (Fig. S5, ESI†).

The relationship between the intermolecular interactions and the faces along which the crystals bend was determined by applying mechanical force perpendicular to each face of a cuboid single crystal – *i.e.* the same crystal as that indexed and shown in Fig. 4 (Fig. S6 and Movie S1, ESI†). When describing how a macroscopic crystal bends relative to its assigned unit cell, it is necessary to provide the Miller indices both of the face that bends, as well as the axis around which bending occurs.

The crystal bends on two faces: (010) around [001] and (101) around [010]. However, it tears when force is applied perpendicular to (10−1) (Fig. S7, ESI†). Bending of the (010) face occurs perpendicular to the columnar molecular arrays. This is unsurprising as the arrays are usually implicated in 1D plastic bending, as shown by Desiraju *et al.*[9] Similar to those examples, the stacking interactions ($d_{X\cdots\pi}$, $d_{\pi\cdots\pi}$ and $d_{C\cdots\pi}$) are relatively strong compared to the orthogonal van der Waals contacts (Fig. 1c). Bending of (101) is also unsurprising as the soft halogen bond interactions (C)N···Br(C) propagate parallel to this plane. These interactions are akin the X···X (X = Br, Cl) halogen bonds reported in other structures[22a] in which slip-planes occur parallel to the X···X interactions. The (C)N···Br(C) slip-planes thus result in 1D plastic bending of (101). 2D plastic deformation is rare and there are only two examples in the literature, both reported by Saha *et al.*[22] The significance of the two orthogonal 1D plastic deformations (2D) is that it allows for twisting or helical deformation, as shown in Fig. 5.

The mechanism for the 2D deformation appears to be similar to those described by Saha *et al.* – *i.e.* the packing and intermolecular interactions are anisotropic in nature. The columnar molecular stacks are separated from each other by 2D sheets of van der Waals interactions which, according to Krishna *et al.*, facilitates sliding of molecules when mechanical force is applied. The difference between 4-BBN and the examples reported by Saha *et al.* is that 4-BBN is a rigid small molecule with a single phenyl ring, whereas the molecules reported by Saha consist of two non-planar phenyl rings that are covalently linked along the molecular axis by a flexible moiety such as amides or esters.[22]

Three different crystals of 4-BBN were subjected to differential scanning calorimetric analysis in the range −173 to 117 °C (Fig. S8 and S9, ESI†). An unbent crystal of 4-BBN produces a single melt endotherm with a peak maximum at 114 °C.§ A second crystal of 4-BBN with a single bend on (010) was also subjected to the same temperature program. The thermogram (Fig. S9, ESI†) shows two peaks with maxima at 111 °C (small) and 112 °C (larger). A third crystal with multiple bends on (010) shows two peaks that are approximately equal in size at 113 and 115 °C. Similar changes in melting behaviour due to bending have been observed before.[20]

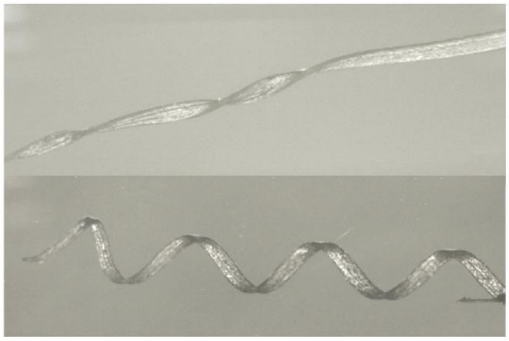

Fig. 5 Photomicrographs of hand-twisted/helical crystals of 4-BBN.

Hot stage microscopy was carried out to visualise the two separate thermal events. Unbent 4-BBN melts uniformly (Movie S2, ESI†) while the bent crystals start to melt at the bend, followed by progression of melting to the rest of the crystal (Fig. S10 and Movie S3, ESI†). We attribute the slight differences in melting points to possible reduction of structural order in the bent regions. This was partially confirmed by our attempt to record single-crystal X-ray diffraction data at the location of the bend in the crystal (Fig. 6, right); it was not possible to obtain data of sufficient quality for structure solution. However, in a second attempt X-ray diffraction data were recorded some distance (Fig. 6, centre) away from the bend and the associated structural data for (4-BBN-B) are provided in the ESI† (Tables S1–S3 and Fig. S11). The unit cell parameters of the straight and bent crystals are not very different. However, the amount of distortion in the discrete diffraction images

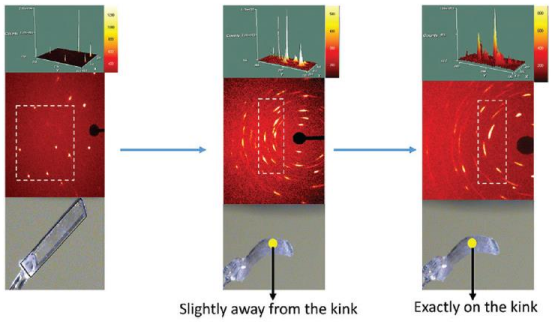

Fig. 6 Representative X-ray diffraction frames (Mo Kα) for an unbent crystal (left) and a bent crystal (centre and right); the yellow circles indicate the region of the crystal exposed to the X-ray beam.

increases substantially as one approaches the centre of the bend in the crystal.

Crystals were also analysed using Fourier transform infrared (FTIR) spectroscopy. The IR spectrum of 4-BBN shows a nitrile stretching band around 2223 cm^{-1} and an aromatic C–H stretch in the range 2780–3086 cm^{-1}. After bending the crystals, additional C–N and aromatic C–H stretches are observed, as well as a new broad peak around 3294 cm^{-1} (Fig. S12, ESI†). The latter is associated with the formation of weak intermolecular hydrogen bonding interactions resulting from the change in the non-bonding distances and angles within the crystal upon bending.[27]

In summary, we have successfully obtained single crystals of 4-BBN suitable for single-crystal X-ray diffraction using specific conditions of sublimation. These crystals display plastic deformation along two orthogonal directions, which is unique for crystals composed of small rigid organic molecules. This phenomenon appears to be driven by the weak anisotropic interactions and anisotropic packing arrangement of the molecules. Movements of the columnar molecular arrays is facilitated by 2D sheets of van der Waals contacts located between the arrays. Moreover, bending on the two orthogonal faces (010) and (101) allows the crystals to be hand-twisted. As a result, some of the physical properties (*e.g.* melting point of the crystal) are affected.

Finally, we note that Desiraju *et al.* have asserted that anisotropy, both of interactions and of the packing arrangement, are essential for plastic bending.[9c] However, more recently Spackman *et al.* have shown that crystals can still bend when only weak isotropic interactions are present.[28] These arguments may have little bearing on 4-BBN since it is rigid and still able to undergo helical bending, whereas the systems previously considered are comprised of conformationally flexible molecules. Therefore it appears that there are still too many variables and too few examples to allow us to formulate a set of rules for these phenomena. In the case of 4-BBN, the orientation of the rigid molecule appears to correlate with the axis that bends, and the two fold axes.

LJB and VJS thank the National Research Foundation and Stellenbosch University for financial support. LOA and PL also acknowledge UMYU (TETFund) and the Claude Leon Foundation, respectively, for financial support.

Conflicts of interest

There are no conflicts to declare.

Notes and references

§ We note that onset temperatures rather than maxima are generally reported for DSC peaks since the latter depend on factors such as sample size, particle size distribution and heating rates. However, in cases where onset temperatures are difficult to determine (*e.g.* overlapping peaks, sloping baseline), it is useful to compare peak maxima for multiple isotherms provided that the abovementioned experimental factors are kept consistent.

1 (*a*) Y. Yu, M. Nakano and T. Ikeda, *Nature*, 2003, **425**, 145; (*b*) L. Zhang, H. Liang, J. Jacob and P. Naumov, *Nat. Commun.*, 2015, **6**, 7429; (*c*) H. Zeng, P. Wasylczyk, C. Parmeggiani, D. Martella, M. Burresi and D. S. Wiersma, *Adv. Mater.*, 2015, **27**, 3883.
2 (*a*) P. P. Bag, M. Chen, C. C. Sun and C. M. Reddy, *CrystEngComm*, 2012, **14**, 3865; (*b*) S. Karki, T. Friščić, L. Fábián, P. R. Laity, G. M. Day and W. Jones, *Adv. Mater.*, 2009, **21**, 3905; (*c*) F. P. A. Fabbiani, D. R. Allan, W. I. F. David, A. J. Davidson, A. R. Lennie, S. Parsons, C. R. Pulham and J. E. Warren, *Cryst. Growth Des.*, 2007, **7**, 1115.
3 S. Lv, D. M. Dudek, Y. Cao, M. M. Balamurali, J. Gosline and H. Li, *Nature*, 2010, **465**, 69.
4 P. Fratzl and F. G. Barth, *Nature*, 2009, **462**, 442.
5 M. A. Garcia-Garibay, *Angew. Chem., Int. Ed.*, 2007, **46**, 8945.
6 (*a*) G. John, S. R. Jadhav, V. M. Menon and V. T. John, *Angew. Chem., Int. Ed.*, 2012, **51**, 1760; (*b*) Q. H. Cui, Y. S. Zhao and J. J. Yao, *Mater. Chem.*, 2012, **22**, 4136.
7 J. A. Rogers, T. Someya and Y. Huang, *Science*, 2010, **327**, 1603.
8 Y. Cao and H. Li, *Nat. Nanotechnol.*, 2008, **3**, 512.
9 (*a*) C. M. Reddy, R. C. Gundakaram, S. Basavoju, M. T. Kirchner, K. A. Padmanabhan and G. R. Desiraju, *Chem. Commun.*, 2005, 3945; (*b*) C. M. Reddy, M. T. Kirchner, R. C. Gundakaram and G. R. Desiraju, *Chem. – Eur. J.*, 2006, **12**, 2222; (*c*) C. M. Reddy, K. A. Padmanabhan and G. R. Desiraju, *Cryst. Growth Des.*, 2006, **6**, 2720.
10 S. Ghosh, M. K. Mishra, S. B. Kadambi, U. Ramamurty and G. R. Desiraju, *Angew. Chem., Int. Ed.*, 2015, **54**, 2674.
11 C. C. Sun and H. Hou, *Cryst. Growth Des.*, 2008, **8**, 1575.
12 G. I. Taylor, *Proc. R. Soc. London, Ser. A*, 1934, **145**, 362.
13 C. C. Sun, *Int. J. Pharm.*, 2008, **347**, 171.
14 J. Weertman and J. R. Weertman, *Elemental Dislocation Theory*, Oxford Uni. Press, Oxford, 1992.
15 R. Bandyopadhyay and D. J. W. Grant, *Pharmacol. Res.*, 2002, **19**, 491.
16 A. Argon and B. Quentin, *Strengthening Mechanisms in Crystal Plasticity*, Oxford Scholarship Online, 2007.
17 G. R. Krishna, M. S. R. N. Kiran, C. L. Fraser, U. Ramamurty and C. M. Reddy, *Adv. Funct. Mater.*, 2013, **23**, 1422.
18 (*a*) G. R. Krishna, R. Devarapalli, G. Lal and C. M. Reddy, *J. Am. Chem. Soc.*, 2016, **138**, 13561; (*b*) G. R. Krishna, R. Devarapalli, R. Prusty, T. Liu, C. L. Fraser, U. Ramamurty and C. M. Reddy, *IUCrJ*, 2015, **2**, 611; (*c*) G. R. Krishna, L. Shi, P. P. Bag, C. C. Sun and C. M. Reddy, *Cryst. Growth Des.*, 2015, **15**, 1827.
19 C. Zhang, X. Wang and X. Huang, *J. Am. Chem. Soc.*, 2008, **130**, 8359.
20 M. K. Panda, S. Ghosh, N. Yasuda, T. Moriwaki, G. D. Mukherjee, C. M. Reddy and P. Naumov, *Nat. Chem.*, 2015, **7**, 65.
21 (*a*) G. R. Desiraju and R. L. Harlow, *J. Am. Chem. Soc.*, 1989, **111**, 6757; (*b*) D. Britton, J. Konnert and S. Lam, *Cryst. Struct. Commun.*, 1977, **6**, 45.
22 (*a*) S. Saha and G. R. Desiraju, *J. Am. Chem. Soc.*, 2017, **139**, 1975; (*b*) S. Saha and G. R. Desiraju, *Chem. Commun.*, 2017, **53**, 6371.
23 (*a*) M. J. Rashkin and M. L. Waters, *J. Am. Chem. Soc.*, 2002, **124**, 1860; (*b*) C. A. Hunter, K. R. Lawson, J. Perkins and C. J. Urch, *J. Chem. Soc., Perkin Trans. 2*, 2001, 651; (*c*) J.-C. Dai, S.-M. Hu, X.-T. Wu, Z.-Y. Fu, W.-X. Du, H.-H. Zhang and R.-Q. Sun, *New J. Chem.*, 2003, **27**, 914; (*d*) C. Janiak, *J. Chem. Soc., Dalton Trans.*, 2000, 3885.
24 G. R. Desiraju, J. A. R. P. Sarma and T. S. R. Krishna, *Chem. Phys. Lett.*, 1986, **131**, 124.
25 SAINT Data Reduction Software, Version 2017.3-RC2; Bruker AXS 2005–2017.
26 Materials Studio Modelling Environment, Version 6.0.0; Accelrys Software Inc., San Diego, 2011.
27 L. Pejov, M. K. Panda, T. Moriwaki and P. Naumov, *J. Am. Chem. Soc.*, 2017, **139**, 2318.
28 M. J. Turner, S. P. Thomas, M. W. Shi, D. Jayatilaka and M. A. Spackman, *Chem. Commun.*, 2015, **51**, 3735.

4.2. Supporting Information

Hand-twistable plastically deformable crystals of a rigid small organic molecule

Lukman O. Alimi, Prem Lama, Vincent J. Smith and Leonard J. Barbour*

Materials

4-bromobenzonitrile was purchased from Sigma-Aldrich and used as received without further purification.

Crystallisation of 4-bromobenzonitrile

Crystals of 4-bromobenzonitrile were obtained by sublimation at 50 °C for 3 hrs using glass oven under dynamic vacuum (0.02 mbar). For the X-ray diffraction study of 4-bromobenzonitrile, a small colourless block was cut from a long crystal.

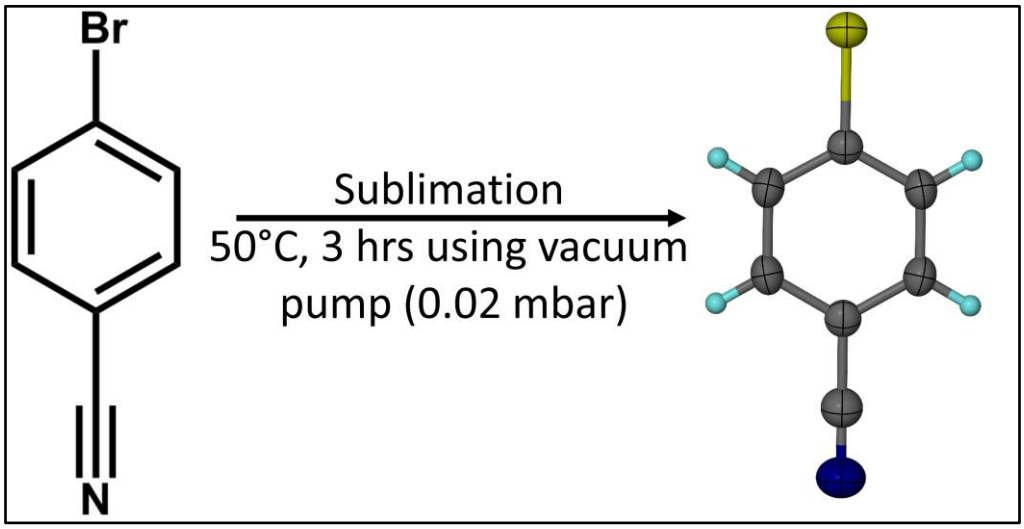

Scheme S1: Crystallisation of the organic compound 4-bromobenzonitrile.

Preparation of the single crystal of 4-bromobenzonitrile (4-BBN-S)

A very suitable, straight and rectangular crystal of 4-bromobenzonitrile was selected for the single crystal X-ray diffraction (SCXRD) analysis. The crystal was glued on the glass fibre using epoxy and the SCXRD data were collected.

Preparation of the bent crystals of 4-bromobenzonitrile (4-BBN-B)

The same single crystal was bent using mechanical force before data collection (figure S1).

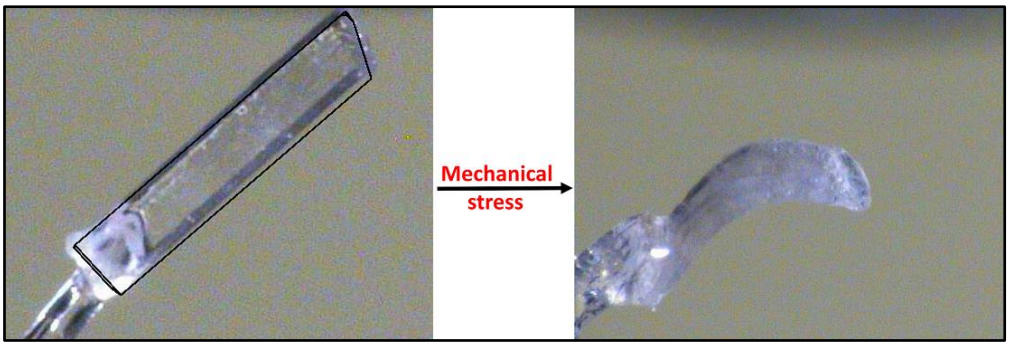

Figure S1: Images showing straight and bent crystal for SCXRD analysis.

Computational Analysis

Crystal structures of 4-bromobenzonitrile at 273 K were imported from the refined crystal structures. Only the hydrogen atoms in the framework were optimized as part of a periodic system using the CASTEP module of the Materials Studio software suite.[1] The optimizations were performed using the GGA PBE functional with Grimme's DFT-D dispersion correction, and thresholds for geometry optimization and SCF convergence were chosen as 1×10^{-5} and 1×10^{-6} eV, respectively. Single point energy calculations using the DMol3 module of the Materials Studio software suite were performed using the GGA PBE functional with Grimme's DFT-D dispersion correction, and threshold for SCF convergence were chosen as 1×10^{-6} eV. The electron density data obtained from the DMol3 calculations were used to construct the three-dimensional 0.01 e^{-} $Å^{-3}$ electron density contour used for the molecular electrostatic potential map (obtained from the same calculation).

From the calculation, we found that if we consider only an individual 4-bromobenzonitrile, negative electrostatic potential is observed at the center of benzene ring due to the presence of -CN and -Br groups (Figure S2a). As a result, the molecules should not stack in face to face fashion because of the repulsive interactions. However, on considering the overall packing of 4-bromobenzonitrile, the interactions from neighbouring molecules affect the electron density distribution on the benzene ring i.e. the π-clouds (shifted to negative electron density at the two ends of the molecule (Figure S2b) and as a result the center of the benzene ring becomes slightly positive. Overall, 4-bromobenzonitrile are arranged in polar mode, therefore in order to stabilise the system i.e. to minimise repulsion, the molecules have to stack in an offset manner so that the positive aromatic center interacts with the negative π-cloud on the neighbouring molecule.[2] Hence, the offset π···π stacking[2,3,4,5] is observed in the system.

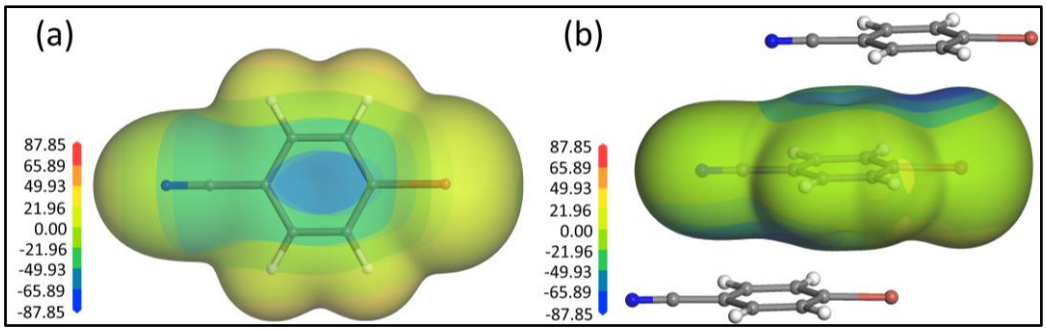

Figure S2: Electrostatic potential mapped onto the electron density isosurface of (a) the molecule and (b) the molecules in the crystal packing showing the offset π···π interactions. Electrostatic potentials are in kcal/mol. Areas of positive and negative potentials are indicates in red and blue respectively.

Table S1. Crystallographic details for straight (**4-BBN-S)** and bent (**4-BBN-B)** crystals.

Identification code	**4-BBN-S**	**4-BBN-B**
Empirical formula	C_7H_4NBr	C_7H_4NBr
Formula weight (g/mol)	182.02	182.02
Temperature/K	273(2)	273(2)
Crystal system	Monoclinic	Monoclinic
Space group	*Cm*	*Cm*
a/Å	9.5310(20)	9.5090(50)
b/Å	8.5593(18)	8.5350(70)
c/Å	4.1352(9)	4.1270(20)
α/°	90	90.00
β/°	90.295(3)	90.311(5)
γ/°	90	90.00
Volume/Å^3	337.34(12)	334.9(3)
Z	2	2
ρ_{calc} (g/cm^3)	1.792	1.805
μ/mm^{-1}	5.990	6.033
F(000)	176	176
Crystal size/mm^3	0.91 × 0.188 × 0.104	0.91 × 0.188 × 0.104
Radiation	MoKα (λ = 0.71073)	MoKα (λ = 0.71073)
θ range for data collection/°	3.199 to 28.277	3.207 to 25.332
Index ranges	-12 ≤ h ≤ 12, -11≤ k ≤ 11, -5 ≤ l ≤ 5	-11 ≤ h ≤ 11, -10≤ k ≤ 10, -4 ≤ l ≤ 4
Reflections collected	3422	4129
Independent reflections	893 [R_{int} = 0.0463, R_{sigma} = 0.0337]	657 [R_{int} = 0.0313, R_{sigma} = 0.0189]
Data/restraints/parameters	893/2/49	655 / 2 / 49
Goodness-of-fit on F^2	1.087	1.029
Final R indexes [I>=2σ (I)]	R_1 = 0.0596, wR_2 = 0.1518	R_1 = 0.0404, wR_2 = 0.1010
Final R indexes [all data]	R_1 = 0.0613, wR_2 = 0.1534	R_1 = 0.0408, wR_2 = 0.1019
Largest diff. peak/hole /e Å^{-3}	0.667/-0.236	0.601 / -0.218
CCDC number	1587640	1587641

Table S2: Intermolecular interactions within the structure responsible for bending in 4-bromobenzonitrile.

	π···π (*i*1···*i*1) distance (Å)	**N1···Br1 (d) (Å)**	**C5-N1···Br1 (D) (Å)**	**∠ C5-N1···Br1 (θ) (°)**	**C1-Br1···N1 (D) (Å)**	**∠ C1-Br1···N1 (θ) (°)**	**Closest vdW H_2···H_3 (Å)**	**Closest C2···C3 contact (Å)**
4-BBN-S	4.1352(9)	3.2540(6)	4.3571(8)	166.546(9)	5.1170(1)	167.995(8)	2.9561(9)	4.0578(7)
4-BBN-B	4.1268(20)	3.2510(14)	4.3563(19)	167.636(20)	5.1241(22)	168.479(14)	2.9718(12)	4.0655(15)

***i*1** is the centroid of C1- C6

Table S3: Other shortest non-bonding distances and angles between the molecules**.**

	(D···A) C3-H3···Br1 (Å)	**(∠D-H···A) ∠C3-H3···Br1 (°)**	**(D···A) C2-H2···N1 (Å)**	**(∠D-H···A) ∠ C2-H2···N1 (°)**	**C···π (Å)**	**Br···π (Å)**
4-BBN-S	3.7845(6)	125.566(6)	3.7027(6)	151.009(6)	3.7027(7)	3.6989(7)
4-BBN-B	3.7762(13)	125.067(13)	3.7018(13)	151.166 (13)	3.6585(16)	3.7019(15)

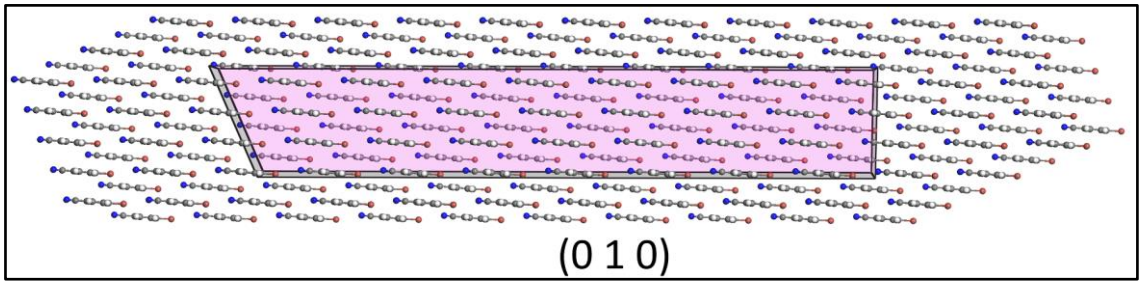

Figure S3: Overlay of crystal habit with the crystal packing along (0 1 0) plane.

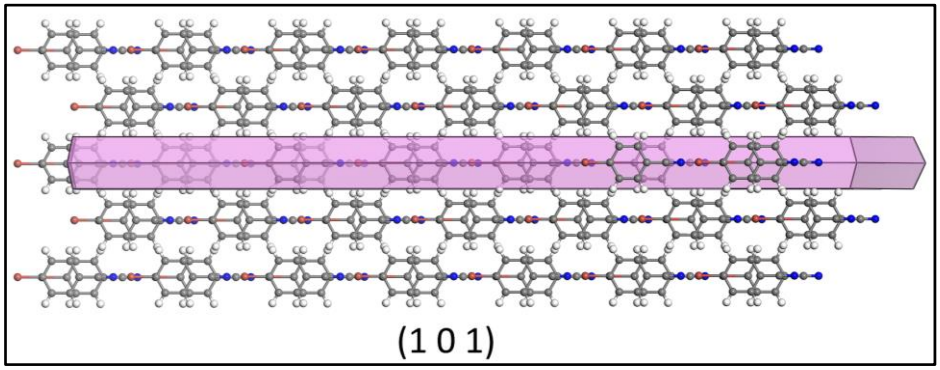

Figure S4: Overlay of crystal habit with the crystal packing along (1 0 1) plane.

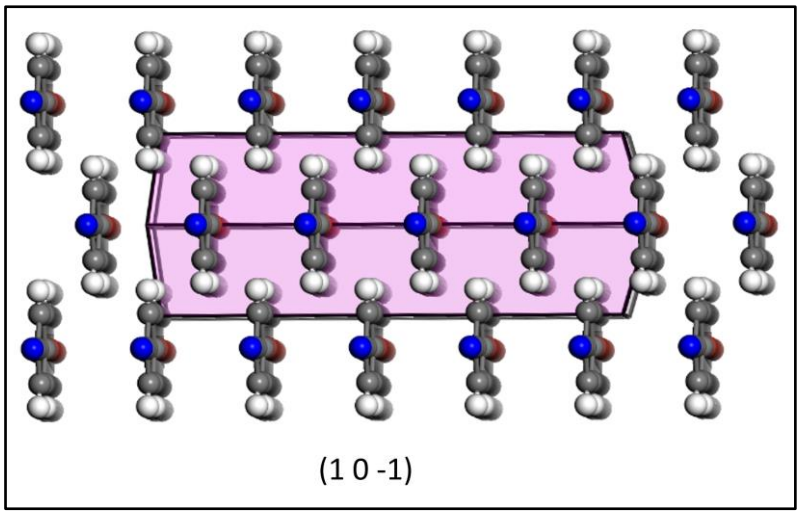

Figure S5: Overlay of crystal habit with the crystal packing along (1 0 -1) plane.

Mechanical bending of the 4-bromobenzonitrile crystal

This mechanical bending of 4-bromobenzonitrile was recorded with the PIXEL camera mounted on a stereo zoom SMZ74 5T trinocular stereoscope using Windows Movie Maker software. This was carried out at room temperature (Movies S1).

Figure S6: Micrographs showing the mechanical bending of 4-bromobenzonitrile crystal.

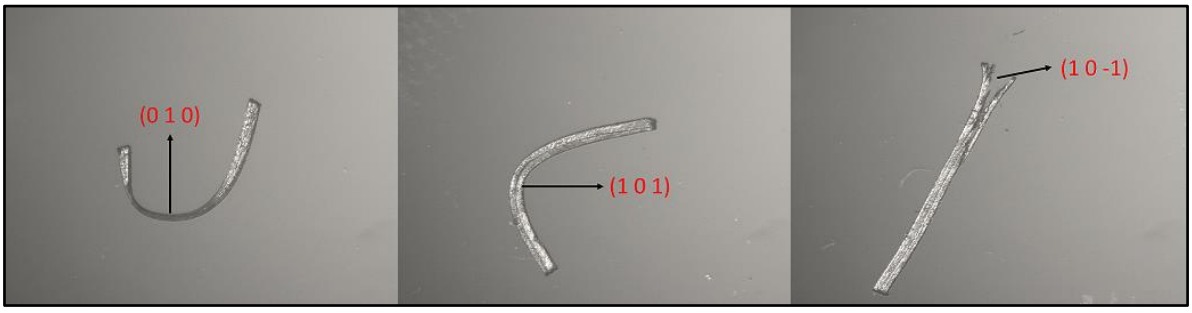

Figure S7: Micrographs of 4-bromobenzonitrile crystal showing the mechanical bending on (0 1 0) and (1 0 1) faces but splitting/breaking on (1 0 -1) face.

Differential Scanning Calorimetry (DSC)

Temperature-ramped differential scanning calorimetry of 4-bromobenzonitrile was carried out on TA DSC-Q20 and DSC-Q100 instrument. Crystals were taken on a Tzero aluminium pan and connected to LNG cryostat for low temperature analysis. The low temperature DSC analysis was carried out by cooling from 300 to 100 K and heated back to 300 K at the heating rate of 5 K min^{-1}. Also, the crystal was analysed by heating from room temperature (300 K) to the selected temperature at the ramp rate of 5 K min^{-1}.

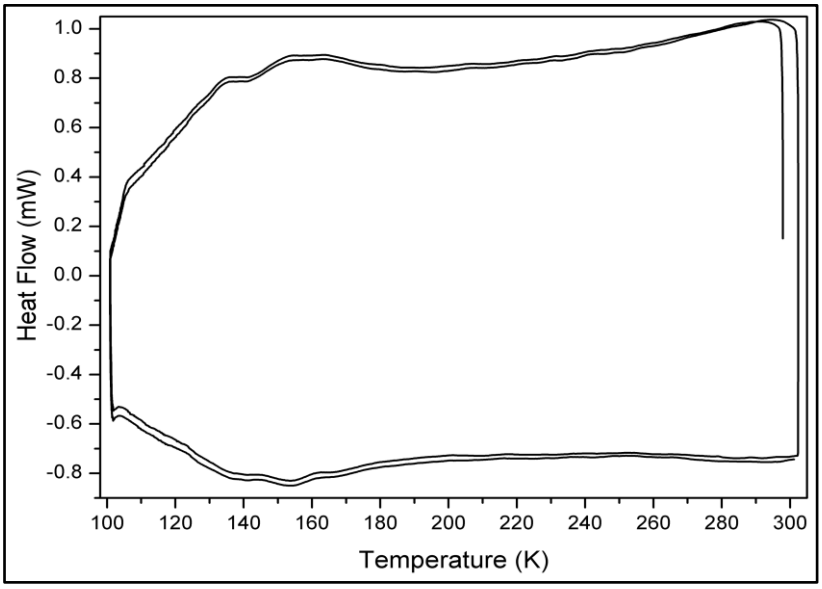

Figure S8: T-DSC curve for 4-bromobenzonitrile in the range of 100-300 K (two cycles).

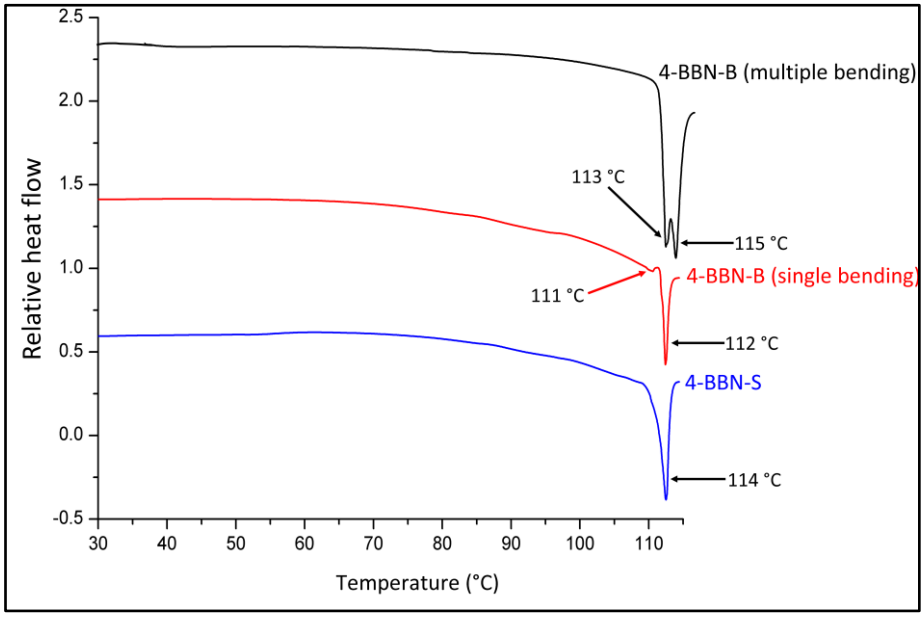

Figure S9: T-DSC thermograms showing the melting points of both straight and bent crystal.

Hot stage Microscopy

Thermomicroscopic behaviour of 4-bromobenzonitrile was observed with hot-stage microscope (Linkam) consisting of a temperature-controlled stage THMS600-PS mounted on a Q-imaging (Q32634) microscope. Crystal of 4-bromobenzonitrile was cooled from room temperature (300 K) to 100 K and heated back to room temperature at a constant heating rate of 5 K min^{-1}. High-speed recordings were obtained with PIXEL camera mounted on a stereo zoom SMZ745T trinocular stereoscope (Movies S2 and S3).

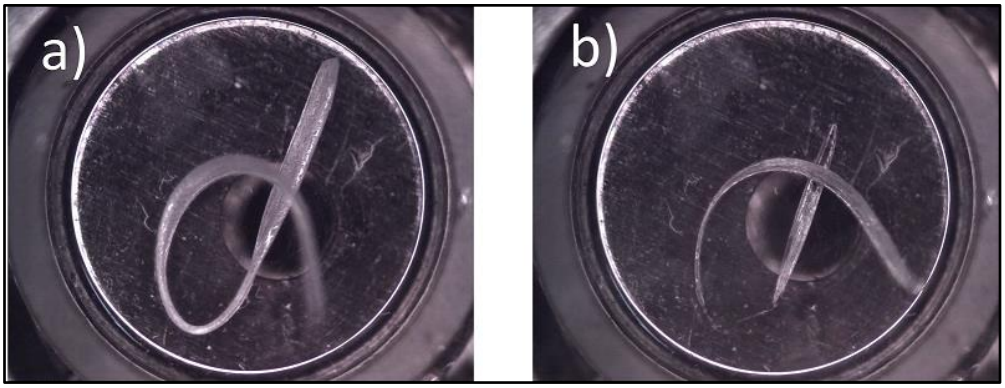

Figure S10: Micrographs showing **a)** bent crystal before melting and **b)** the melting of the bent area of the crystal before other part.

Single crystal structure determination

Single-crystal X-ray diffraction data were collected at 273 K using a Bruker APEX-II DUO CCD area detector diffractometer equipped with an Oxford Cryosystems 700Plus cryostat. A multilayer monochromator with Mo Kα radiation (λ = 0.71073 Å) from an Incoatec IμS micro source was used. Data reduction was carried out by means of a standard procedure using the Bruker software package SAINT.[6] Absorption corrections and correction of other systematic errors were performed using SADABS.[7,8] The structures were solved by direct methods using SHELXS-2016 and refined using SHELXL-2016.[9] X-Seed[10] was used as the graphical interface for the SHELX program suite and the images were rendered with POV-Ray. Hydrogen atoms were placed in calculated positions using riding models.

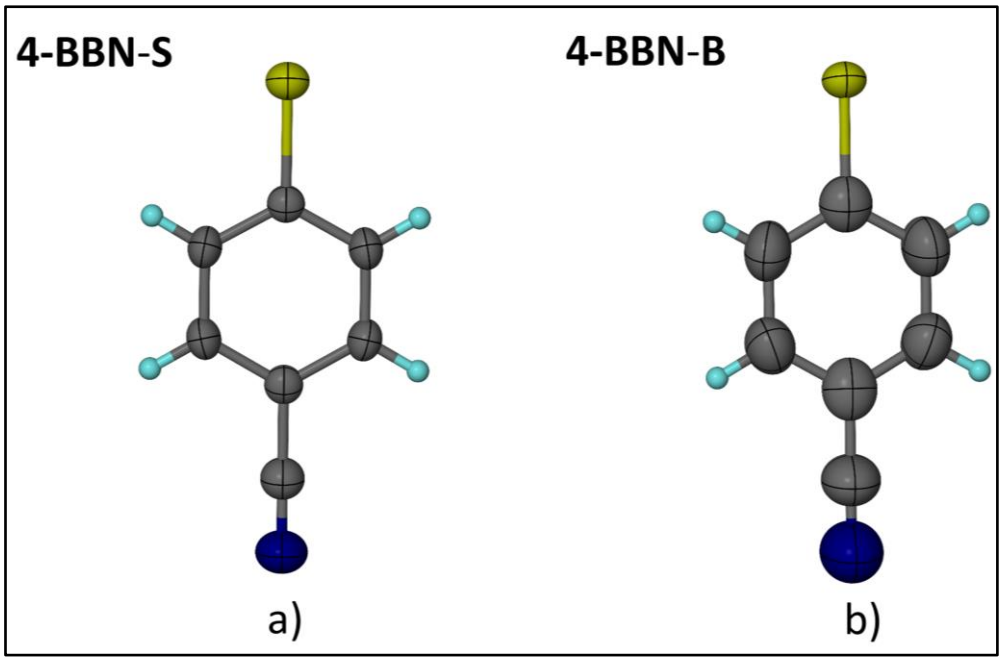

Figure S11: ORTEP representation with 50% probability for a) **4-BBN-S** and b) **4-BBN-B** at 273 K.

Infra-red spectroscopy

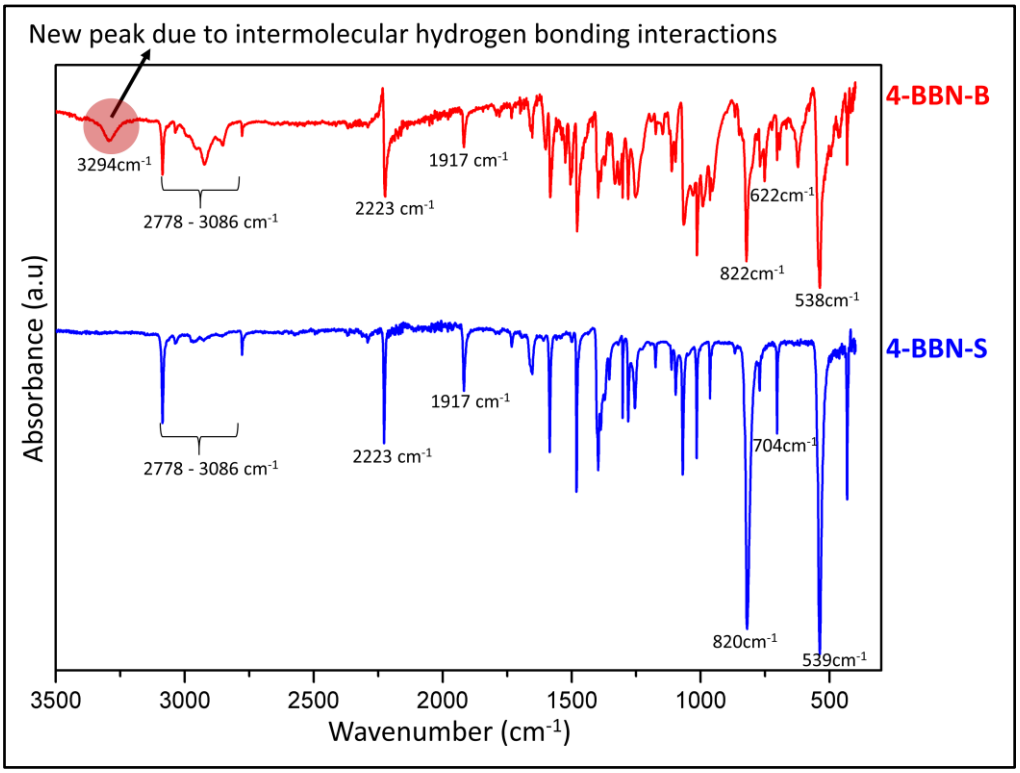

Figure S12: IR spectra of straight and bent crystals of 4-bromobenzonitrile.

4.3. References

1. Materials Studio Modelling Environment, Version 6.0.0; Accelrys Software Inc.: San Diego, 2011.

2. a) C. A. Hunter, K. R. Lawson, J. Perkins and C. J. Urch. *J. Chem. Soc., Perkin Trans*. 2001, **2**, 651; b) C. A. Hunter and J. K. M. Sanders, *J. Am. Chem. Soc*., 1990, **112**, 5525.

3. M. J. Rashkin and M. L. Waters, *J. Am. Chem. Soc*., 2002, **124**, 1860.

4. J. -C. Dai, S. -M. Hu, X. -T. Wu, Z. -Y. Fu, W. -X. Du, H. -H. Zhang and R. -Q. Sun. *New J. Chem*., 2003, **27**, 914.

5. C. Janiak, *J. Chem. Soc., Dalton Trans*., 2000, 3885.

6. *SAINT Data Reduction Software*, Version 2017.3-RC2; Bruker AXS 2005-2017.

7. *SADABS*, Version 2.05; Bruker AXS Inc.: Madison, WI, 2002.

8. R. H. Blessing, *An Empirical Correction for Absorption Anisotropy*. *Acta Crystallogr., Sect. A: Found. Crystallogr*. 1995, **51**, 33.

9. G. M. Sheldrick, A Short History of SHELX. *Acta Crystallogr., Sect. A: Found. Crystallogr*. 2008, **64**, 112.

10. L. Barbour, X-Seed − *A Software Tool for Supramolecular Crystallography*. *J. Supramol. Chem*. 2001, **1**, 189.

Chapter 5: Reversible thermosalience of 4-aminobenzonitrile

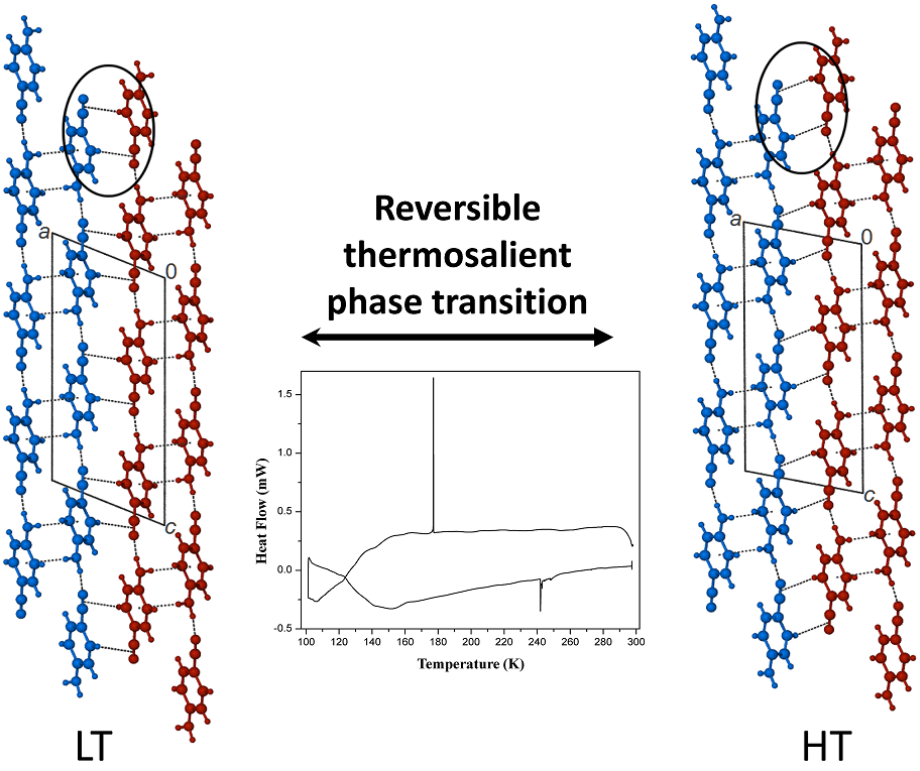

5.1. Communication in chemical communications (Published)

Contributions of the main author:

- Design of the project with Dr Vincent J. Smith
- Crystallisation of the material
- Preparation of the crystal for single-crystal X-ray data
- Recording of DSC thermograms
- Recording of Hot stage micrographs
- Recording of variable-temperature PXRD patterns
- Collection of variable-temperature single-crystal X-ray data
- Solution and refinement of single-crystal X-ray structures
- Computational analysis with Dewald P. van Heerden
- Interpretation of results with Dr Prem Lama and Dr Vincent J. Smith
- Writing the first draft of the article.

ChemComm

COMMUNICATION

View Article Online
View Journal | View Issue

Cite this: *Chem. Commun.*, 2018, 54, 6208

Received 5th May 2018,
Accepted 22nd May 2018

DOI: 10.1039/c8cc03636e

rsc.li/chemcomm

Reversible thermosalience of 4-aminobenzonitrile†

Lukman O. Alimi, Dewald P. van Heerden, Prem Lama, Vincent J. Smith and Leonard J. Barbour *

Crystals of 4-aminobenzonitrile grown by sublimation undergo reversible thermosalient phase changes during cooling and subsequent heating. Single-crystal diffraction studies have been carried out at 20 K intervals during cooling from 300 to 100 K in order to explain the structural change that occurs.

Our pursuit of new insights into anomalous thermal and mechanical behaviour of crystals spans the past decade.[1] As part of this still ongoing work, we recently reported on the anomalous thermal expansion of a co-crystal of 4-aminobenzonitrile (ABN, Scheme 1) and 4-dimethylamino-benzonitrile.[2] Even more recently we reported unusual plastic bending of crystals of 4-bromobenzonitrile.[3] These studies were inspired by previous reports from which we inferred that crystals of small 4-substituted benzonitrile molecules might exhibit interesting thermal[4] and mechanical[5] phenomena that merit in-depth structural investigation.

In 1982 Merlino and Sartori reported the crystal structure of ABN at room temperature, but they did not disclose how the crystals were grown.[4a] Twelve years later, as part of a broader structural study of five compounds, Heine *et al.* crystallised ABN from tetrahydrofuran at 255 K (presumably in a freezer) and determined a crystal structure at 153 K.[4b] They noted that their structure (in $P2_12_12_1$) was a polymorph of that reported by Merlino and Sartori (in $P2_1/c$) and assumed that a temperature-induced phase transition occurs between room temperature and 255 K. However, in 2013 Islor *et al.* redetermined the crystal structure of ABN at 200 K and reported[4c] a structure similar to that of Merlino and Sartori; the crystals were grown from an ethanolic solution at room temperature. Since they did not observe the phase transition claimed by Heine *et al.*, they suggested that rapid cooling of the crystal to 200 K preserves the monoclinic phase. We now report a detailed investigation of ABN in the temperature range 300 to 100 K and provide a correction of previous assumptions related to the thermal behaviour of the $P2_1/c$ phase. By employing complementary techniques such as X-ray diffraction, hot-stage microscopy and differential scanning calorimetry (DSC) we have noted that the monoclinic phase exhibits previously overlooked thermal expansion properties and a reversible phase transition accompanied by thermosalience during both heating and cooling.

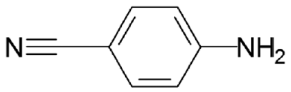

Scheme 1 Molecular structure of 4-aminobenzonitrile (ABN).

Department of Chemistry and Polymer Science, University of Stellenbosch, Matieland, 7602, South Africa. E-mail: ljb@sun.ac.za

† Electronic supplementary information (ESI) available. Crystallographic information files CCDC 1816748–1816750, 1816752–1816759 and 1816762 experimental methods, DSC, hot stage microscopy images, PXRD, intermolecular interactions, thermal expansion and computational details. For ESI and crystallographic data in CIF or other electronic format see DOI: 10.1039/c8cc03636e

Thermosalience refers to the phenomenon whereby crystals jump or explode as a result of the sudden release of strain accumulated during thermal cycling.[6] Such materials have potential applications as thermal sensors and actuators.[7,8] The thermosalient effect is a kinematically complex, two-stage process.[9] It involves the application of thermal stress (either heating or cooling) with concomitant accumulation of strain build-up in the crystal, followed by a sudden release of the strain through rapid structural transformation. The crystal then either jumps or disintegrates due to a sudden deformation of its shape. The thermosalient effect has been associated with the lack of strong three-dimensional hydrogen-bonded networks,[9,10] although it has been suggested that weak intermolecular interactions play a key role in the mechanical properties of these crystals.[9] The relationship between the types and strengths of intermolecular interactions (and the associated mechanical effects) is complicated and structure-specific.[11]

Diffraction-quality single crystals of ABN were grown by sublimation under dynamic vacuum (0.02 mbar) at 60 °C (Fig. S1, ESI†). A suitable crystal was selected and unit cell determination at room temperature by means of single-crystal diffraction (SCD) analysis yielded similar monoclinic parameters to those reported by Merlino and Sartori,[4a] and Islor *et al.*[4c] A crystal of

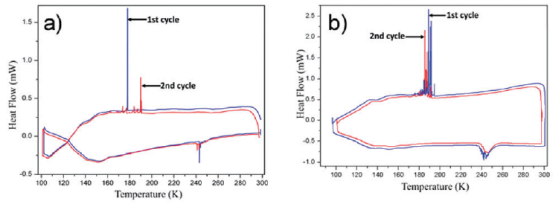

Fig. 1 DSC thermograms for (a) a single crystal and (b) bulk crystals of ABN. In each case the thermogram shows two cooling/heating cycles.

ABN was subjected to DSC analysis involving two cooling/heating cycles in the range 300 to 100 K (see ESI† for details). A single sharp exothermic peak occurs with an onset temperature of 177 K during the cooling leg of the first cycle, followed by a set of sawtooth endothermic peaks spanning the range 242 to 249 K during subsequent heating (Fig. 1). We note that Naumov and co-workers[9,10] have stated that sawtooth peaks in a DSC thermogram are indicative of thermosalience. During the second cooling/heating cycle, the thermogram shows sawtooth exothermic (161 to 190 K) and endothermic peaks (241 to 258 K) during both cooling and heating, respectively. We attribute the occurrence of sawtooth peaks in both legs of the second cycle to fragmentation of the single crystal during the exothermic event of the first cycle. To substantiate this claim, we carried out similar DSC measurements on a bulk sample consisting of several single crystals; the resulting thermogram shows sawtooth exothermic and endothermic peaks during cooling and heating in both cycles.

The thermal behaviour of ABN was also investigated by means of hot-stage microscopy in the range 300 to 100 K (ESI†). The micrographs show that the crystal disintegrates into several small fragments at 164 K during cooling, leaving only a few of these fragments in the field of view (Fig. S3 and Video S1, ESI†). During subsequent heating, the fragments jump when the temperature reaches 243 K, and these observations reinforce the conclusions drawn from the DSC analysis. In a second hot-stage experiment a crystal was coated with paratone oil before being subjected to a cooling/heating cycle (Fig. S4 and Video S2, ESI†). During cooling, the entire crystal jumped (174 K), without disintegrating, and during heating it moved slightly when the temperature reached 231 K. Variable temperature powder X-ray diffraction (with Pawley refinement of the profiles) was also carried out for ABN by cooling the sample from 300 to 100 K and recording data at 20 K intervals (Fig. S5 and S6, ESI†). The diffractograms show that the high-temperature phase persists in the temperature range 300 to 180 K, with gradual shifting of the peaks to higher 2θ, which is consistent with positive thermal expansion of the material. At 160 K it appears that a second phase begins to emerge, and that this new phase prevails in the range 140 to 100 K. These results are also consistent with the DSC analysis.

Variable temperature single-crystal X-ray diffraction analysis was also carried out in the range 300 to 100 K at 20 K intervals (see ESI† for details) with a view to elucidating the structural nature of the thermosalient phase change that occurs between 180 and 160 K upon cooling. A suitable crystal was glued to the tip of a glass fibre and then covered with a thin layer of epoxy to prevent it from jumping off the mount (Fig. S7, ESI†). The space group $P2_1/c$ is retained throughout the entire temperature range investigated and variation of the unit cell parameters a, b and c do not indicate an obvious phase transition. However, the β angle experiences a relatively large change from 101.740(2)° at 180 K to 113.088(7)° at 160 K, and this discontinuity is the most dramatic indication of the phase transition. After diffraction data were recorded at 100 K, the crystal was warmed to 300 K at a rate of 5 K min^{-1}. Redetermination of the crystal structure at 300 K (see ESI†) shows that the phase transition is enantiotropic.[12]

The thermal expansion coefficients of the two monoclinic forms of ABN were calculated using PASCal[13] (see ESI† for details). The coefficients of the principal axes for the range 300 to 180 K (*i.e.* before the phase change) $X1$ [0.5836, 0.0000, 0.8121], $X2$ [0.0000, −1.0000, 0.0000] and $X3$ [0.9983, 0.0000, −0.0580] are 24.8, 61.3 and 138.2 MK^{-1}, respectively. The volumetric thermal expansion coefficient α_v = 225.1 MK^{-1} represents a decrease of approximately 3.0% in the overall volume of the material upon cooling from 300 to 180 K. Over the temperature range 160 to 100 K, the thermal expansion coefficients along the principal axes $X1$ [0.0000, 1.0000, 0.0000], $X2$ [−0.7573, 0.0000, 0.6531] and $X3$ [0.9423, 0.0000, 0.3349] are 10.9, 54.8 and 174.7 MK^{-1}, respectively. The volumetric thermal expansion coefficient α_v = 250 MK^{-1} represents a decrease of approximately 1.5% in the overall volume upon cooling from 160 to 100 K.

It is necessary to compare the crystal structures of ABN determined at 180 and 160 K in order to rationalise the nature of the phase transition. The packing modes of the two forms are strikingly similar, and Hirshfeld surface analysis[14] was used to identify the most prominent intermolecular interactions (see ESI† and Video files S3 and S4). At 180 K these comprise relatively weak N–H···N≡C (N···N = 3.205(2) Å), N–H···π_{Ar} (N···centroid$_{Ar}$ = 3.46 Å) and C–H···$\pi_{C\equiv N}$ (C···centroid$_{C\equiv N}$ = 3.78 Å) hydrogen bonds (Table S2, ESI†). The N–H···N≡C hydrogen bonds link the molecules into one-dimensional strands along [001] in a head-to-tail fashion (Fig. 2a), and neighbouring strands are packed to form polar layers parallel to (001). No obvious intermolecular interactions are discernible between neighbouring strands in each such layer. However, each strand interacts with two adjacent strands of only one neighbouring layer by means of N–H···π_{Ar} bonds, thus forming a network of indirect linkages between neighbouring strands within each layer (Fig. 2b). We can thus consider the structure to consist of stacked bilayers; the two polar layers within each bilayer are arranged antiparallel relative to each other, and therefore no net dipole moment exists. Adjacent bilayers are associated by means of C–H···$\pi_{C\equiv N}$ interactions (Fig. 3a). Moreover, adjacent bilayers are offset relative to one another with respect to the normal of the bc plane, and this offset is reflected in the deviation of the β angle from 90°.

A projection of the crystal structure of ABN at 160 K (*i.e.* after the phase transition) is shown in Fig. 3b. It is apparent that each bilayer, as defined above, does not undergo significant

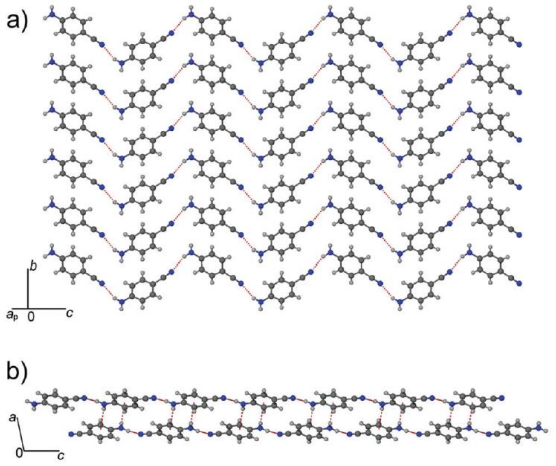

Fig. 2 Perspective views of the monoclinic form of ABN at 180 K showing (a) the formation of 1D strands (N–H···N≡C interactions) along [001], and (b) cross-linking (N–H···π_{Ar}) of these strands to form bilayers parallel to (100). Hydrogen bonds are shown as dashed red lines.

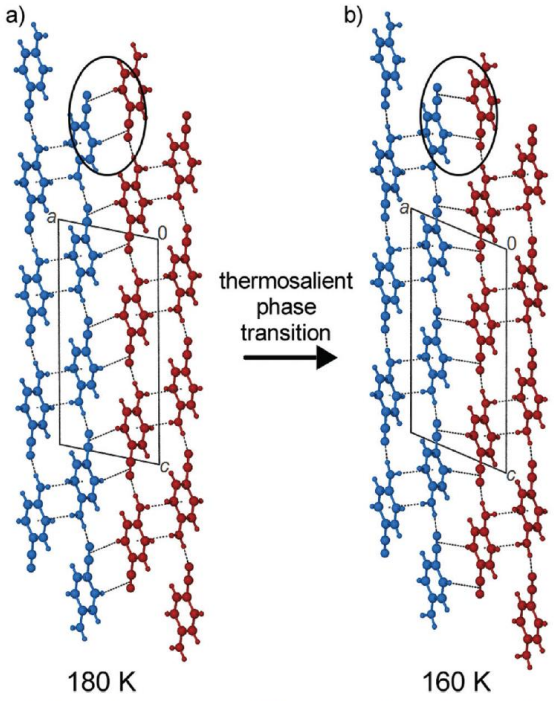

Fig. 3 Ball-and-stick projections of the two monoclinic polymorphic forms of ABN along [010] at (a) 180 K and (b) 160 K. In each case, adjacent bilayers are coloured blue and red. Hydrogen bonds are shown as dashed black lines. The structural transformation involves a shearing translation of adjacent bilayers parallel to (100). The most noticeable changes are the unit cell β angle and the orientations of the C–H···$\pi_{C\equiv N}$ interactions (encircled) between bilayers.

internal rearrangement of its constituent molecules (Fig. S13, ESI†) as a result of the phase transition. However, there is a very notable shift of adjacent bilayers by *ca.* 1.4 Å relative to one another along [001]. It is also apparent that the C–H···$\pi_{C\equiv N}$ interactions between neighbouring bilayers are maintained after the phase transition, although their geometry (*i.e.* relative orientations of the participating atoms) changes significantly, as indicated by the encircled regions in Fig. 3. The shearing translation of adjacent bilayers relative to one another accounts for the dramatic change in the crystallographic β angle from 101.740(2)° at 180 K to 113.088(7)° at 160 K. We postulate that the thermally-induced phase transition occurs rapidly and is accompanied by an abrupt change in the shape of the crystal that is commensurate with the change in the shape of the unit cell. It is reasonable to presume that this sudden macroscopic change in shape provides the necessary propulsion for the crystals to jump.

In their recent perspective on thermosalience Naumov and co-workers[15] commented that the phenomenon is almost always accompanied by small but strongly anisotropic biaxial negative linear thermal expansion. While the thermal expansion of the monoclinic phase of ABN is highly anisotropic, it is nevertheless positive along all three dimensions (both before and after the phase change). Fig. 4 illustrates the effects of thermal contraction upon ABN during cooling from 300 to 100 K; it is useful to consider the grey molecules as a reference bilayer common to both structures. Upon cooling from 300 to 180 K, the high-temperature polymorph of ABN experiences its most significant degree of thermal contraction (*i.e.* along *X*3) in a direction that is almost normal to the bilayer stacking axis. That is, as the bilayer shown in blue approaches the reference layer, it experiences a small lateral shift from right to left. The phase transition then involves a sudden shift in the opposite direction, and further cooling results in continued contraction with a gradual lateral shift of the red layer from left to right. This mechanism is similar to that exhibited by terephthalic acid and the structural change conforms to class III, as categorised by Naumov and co-workers.[9,16]

Our detailed structural studies have provided a lucid description of how the thermosalient phase change occurs. However,

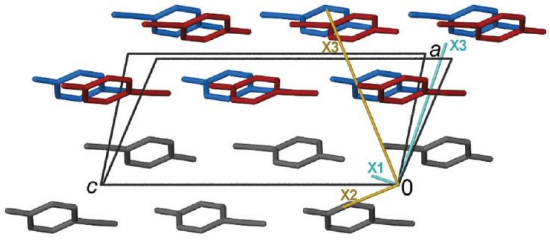

Fig. 4 Overlaid projections of the crystal structures of ABN determined at 180 and 160 K. Both structures are projected along [0−10] with their unit cell origins superimposed. The molecules shown in grey represent a bilayer common to both structures. The adjacent bilayers are shown in blue and red for the structures at 180 and 160 K, respectively. The principal axis tensors representing the thermal expansion of the two polymorphs (300 to 180 K and 160 to 100 K) are shown in light blue and orange, respectively, and are scaled according to their coefficients. Hydrogen atoms have been omitted for clarity.

side-by-side comparison of the enantiotropic crystal structures does not suggest why it occurs, and we therefore carried out a theoretical study. The lattice energies of all 11 crystal structures calculated in the temperature range 300 to 100 K (see ESI† and Fig. S14 for details) follow a gradual downward trend from −112 to −117 kcal mol^{-1}, with no discernible discontinuity between 180 and 160 K. In general, we consider all molecular crystal structures to be stabilised by an interplay between directional (*e.g.* hydrogen bonds, π interactions, *etc.*) and non-directional (van der Waals) forces. As expected, the reduced molecular footprint with cooling results in a gradual reduction of the interlayer spacing (both intra- and inter-bilayer) (Fig. S15, ESI†). This has a marked influence on the strengths of the intermolecular interactions that govern molecular packing. Our calculations show that, upon cooling from 300 K, the directional interactions of ABN strengthen, but at the expense of the van der Waals interactions (Fig. S14 and S18, ESI†). We postulate that the counterintuitive trend of the van der Waals interactions is due to a topological mismatch between adjacent bilayers that is enforced by the directional interactions. Between 180 and 160 K further progress along the contraction trajectory is no longer sustainable, thus necessitating a sudden shear translation of adjacent bilayers relative to one another (Fig. 4). The more complementary topological match between bilayers in the ensuing low-temperature phase then allows continued reduction of the interlayer spacing upon further cooling to 100 K. The intermolecular interactions within the bilayers are maintained through the phase change. However, we note a substantial increase in strength of an elongated offset $\pi_{Ar}\cdots\pi_{Ar}$ interaction between successive bilayers (Table S4 and Fig. S19, ESI†) as a result of the shearing transformation.

Our detailed structural and theoretical studies have provided new insight into the unusual and previously overlooked thermal behaviour of ABN. These results are consistent with Naumov's assertion[9,10] that thermosalience in molecular crystals is generally associated with the lack of strong hydrogen bonded networks, and that weak intermolecular interactions play an important role. In particular, our findings imply that the interplay between directional and non-directional interactions can result in the build-up of steric strain, the sudden release of which can cause a rapid structural change, which also manifests macroscopically to provide the necessary propulsion for thermosalience.

We thank the National Research Foundation of South Africa for financial support of this work and the Centre for High Performance Computing (CHPC) in Cape Town for the use of their computational resources.

Conflicts of interest

There are no conflicts to declare.

References

1 (*a*) A. Janiak, C. Esterhuysen and L. J. Barbour, *Chem. Commun.*, 2018, **54**, 3727; (*b*) E. R. Engel, V. J. Smith, C. X. Bezuidenhout and L. J. Barbour, *Chem. Mater.*, 2016, **28**, 5073; (*c*) D. P. van Heerden, C. Esterhuysen and L. J. Barbour, *Dalton Trans.*, 2016, **45**, 4141; (*d*) P. Lama, L. O. Alimi, R. K. Das and L. J. Barbour, *Chem. Commun.*, 2016, **52**, 3231; (*e*) R. K. Das, H. Aggarwal and L. J. Barbour, *Inorg. Chem.*, 2015, **54**, 8171; (*f*) W. Cai, A. Gladysiak, M. Anioła, V. J. Smith, L. J. Barbour and A. Katrusiak, *J. Am. Chem. Soc.*, 2015, **137**, 9296; (*g*) P. Lama, R. K. Das, V. J. Smith and L. J. Barbour, *Chem. Commun.*, 2014, **50**, 6464; (*h*) E. R. Engel, V. J. Smith, C. X. Bezuidenhout and L. J. Barbour, *Chem. Commun.*, 2014, **50**, 4238; (*i*) M. Lusi and L. J. Barbour, *CrystEngComm*, 2014, **16**, 36; (*j*) I. Grobler, V. J. Smith, P. M. Bhatt, S. A. Herbert and L. J. Barbour, *J. Am. Chem. Soc.*, 2013, **135**, 6411; (*k*) D. Das, T. Jacobs, A. Pietraszko and L. J. Barbour, *Chem. Commun.*, 2011, **47**, 6009; (*l*) D. Das, T. Jacobs and L. J. Barbour, *Nat. Mater.*, 2010, **9**, 36.
2 L. O. Alimi, P. Lama, V. J. Smith and L. J. Barbour, *CrystEngComm*, 2018, **20**, 631.
3 L. O. Alimi, P. Lama, V. J. Smith and L. J. Barbour, *Chem. Commun.*, 2018, **54**, 2994.
4 (*a*) S. Merlino and F. Sartori, *Acta Crystallogr.*, 1982, **B38**, 1476; (*b*) A. Heine, R. Herbst-Irmer, D. Stalke, W. Kuhnle and K. A. Zachariasse, *Acta Crystallogr.*, 1994, **B50**, 363; (*c*) A. M. Islor, B. Chandrakantha, T. Gerber, E. Hosten and R. Betz, *Z. Kristallogr.*, 2013, **228**, 217.
5 (*a*) C. M. Reddy, R. C. Gundakaram, S. Basavoju, M. T. Kirchner, K. A. Padmanabhan and G. R. Desiraju, *Chem. Commun.*, 2005, 3945; (*b*) C. M. Reddy, M. T. Kirchner, R. C. Gundakaram and G. R. Desiraju, *Chem. – Eur. J.*, 2006, **12**, 2222; (*c*) C. M. Reddy, K. A. Padmanabhan and G. R. Desiraju, *Cryst. Growth Des.*, 2006, **6**, 2720.
6 M. K. Panda, M. Etter, R. E. Dinnebier and P. Naumov, *Angew. Chem., Int. Ed.*, 2017, **56**, 8104.
7 (*a*) N. K. Nath, M. K. Panda, S. C. Sahoo and P. Naumov, *CrystEngComm*, 2014, **16**, 1850; (*b*) Z. Skoko, S. Zamir, P. Naumov and J. Bernstein, *J. Am. Chem. Soc.*, 2010, **132**, 14191.
8 S. Ghosh and C. M. Reddy, *Angew. Chem., Int. Ed.*, 2012, **51**, 10319.
9 S. C. Sahoo, M. K. Panda, N. K. Nath and P. Naumov, *J. Am. Chem. Soc.*, 2013, **135**, 12241.
10 M. K. Panda, T. Runčevski, A. Husain, R. E. Dinnebier and P. Naumov, *J. Am. Chem. Soc.*, 2015, **137**, 1895.
11 P. Naumov, S. Chizhik, M. K. Panda, N. K. Nath and E. Boldyreva, *Chem. Rev.*, 2015, **115**, 12440.
12 J. D. Dunitz, *Pure Appl. Chem.*, 1991, **63**, 177.
13 J. Cliffe and A. L. Goodwin, *J. Appl. Crystallogr.*, 2012, **45**, 1321.
14 M. A. Spackman and D. Jayatilaka, *CrystEngComm*, 2009, **11**, 19.
15 P. Commins, I. T. Desta, D. P. Karothu, M. K. Panda and P. Naumov, *Chem. Commun.*, 2016, **52**, 13941.
16 D. P. Karothu, J. Weston, I. T. Desta and P. Naumov, *J. Am. Chem. Soc.*, 2016, **138**, 13298.

5.2. Supporting Information

Reversible Thermosalience of 4-Aminobenzonitrile

Lukman O. Alimi, Dewald P. van Heerden, Prem Lama, Vincent J. Smith and Leonard J. Barbour*

Materials

4-aminobenzonitrile was purchased from Sigma-Aldrich and used as received without further purification.

Crystallisation of 4-aminobenzonitrile (ABN)

Crystals of 4-aminobenzonitrile were obtained over several days by sublimation in a glass oven at 60 °C under dynamic vacuum (0.02 mbar). A small colourless crystal was selected for the variable-temperature single-crystal X-ray diffraction study of 4-aminobenzonitrile.

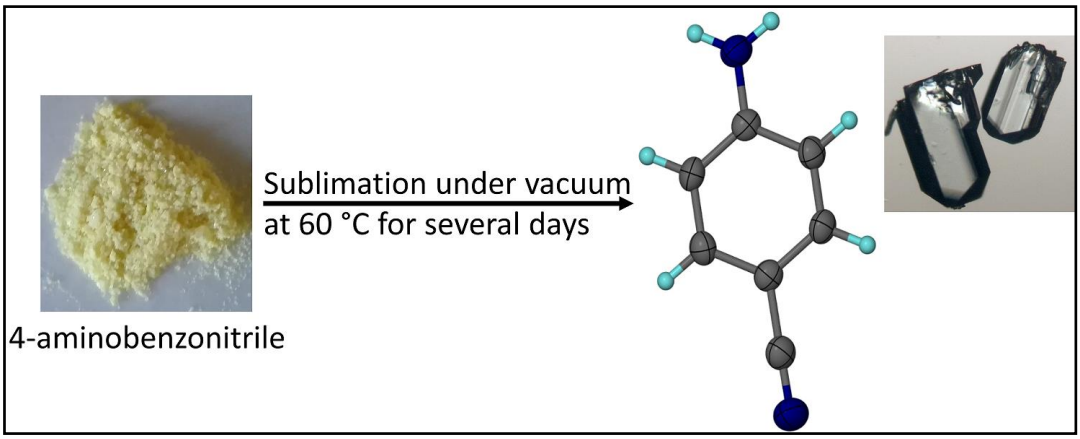

Fig. S1 Crystallisation of 4-aminobenzonitrile (ABN).

Differential Scanning Calorimetry (DSC)

DSC experiments were carried out using a TA Instruments DSC-Q100 equipped with a Liquid Nitrogen Cooling System (LNCS). Two different samples of ABN were used for the experiments: (i) a single crystal of 1.0 mg and (ii) 5.5 mg bulk crystals. In each case the sample was cooled in a standard hermetically sealed aluminium pan from 300 to 100 K and heated back to 300 K at the ramp rate of 5 K min^{-1}. Experiments were carried out under a constant flow of dry nitrogen gas at 50 ml min^{-1}. The enthalpies associated with the peaks were determined by integrating the baseline before and after the transition using the "integrate peak horizontal" command of the TA instruments Universal Analysis 2000 software.

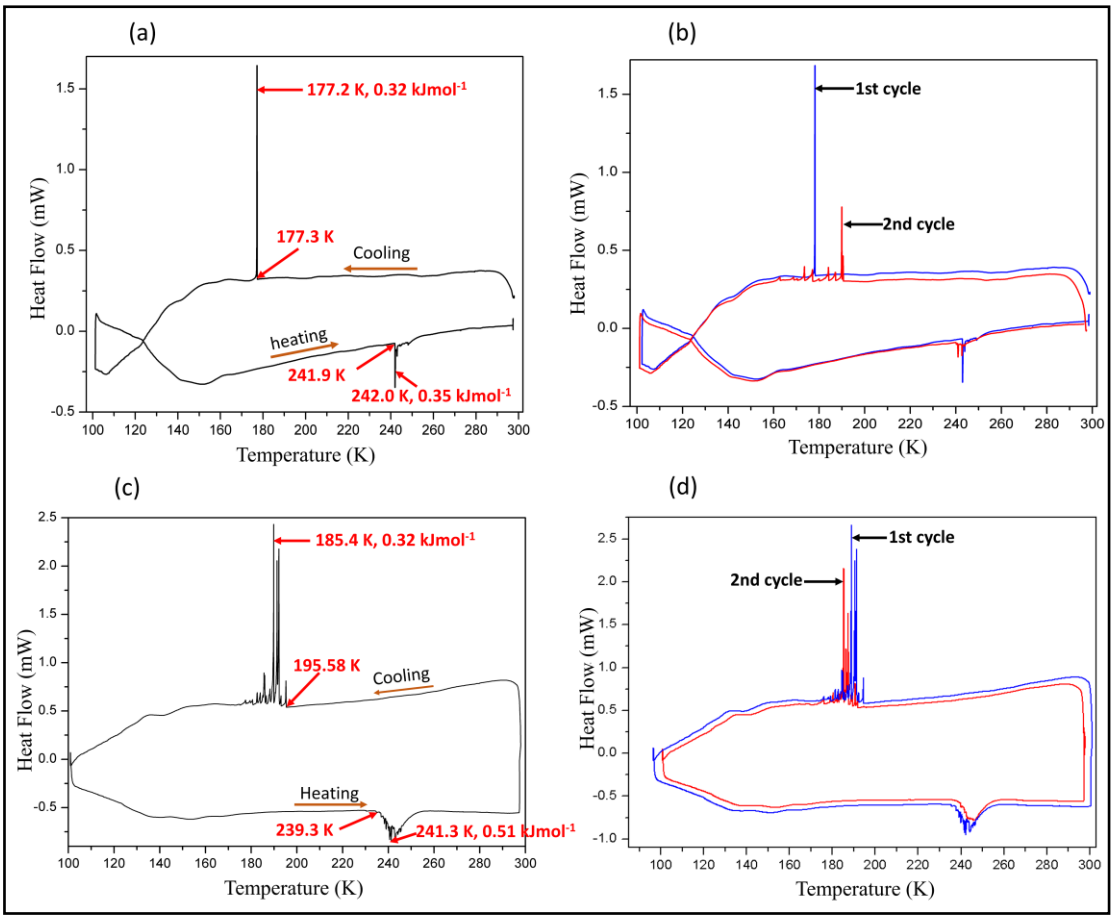

Fig. S2 DSC thermograms for ABN in the range 300 to 100 K. (a) A solitary exothermic peak is observed for a single crystal upon cooling, followed by a sawtooth-shaped endotherm upon heating. (b) Two cycles for the single crystal. (c) Sawtooth peaks during both cooling and heating for bulk crystals. (d) Two cycles for the bulk crystals.

Hot stage microscopy

The thermal behaviour of ABN was observed using a Linkam DSC-600 equipped with a Meiji MS-45D Unicam zoom macroscope and a PixelLink digital camera. A single crystal of ABN was cooled from 300 to 100 K and then heated back to 300 K at a constant rate of 5 K min^{-1}.

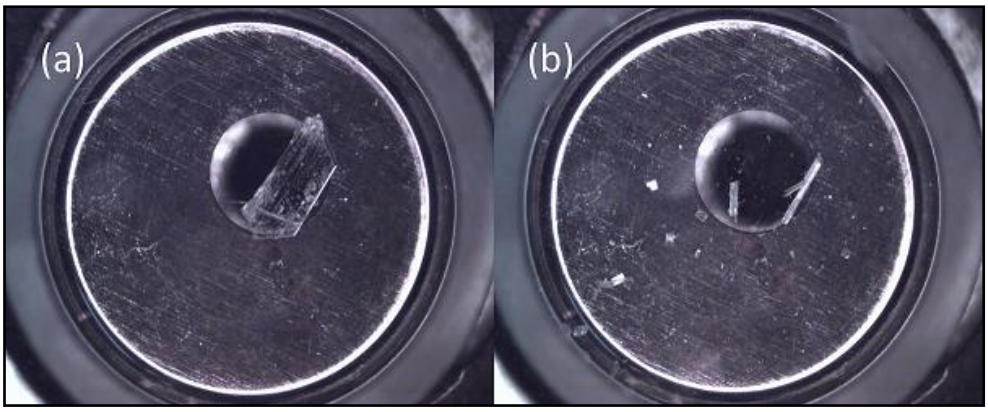

Fig. S3 Micrographs showing (a) a crystal of ABN before exploding and (b) the debris of the crystal after exploding during cooling from 300 to 100 K.

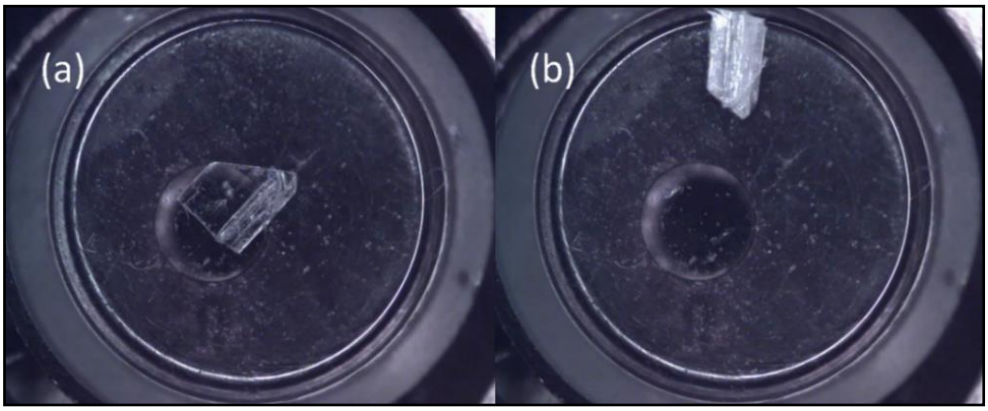

Fig. S4 Micrographs showing a crystal of coated in oil (a) before and (b) after the thermosalient event during cooling from 300 to 100 K.

Powder X-ray diffraction

Variable temperature powder X-ray diffraction data were recorded using Cu Kα radiation (λ = 1.5418 Å, 40 kV and 30 mA) on a PANalytical X'pert PRO instrument operating in Bragg-Brentano geometry. The temperature was controlled by means of a short-nozzle Oxford Cryosystems Cryostream 700Plus cryostat. Samples were placed in sealed glass capillaries (0.5mm) and data were recorded from 300 to 100 K at 20 K intervals. Pawley refinement was carried out using TOPAS[1] version 4.2.

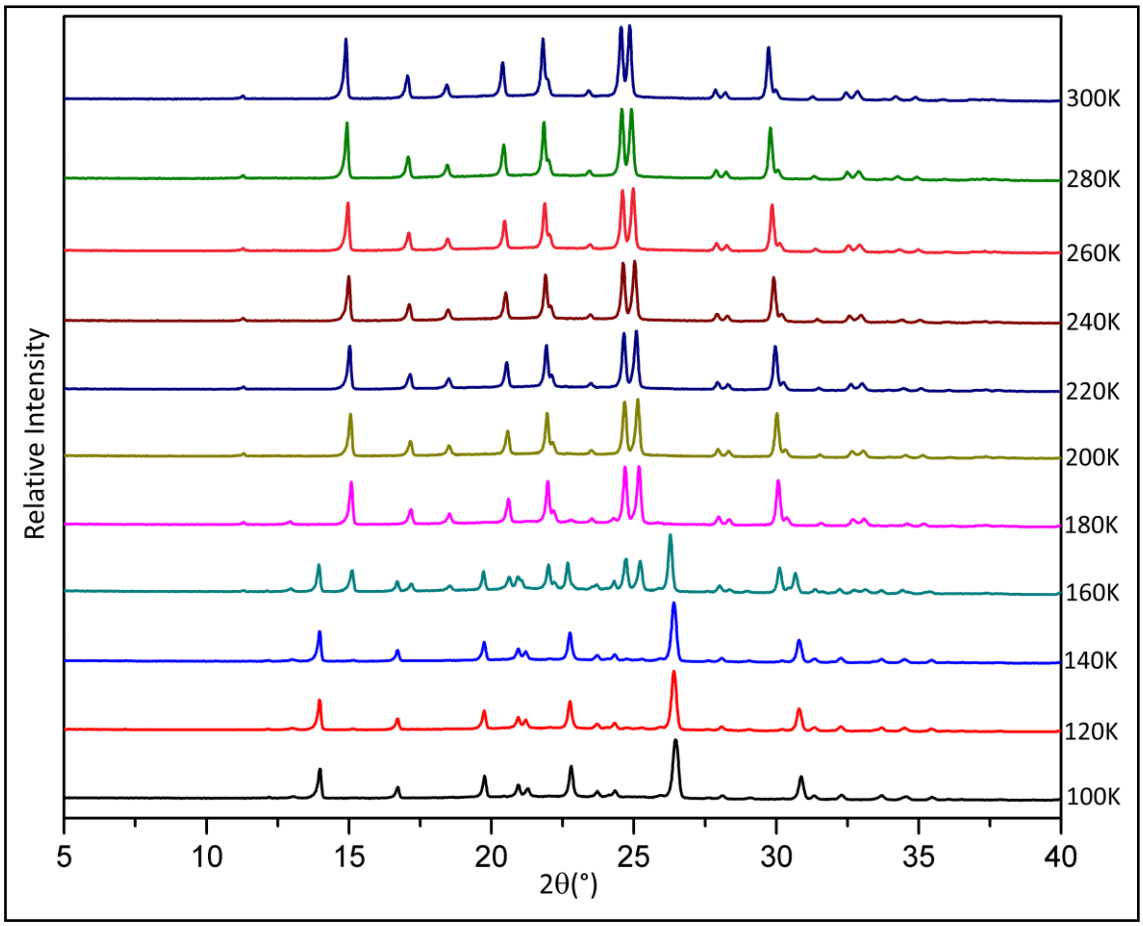

Fig. S5 Variable-temperature PXRD patterns of ABN showing the phase change after 180 K.

(a)

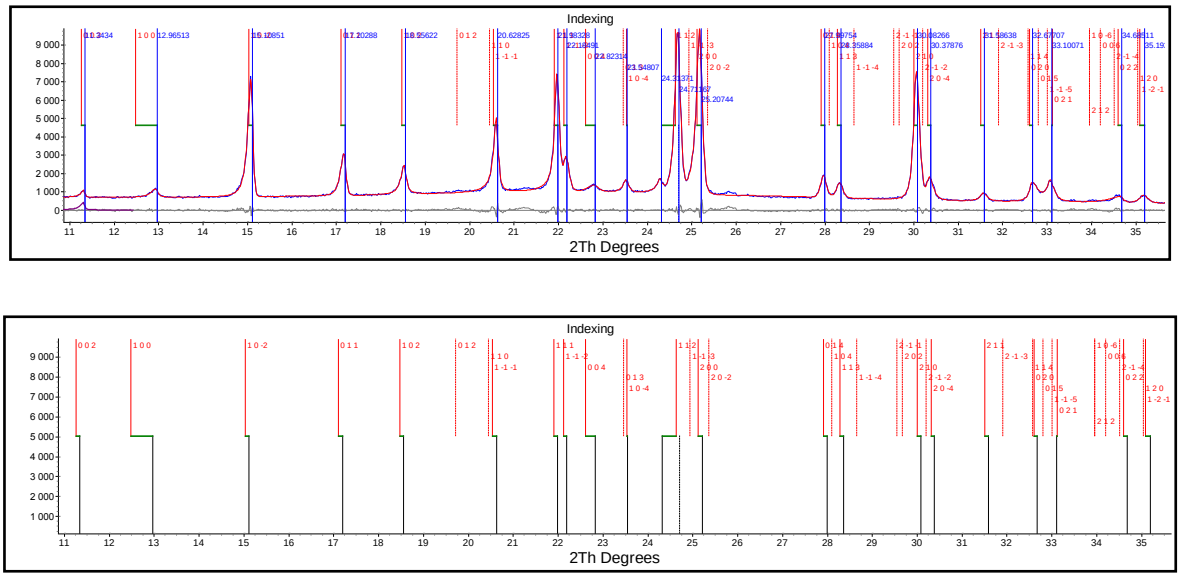

(b)

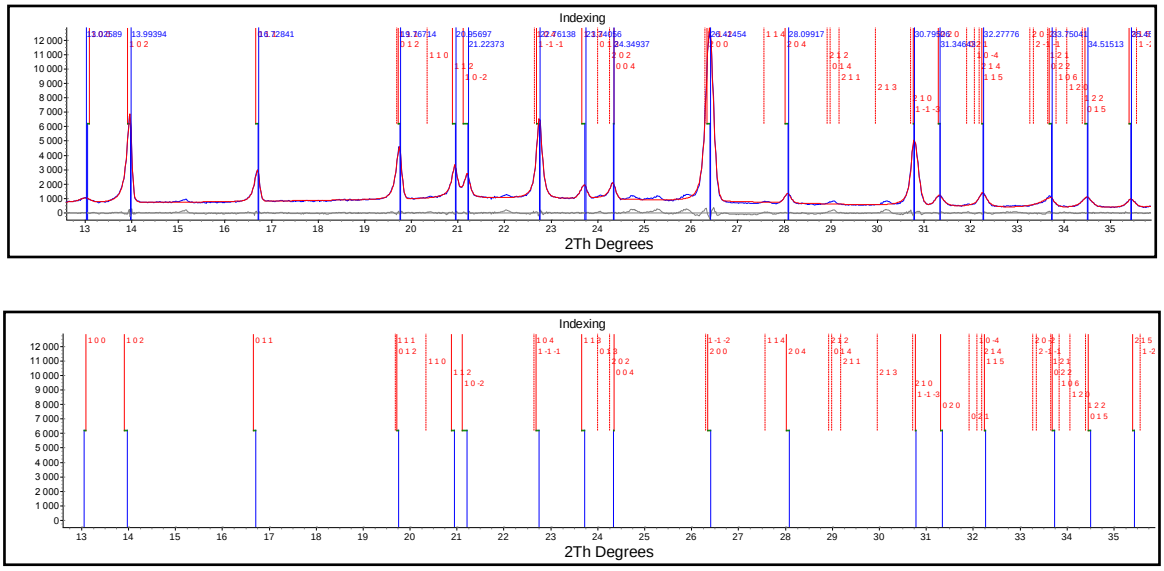

Fig. S6 Pawley refinement of the PXRD patterns of ABN at (a) 180 and (b) 140 K.

Single crystal X-ray diffraction measurements

Single crystal X-ray diffraction data were recorded using a Bruker D8 Venture diffractometer equipped with a Photon II CPAD detector and an Oxford Cryosystems Cryostream 800Plus cryostat. The crystal was carefully covered with thin layer epoxy to prevent it from jumping off the mount (see Fig. S7). A multilayer monochromator with Mo Kα radiation (λ = 0.71073 Å) from an Incoatec IμS micro source was used. Data reduction was carried out by means of a standard procedure using the Bruker software package SAINT,[2] and absorption corrections and correction of other systematic errors were performed using SADABS.[3,4] The structures were solved by direct methods using SHELXS-2016 and refined using SHELXL-2016.[5] X-Seed[6] was used as the graphical interface for the SHELX program suite. Aromatic hydrogen atoms were placed in calculated positions using riding models. Since there is no standard model for amine hydrogen atoms, these atoms were identified in difference electron density maps and refined with a N–H bond-length restraint of 1.02(2) Å (based on a survey of the CSD where structures were determined by means of neutron diffraction).

Using the same crystal, data were recorded at 20 K intervals during cooling in the range 300 to 100 K. Thereafter, the crystal was warmed to 300 K before a final data set was recorded (to check for reversibility of the phase transition).

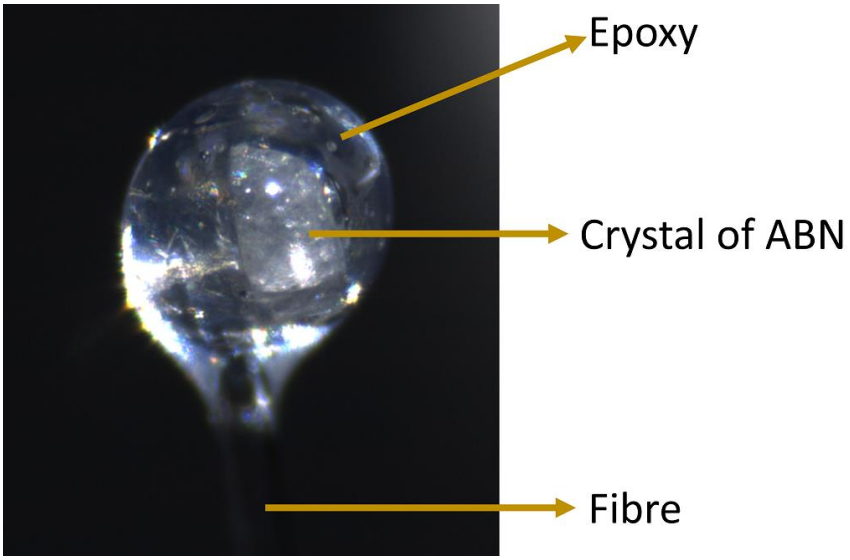

Fig. S7 A single crystal of ABN glued to a glass fibre and covered with epoxy.

Table S1 Crystallographic details for ABN.

Identification code	**ABN_300K**	**ABN_280K**	**ABN_260K**	**ABN_240K**	**ABN_220K**	**ABN_200K**
Empirical formula	$C_7H_6N_2$	$C_7H_6N_2$	$C_7H_6N_2$	$C_7H_6N_2$	$C_7H_6N_2$	$C_7H_6N_2$
Formula weight/g/mol	118.14	118.14	118.14	118.14	118.14	118.14
Temperature/K	300(2)	280(2)	260(2)	240(2)	220(2)	200(2)
Crystal system	Monoclinic	Monoclinic	Monoclinic	Monoclinic	Monoclinic	Monoclinic
Space group	$P2_1/c$	$P2_1/c$	$P2_1/c$	$P2_1/c$	$P2_1/c$	$P2_1/c$
a/Å	7.3414(5)	7.3198(5)	7.3002(5)	7.2815(6)	7.2662(6)	7.2430(5)
b/Å	5.5181(4)	5.5097(3)	5.5022(3)	5.4951(4)	5.4906(4)	5.4842(4)
c/Å	16.1043(11)	16.0906(11)	16.0771(11)	16.0633(12)	16.0552(13)	16.0426(11)
α/°	90	90.00	90.00	90.00	90.00	90.00
β/°	102.118(2)	102.034(2)	101.968(2)	101.903(2)	101.835(3)	101.8840(10)
γ/°	90	90.00	90.00	90.00	90.00	90.00
Volume/Å^3	637.86(8)	634.67(7)	631.73 (7)	628.91(8)	626.92(8)	623.79(8)
Z	4	4	4	4	4	4
ρ_{calc}g/cm^3	1.230	1.236	1.242	1.248	1.252	1.258
μ/mm^{-1}	0.077	0.078	0.078	0.079	0.079	0.079
F(000)	248	248	248	248	248	248
Crystal size/mm^3	0.63 × 0.44 × 0.16	0.62 × 0.43 × 0.15	0.61 × 0.42 × 0.14	0.60 × 0.41 × 0.13	0.59 × 0.40× 0.12	0.58 × 0.39 × 0.11
Radiation	MoKα (λ = 0.71073)	MoKα (λ = 0.71073)	MoKα (λ = 0.71073)	MoKα (λ = 0.71073)	MoKα (λ = 0.71073)	MoKα (λ = 0.71073)
θ range for data collection/°	2.84 to 25.02	2.85 to 25.34	3.92 to 25.35	3.93 to 25.35	3.93 to 25.34	3.94 to 26.02
Index ranges	-8 ≤ h ≤ 8, -6 ≤ k ≤ 6, -19 ≤ l ≤ 19	-8 ≤ h ≤ 8, -6 ≤ k ≤ 6, -19 ≤ l ≤ 19	-8 ≤ h ≤ 8, -6 ≤ k ≤ 6, -19 ≤ l ≤ 19	-8 ≤ h ≤ 8, -6 ≤ k ≤ 6, -19 ≤ l ≤ 19	-8 ≤ h ≤ 8, -6 ≤ k ≤ 6, -19 ≤ l ≤ 19	-8 ≤ h ≤ 8, -6 ≤ k ≤ 6, -19 ≤ l ≤ 19
Reflections collected	9632	9938	9862	9587	9293	9860
Independent reflections	1119 [R_{int} = 0.0344]	1151 [R_{int} = 0.0337]	1146 [R_{int} = 0.0314]	1142 [R_{int} = 0.0279]	1138 [R_{int} = 0.0269]	1206 [R_{int} = 0.0263]
Data/restraints/parameters	1119/0/90	1151 /0/90	1146/0/90	1142/0/90	1138/0/90	1206/0/90
Goodness-of-fit on F^2	1.043	1.078	1.047	1.083	1.065	1.049
Final R indexes [I>=2σ (I)]	R_1 = 0.0407, wR_2 = 0.1013	R_1 = 0.0403, wR_2 = 0.1035	R_1 = 0.0388, wR_2 = 0.0981	R_1 = 0.0367, wR_2 = 0.0942	R_1 = 0.0350, wR_2 = 0.087	R_1 = 0.0357, wR_2 = 0.0898
Final R indexes [all data]	R_1 = 0.0522, wR_2 = 0.1096	R_1 = 0.0493, wR_2 = 0.1111	R_1 = 0.0475, wR_2 = 0.1053	R_1 = 0.0436, wR_2 = 0.1001	R_1 = 0.0410, wR_2 = 0.0919	R_1 = 0.0424, wR_2 = 0.0946
Largest diff. peak/hole / e Å^{-3}	0.094/-0.12	0.093/-0.118	0.105/-0.119	0.117/-0.122	0.12/-0.098	0.139/-0.137
CCDC Number	1816756	1816754	1816755	1816759	1816758	1816753

Table S1 continued

Identification code	**ABN_180K**	**ABN_160K**	**ABN_140K**	**ABN_120K**	**ABN_100K**	**ABN_300K_R**
Empirical formula	$C_7H_6N_2$	$C_7H_6N_2$	$C_7H_6N_2$	$C_7H_6N_2$	$C_7H_6N_2$	$C_7H_6N_2$
Formula weight	118.14	118.14	118.14	118.14	118.14	118.14
Temperature/K	180(2)	160(2)	140(2)	120(2)	100(2)	300(2)
Crystal system	Monoclinic	Monoclinic	Monoclinic	Monoclinic	Monoclinic	Monoclinic
Space group	$P2_1/c$	$P2_1/c$	$P2_1/c$	$P2_1/c$	$P2_1/c$	$P2_1/c$
a/Å	7.2228(5)	7.368(2)	7.3455(19)	7.3320(18)	7.3184(18)	7.3645(18)
b/Å	5.4765(4)	5.7105(17)	5.7043(15)	5.7057(14)	5.7059(15)	5.5357(14)
c/Å	16.0273(12)	15.915(5)	15.878(4)	15.859(4)	15.844(4)	16.147(4)
α/°	90.00	90.00	90.00	90.00	90.00	90.00
β/°	101.740(2)	113.088(7)	113.224(6)	113.341(6)	113.439(6)	102.119(6)
γ/°	90.00	90.00	90.00	90.00	90.00	90.00
Volume/Å^3	620.71(8)	616.0(3)	611.4(3)	609.1(3)	607.0(3)	643.60
Z	4	4	4	4	4	4
ρ_{calc} g/cm^3	1.264	1.274	1.283	1.288	1.293	1.219
μ/mm^{-1}	0.080	0.080	0.081	0.081	0.081	0.077
F (000)	248	248	248	248	248	248
Crystal size/mm^3	0.57 × 0.38 × 0.10	0.56 × 0.37 × 0.09	0.55 × 0.36 × 0.08	0.54 × 0.35 × 0.07	0.53 × 0.34 × 0.06	0.63 × 0.44 × 0.16
Radiation	MoKα (λ = 0.71073)	MoKα (λ = 0.71073)	MoKα (λ = 0.71073)	MoKα (λ = 0.71073)	MoKα (λ = 0.71073)	MoKα (λ = 0.71073)
θ range for data collection/°	2.88 to 25.34	2.78 to 26.17	3.02 to 26.11	3.03 to 26.11	3.03 to 25.02	2.83 to 26.36
Index ranges	-8 ≤ h ≤ 8, -6 ≤ k ≤ 6, -19 ≤ l ≤ 19	-9 ≤ h ≤ 9, -7 ≤ k ≤ 6, -19 ≤ l ≤ 19	-9 ≤ h ≤ 9, -7 ≤ k ≤ 6, -19 ≤ l ≤ 19	-9 ≤ h ≤ 9, -7 ≤ k ≤ 6, -19 ≤ l ≤19	-8 ≤ h ≤ 8, -6 ≤ k ≤ 6, -18 ≤ l ≤ 18	-9 ≤ h ≤ 9, -6 ≤ k ≤ 6, -20 ≤ l ≤ 20
Reflections collected	9721	6188	7099	7218	6483	6483
Independent reflections	1134 [R_{int} = 0.0283]	1208[R_{int} = 0.1831]	1197 [R_{int} = 0.0420]	1184 [R_{int} = 0.0407]	1056 [R_{int} = 0.0371]	1306 [R_{int} = 0.0420]
Data/restraints/parameters	1134/0/90	1208/0/90	1197/0/90	1184/0/90	1056/0/90	1306/0/90
Goodness-of-fit on F^2	1.067	1.080	1.081	1.102	1.092	1.070
Final R indexes [I>=2σ (I)]	R_1 = 0.0344, wR_2 = 0.0890	R_1 = 0.0713, wR_2 = 0.1707	R_1 = 0.0565, wR_2 = 0.1270	R_1 = 0.0560, wR_2 = 0.1277	R_1 = 0.0502, wR_2 = 0.1205	R_1 = 0.0622, wR_2 = 0.1360
Final R indexes [all data]	R_1 = 0.0392, wR_2 = 0.0929	R_1 = 0.1001, wR_2 = 0.1876	R_1 = 0.0786, wR_2 = 0.1377	R_1 = 0.0772, wR_2 = 0.1383	R_1 = 0.06769, wR_2 = 0.1294	R_1 = 0.1150, wR_2 = 0.1580
Largest diff. peak/hole / e Å^{-3}	0.131/-0.143	0.315/-0.244	0.201/-0.218	0.219/-0.218	0.200/-0.218	0.119/-0.151
CCDC Number	1816752	1816762	1816750	1816749	1816748	1816757

Table S2 Hydrogen bonding interaction in ABN from 100 K to 300 K

Temperature (K)	**100**	**120**	**140**	**160**	**180**	**200**	**220**	**240**	**260**	**280**	**300**	**300_R**
N1···N2 (Å)	3.1385 (6)	3.1417 (5)	3.1452 (6)	3.1515 (8)	3.2052 (2)	3.2116 (1)	3.2154 (2)	3.2193 (2)	3.2235 (1)	3.2284 (1)	3.2339 (1)	3.2474 (5)
N1-H1B···N2 (°)	159.204 (13)	159.543 (10)	159.471 (11)	161.053 (12)	156.906 (3)	156.929 (3)	156.925 (3)	156.609 (3)	157.406 (2)	157.002 (2)	157.132 (3)	156.718 (9)
C3···N2 (Å)	3.4713 (6)	3.4742 (6)	3.4789 (7)	3.4864 (8)	3.4592 (2)	3.4690 (2)	3.4779 (2)	3.4845 (2)	3.4940 (2)	3.5031 (2)	3.5130 (2)	3.5230 (6)
C3-H3···N2 (°)	144.545 (9)	144.764 (8)	144.906 (9)	145.406 (10)	156.524 (2)	156.643 (2)	156..903 (2)	157.118 (2)	157.395 (2)	157.502 (2)	157.717 (2)	157.992 (8)
C3···$i_{C\equiv N}$ (Å)	3.6209 (7)	3.6249 (6)	3.6300 (7)	3.6431 (8)	3.7806 (2)	3.7886 (2)	3.7968 (2)	3.8022 (2)	3.8098 (2)	3.8185 (2)	3.8276 (2)	3.8399 (6)
N1···i_{Ar} (Å)	3.4049 (7)	3.4113 (7)	3.4213 (7)	3.4318 (8)	3.4383 (2)	3.4486 (2)	3.4615 (2)	3.4703 (2)	3.4810 (2)	3.4935 (2)	3.5044 (2)	3.5158 (7)

Non-standard unit cell setting

In the temperature range 300 to 180 K, the monoclinic space group setting for ABN could be either $P2_1/c$ with a β angle of ca 102°, or $P2_1/n$ with a β angle of ca 104°. The former is the standard setting because its angle is closer to 90°. After the phase transition, the monoclinic crystal system is retained, and the space group settings could be either $P2_1/c$ with a β angle of ca 113°, or $P2_1/n$ with a β angle of ca 94°. In this case, the latter is the standard setting.

However, accepting the standard setting for the low temperature phase does not facilitate direct comparison of the structures before and after the transition. We therefore enforced the $P2_1/c$ setting for the low temperature phase because this choice facilitates our understanding of the transition that accompanies the thermosalient event.

Thermal expansion

This study investigates two enantiotropic polymorphs of ABN in the monoclinic crystal system. Since the three crystallographic axes are not orthogonal to one another the principal axis strain calculator (PASCal program)[7] was used to determine the linear thermal expansion coefficients along all the three principal axes, as well as the volumetric thermal expansion coefficient.

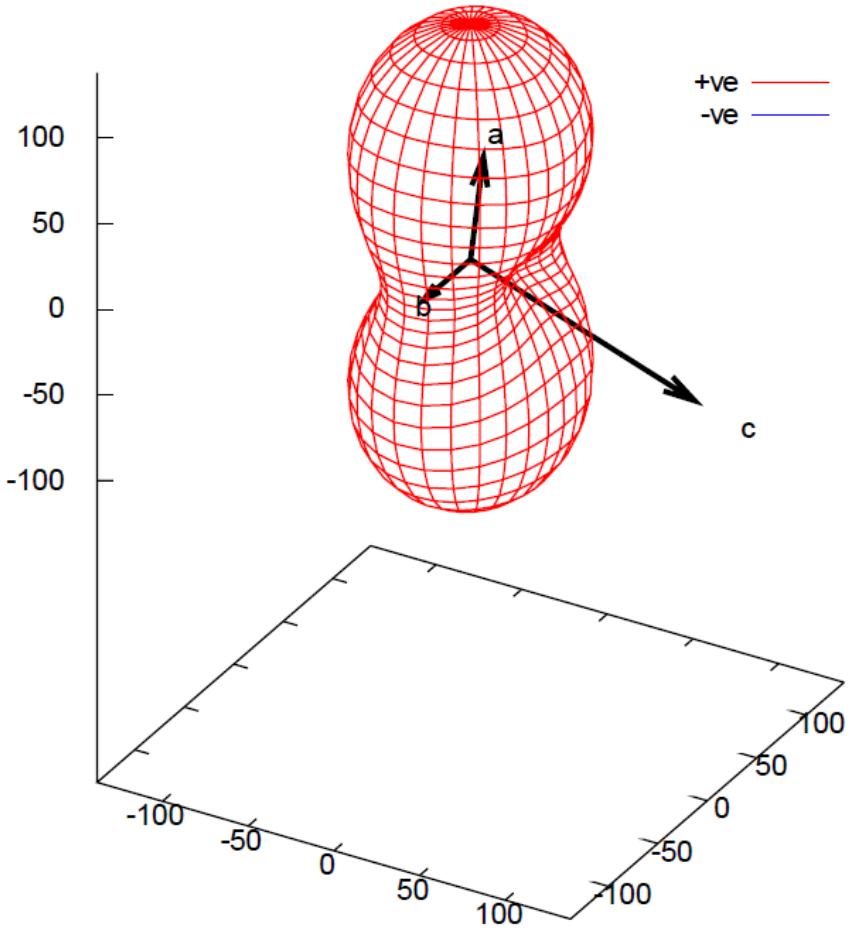

Fig. S8 Expansivity indicatrix (300 to 180 K).

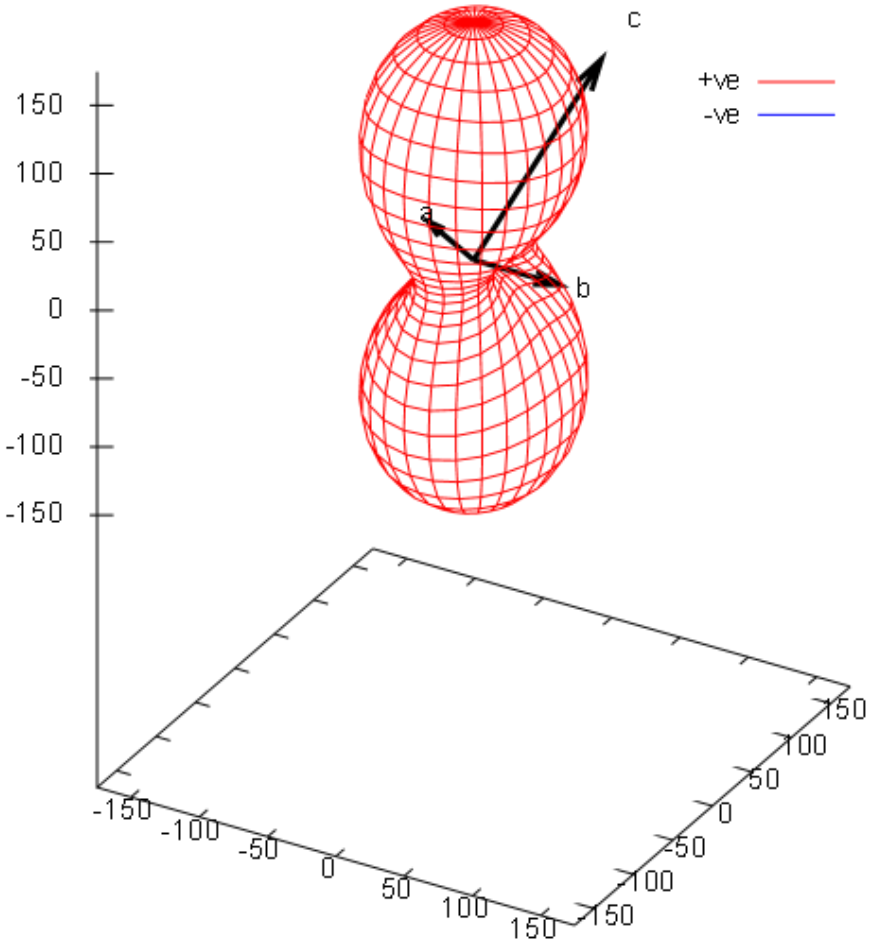

Fig. S9 Expansivity indicatrix (160 to 100 K).

Table S3 Thermal expansion coefficients α_{X1}, α_{X2}, and α_{X3} and volumetric thermal expansion coefficients (α_V), with the percentage changes in length and volume.

Purely organic crystal	Temp(K)	$\alpha_{X1}(MK^{-1})$	$\alpha_{X2}(MK^{-1})$	$\alpha_{X3}(MK^{-1})$	$\alpha_{v}(MK^{-1})$	% change in length along X1	% change in length along X2	% change in length along X3	% change in volume
ABN	100 – 160	10.87	54.76	174.69	250.04	0.08	0.34	1.06	1.5
	180 – 300	24.76	61.34	138.19	225.07	0.31	0.76	1.69	3.0

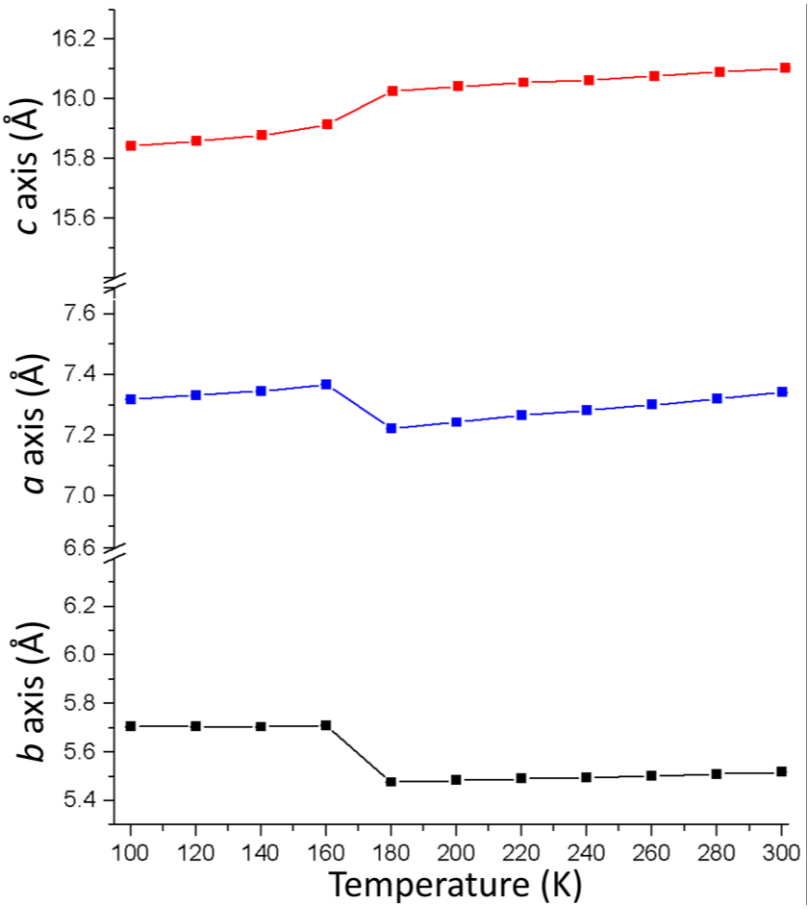

Fig. S10 Variation in the unit cell dimension showing the phase transition between 160 and 180 K.

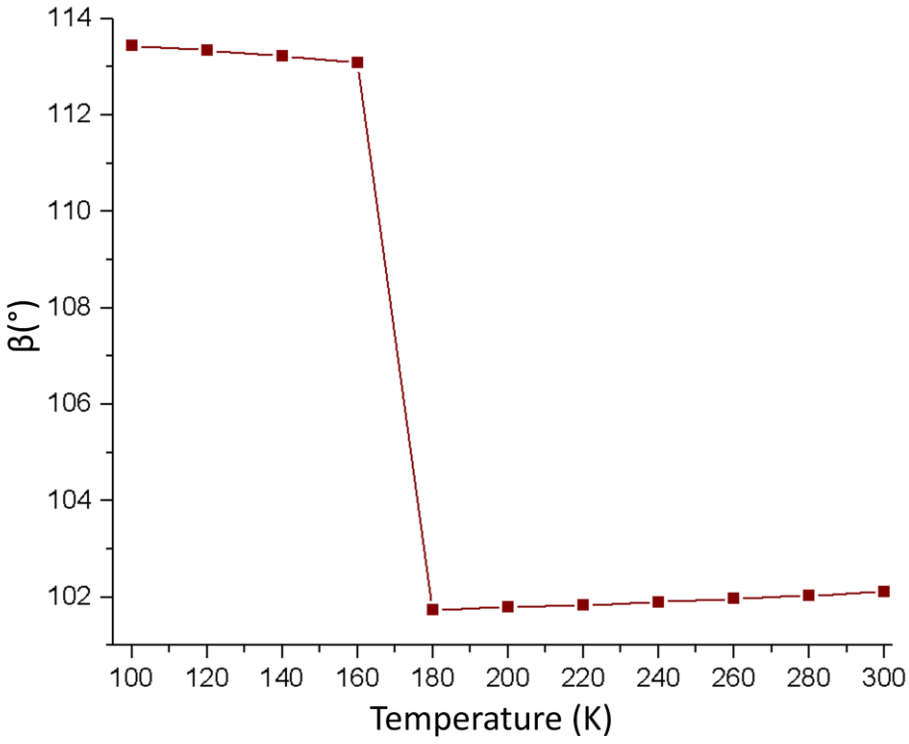

Fig. S11 Variation in the β angle showing the phase transition between 160 and 180 K.

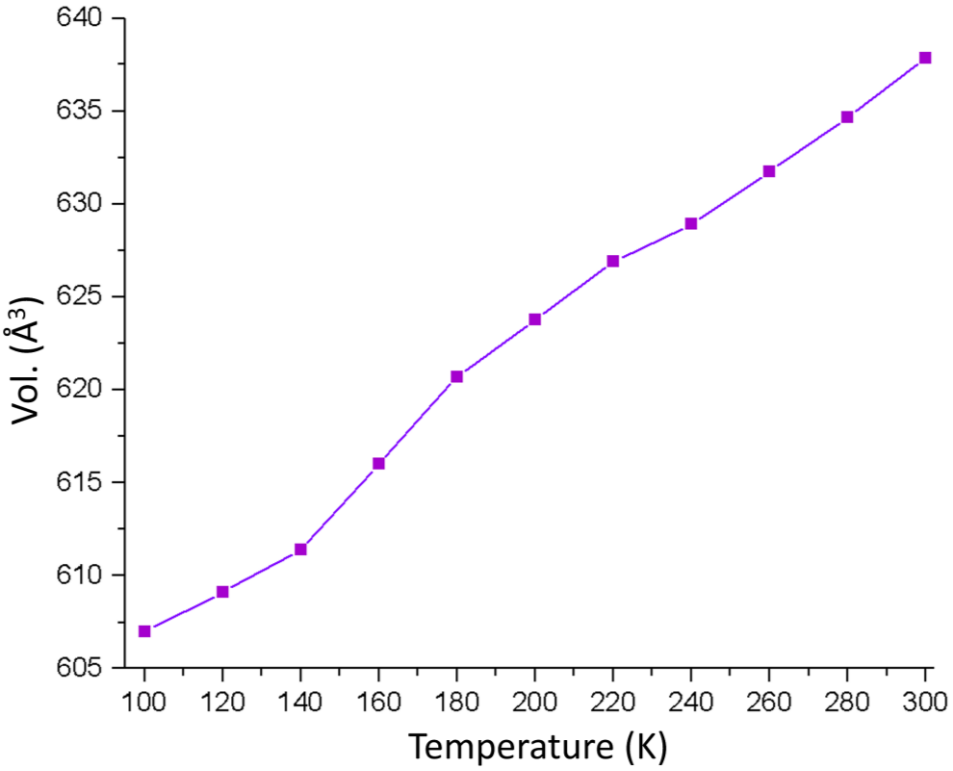

Fig. S12 Variation in unit cell volume of ABN with temperature.

Hirshfeld surface analysis

The program CrystalExplorer[8] (Version 3.1) was used to generate Hirshfeld surfaces (d_{norm}) to indicate the intermolecular interactions for a molecule of ABN in the structures determined at 180 and 160 K. Animations of the surfaces and the corresponding interacting molecules are shown in Videos S3 and S4, respectively.

Overlay of bilayers

In order to assess the similarity of the bilayers in the structures at 180 and 160 K, subsets of the two structures were overlaid using Materials Studio.[9] The RMS difference for a 4 × 2 subset of molecules within the bilayers (represented with thicker bonds in Fig. S12) is 0.176 Å.

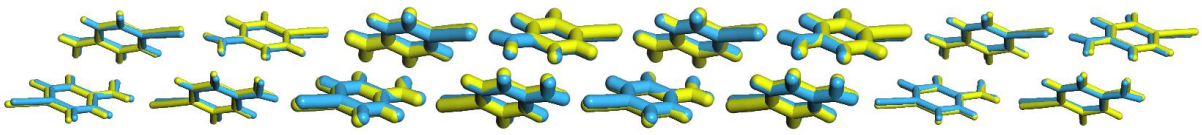

Fig. S13 Overlay of the bilayers showing negligible change in the internal arrangement before and after phase change (Yellow, 180 K; Blue, 160 K).

Theoretical investigation

Hydrogen-atom positions were optimised in *P*1 using the DMol[3] code as implemented in Materials Studio with non-hydrogen atoms constrained to their crystallographic positions.[10] The density functional theory (DFT) generalised gradient approximation of Perdew-Burke-Ernzerhof (PBE)[11] in combination with Grimme's DFT-D dispersion correction[12] was employed. The double numeric plus polarization basis set (DNP, version 4.4) was employed with an orbital cut-off of 3.7 Å. Integration in the reciprocal lattice was performed using a Monkhorst-Pack grid[13] with a k-point separation of 0.07 $Å^{-1}$ and self-consistent field convergence was set to 1.0×10^{-6} au. A hexadecapole multipolar expansion[14] and 20% admixture of the charge density was applied in conjunction with a DIIS (direct inversion in an iterative subspace) size of 6 to speed up convergence.[15] Geometry optimization convergence tolerances on energy, maximum force and maximum displacement were set to 1.0×10^{-5} au, 0.002 Ha $Å^{-1}$ and 0.005 Å, respectively.

Lattice energies were calculated according to the following formula:

$$E_{\text{lattice}} = E_{\text{crystal}} - Z \times E_{\text{reference}}$$

where Z represents the number of symmetry operators present in the space group – four for $P2_1/c$. Although trends should be maintained, the choice of reference system affects the absolute values of lattice energies. Removing three ABN molecules from the *P*1 geometry-optimised unit cell yielded periodic reference **{ABN}** while subsequent deletion of the unit cell yielded molecular reference **(ABN)**. Single point energy evaluations were carried out at the same level of theory as hydrogen-atom geometry optimisations to afford the results given in Figure S14.

A comparison of $E_{\text{lattice}}^{(\mathbf{ABN})}$ (●) and $E_{\text{lattice}}^{\{\mathbf{ABN}\}}$ (○) shows a similar downward trend upon cooling ABN before and after the phase change; however, an opposite change is observed during the phase change between the 180 and 160 K structures. The periodic aromatic-π interaction along the *b* axis, denoted as $\{\pi_{\text{Ar}}\cdots\pi_{\text{Ar}}\}_{\text{b}}$, is calculated as the difference between the single point energy of **{ABN}** and the single point energy of the system comprising one ABN molecule within a unit cell of which the *b*-axis length is doubled, designated **{ABN *b* × 2}**:

$$E_{\text{int}}^{\{\boldsymbol{\pi}_{\mathbf{Ar}}\cdots\boldsymbol{\pi}_{\mathbf{Ar}}\}} = E_{\{\mathbf{ABN}\}} - E_{\{\mathbf{ABN}\ \boldsymbol{b} \times \mathbf{2}\}}$$

It is interesting to note that the $\{i_{Ar}\cdots i_{Ar}\}_b$ interaction (○) becomes more favourable notwithstanding a lengthening of the *b* axis upon cooling. Taking this principal intermolecular interaction into account, $E_{\text{lattice}}^{\{\mathbf{ABN}\ \boldsymbol{b}\times\mathbf{2}\}}$ (**Δ**) is found to closely trace $E_{\text{lattice}}^{(\mathbf{ABN})}$ (●).

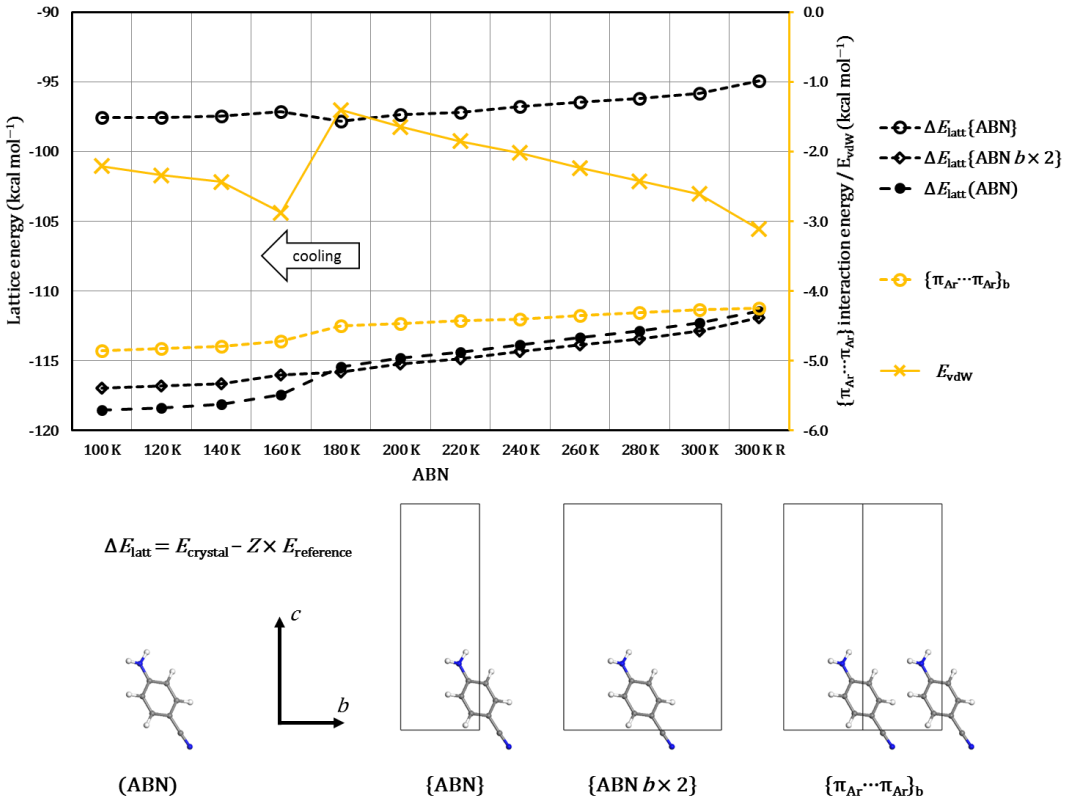

Fig. S14 Comparison of lattice energies calculated using different reference systems. A single ABN in a unit cell with the *b*-axis length doubled, **{ABN *b* × 2}**, yields the same lattice energy as that calculated using an isolated ABN molecule, **(ABN)**. Also shown is the change in the strength of the $\{\pi_{Ar}\cdots\pi_{Ar}\}_b$ intermolecular (○) and the non-bond van der Waals (×) interactions.

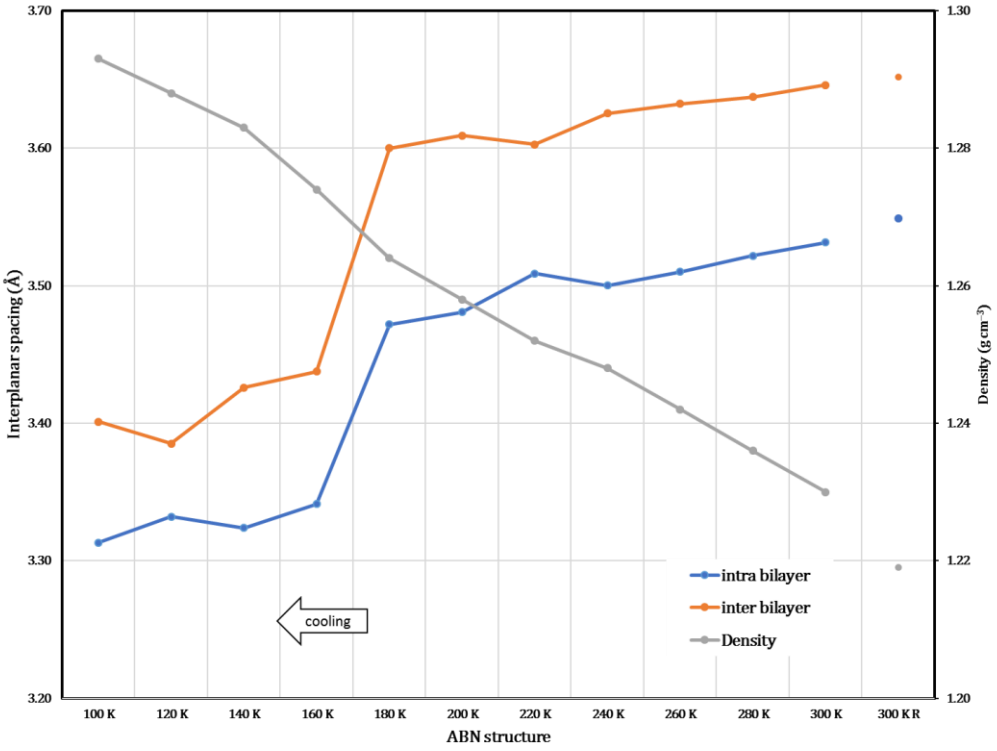

Fig. S15 Comparison of inter- and intra-bilayer spacing (calculated as planes through the aromatic ring centroids) as a function of temperature. Also shown is the trend in calculated density.

The $\{\pi_{Ar}\cdots\pi_{Ar}\}_b$ intermolecular interaction becomes more favourable after the phase due to a reduction of the spacing between mean planes through the ABN molecules, $P_{x,y,z}\cdots P_{x,y+1,z}$ (Table S4).

Table S4 Interplanar and centroid$_{Ar}\cdots$centroid$_{Ar}$ distances involved in principal $\pi\cdots\pi$ intermolecular interactions (P = aromatic mean plane, i_{Ar} = ring centroid, distances in Å).

Temp/K	100	120	140	160	180	200	220	240	260	280	300	300_R
$P_{x,y,z}\cdots P_{x,y+1,z}$	2.49	2.50	2.52	2.53	2.78	2.79	2.80	2.80	2.81	2.82	2.83	2.84
$i_{Ar}\cdots i_{Ar}$	5.71	5.71	5.70	5.71	5.48	5.48	5.49	5.50	5.50	5.51	5.52	5.54
$P_{x,y,z}\cdots P_{1-x,1-y,1-z}$	3.47	3.48	3.49	3.50	3.60	3.61	3.62	3.62	3.63	3.63	3.64	3.65
$i_{Ar}\cdots i_{Ar}$	4.12	4.13	4.15	4.17	5.18	5.19	5.19	5.19	5.19	5.19	5.19	5.20

Molecular Mechanics single point energy evaluations of the hydrogen-atom optimised structures were carried out using the Forcite code of Materials Studio employing the COMPASS force field[16] with force-field assigned charges and Ewald summation.[17]

Table S5 Summary of contributions to the Molecular Mechanics total energy.

Temp (K) / **Energy (kcal mol^{-1})**	**100K**	**120K**	**140K**	**160K**	**180K**	**200K**	**220K**	**240K**	**260K**	**280K**	**300K**	**300K_R**
Total	231.0024	230.4255	229.8857	228.075	222.6462	222.7126	222.3242	222.6924	222.4117	222.1977	222.2181	220.8533
Valence	21.827	21.685	21.648	20.907	22.782	23.217	23.254	23.703	23.739	23.833	24.043	23.448
Valence (diagonal terms)	15.399	15.32	15.316	15.254	15.853	15.816	15.825	15.732	15.648	15.618	15.564	15.481
Bond	1.617	1.614	1.608	1.598	1.333	1.324	1.321	1.307	1.298	1.293	1.289	1.304
Angle	9.33	9.31	9.399	9.301	12.421	12.332	12.48	12.215	12.142	12.108	12.057	11.579
Torsion	3.133	3.085	3.027	3.056	1.519	1.559	1.466	1.59	1.578	1.588	1.584	1.844
Inversion	1.319	1.311	1.282	1.299	0.581	0.601	0.559	0.62	0.629	0.629	0.634	0.754
Valence (cross terms)	6.428	6.365	6.332	5.653	6.929	7.401	7.429	7.971	8.091	8.215	8.479	7.967
Stretch-Stretch	-0.011	-0.013	-0.014	-0.01	-0.01	-0.009	-0.01	-0.009	-0.009	-0.01	-0.009	-0.006
Stretch-Bend-Stretch	-0.678	-0.741	-0.856	-0.656	-0.957	-0.891	-1.02	-0.955	-0.97	-1.012	-1.005	-0.658
Stretch-Torsion-Stretch	4.14	4.357	4.606	3.745	5.257	5.549	5.915	6.301	6.572	6.851	7.191	5.823
Separated-Stretch-Stretch	-0.034	-0.036	-0.038	-0.03	-0.042	-0.045	-0.048	-0.051	-0.053	-0.055	-0.057	-0.047
Torsion-Stretch	-1.853	-1.955	-2.094	-1.952	-2.082	-1.993	-2.134	-2.058	-2.104	-2.156	-2.163	-1.787
Bend-Bend	-1.594	-1.604	-1.632	-1.612	-2.28	-2.26	-2.308	-2.243	-2.235	-2.237	-2.233	-2.109
Torsion-Bend-Bend	0.042	0.036	0.036	0.032	0.052	0.05	0.051	0.052	0.051	0.05	0.048	0.052
Bend-Torsion-Bend	6.416	6.321	6.324	6.137	6.992	7	6.984	6.933	6.839	6.782	6.707	6.699
Non-bond	209.176	208.74	208.238	207.168	199.864	199.496	199.07	198.99	198.673	198.365	198.176	197.406
Van der Waals	-2.209	-2.338	-2.436	-2.875	-1.403	-1.646	-1.853	-2.02	-2.235	-2.422	-2.607	-3.11
Electrostatic	211.385	211.078	210.673	210.043	201.268	201.141	200.923	201.01	200.908	200.787	200.782	200.516

Trends in the strengths of principal directional intermolecular interaction energies were subsequently investigated at the DFT level of theory. Each ABN molecule acts as a donor and acceptor for three principal intermolecular interactions of type N−H···N≡C, N−H···π_{Ar} and C−H···$\pi_{C\equiv N}$ as shown in Figure S16. Two offset aromatic-π interactions are present: $\{\pi_{Ar}\cdots\pi_{Ar}\}_b$ along the *b* axis and $\{\pi_{Ar}\cdots\pi_{Ar}\}$ between bilayers. Table S4 shows the reduction in the $P_{x,y,z}\cdots P_{x,y+1,z}$ and $P_{x,y,z}\cdots P_{1-x,1-y,1-z}$ mean plane separation.

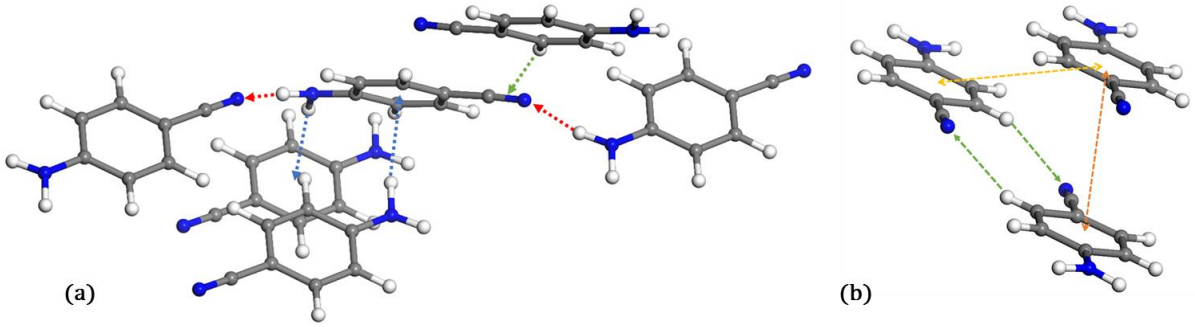

Fig. S16 (a) The six-principal directional intermolecular interactions each ABN molecule is involved in: N−H···N≡C (red, along [001]), N−H···π_{Ar} (blue) and C−H···$\pi_{C\equiv N}$ (green, to the same molecule). (b) Two offset $\{\pi_{Ar}\cdots\pi_{Ar}\}_b$ (yellow, along [010]) and $\{\pi_{Ar}\cdots\pi_{Ar}\}$ (orange) interactions.

Molecular and periodic interaction energies used **(ABN)** and **{ABN}** as reference system, respectively. Figure S17 depicts the model structures used in the calculation of periodic E_{int} values, while *bimolecular* models were employed in determining molecular E_{int} values. Note that **{ABN}** already encompasses the $\{\pi_{\mathrm{Ar}}\cdots\pi_{\mathrm{Ar}}\}_{\mathrm{b}}$ interaction present in the periodic model structures. Figures S18 and S19 summarise all E_{int} values.

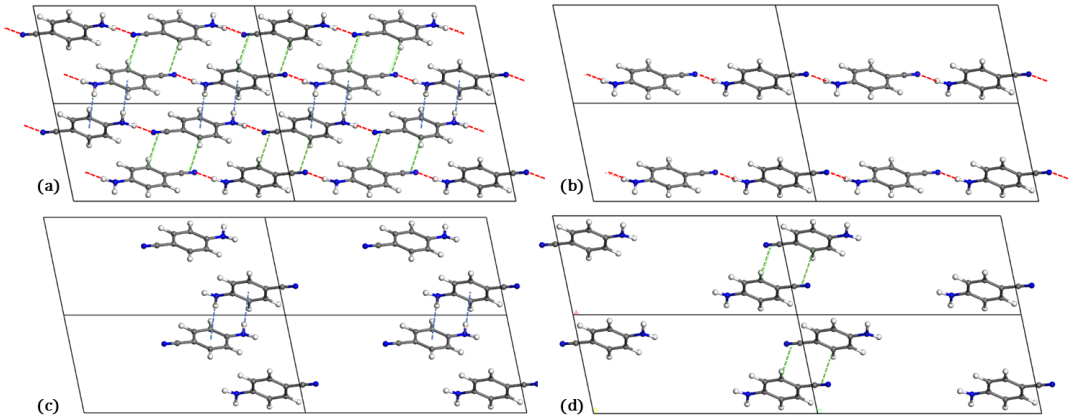

Fig. S17 (a) Packing diagram of the ABN collected at 180 K and model structures used for the calculation of the strength of the (b) intralayer N–H···N≡C (red), (c) intrabilayer N–H···π_{Ar} (blue) and (d) interbilayer C–H···$\pi_{\mathrm{C\equiv N}}$ (green) periodic intermolecular interactions. View: [010]

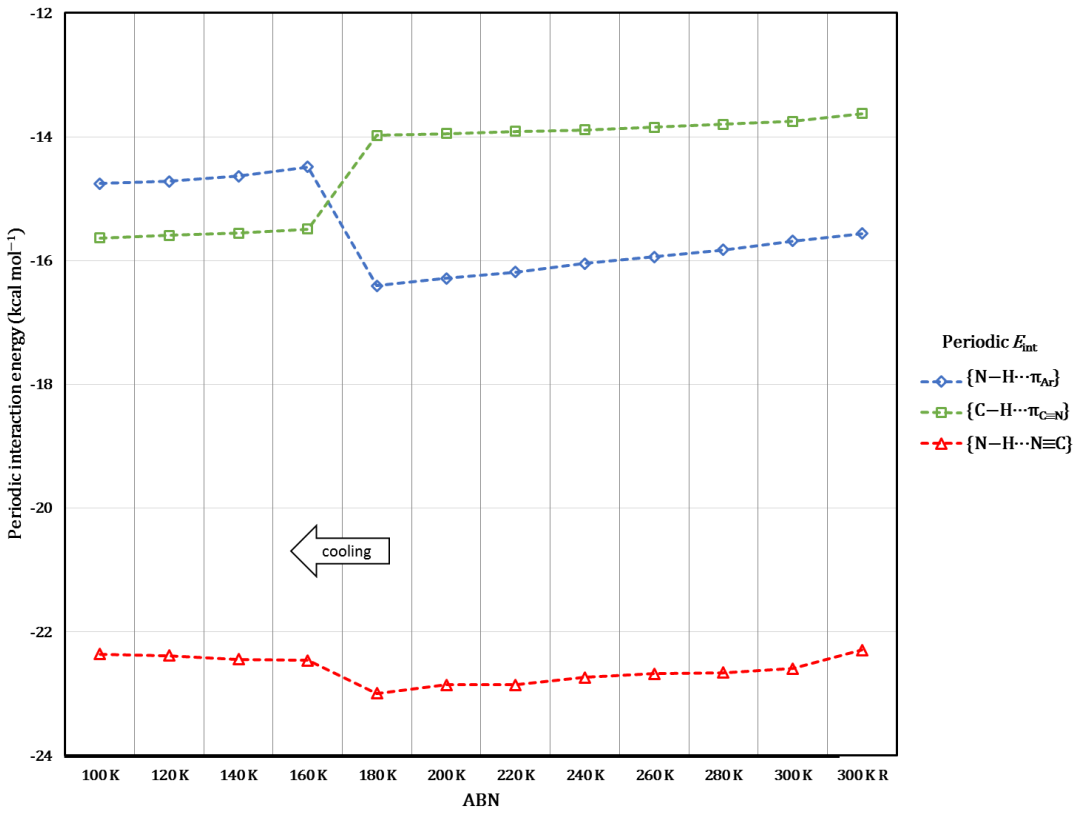

Fig. S18 Plot of periodic interaction energies of principal intermolecular interactions.

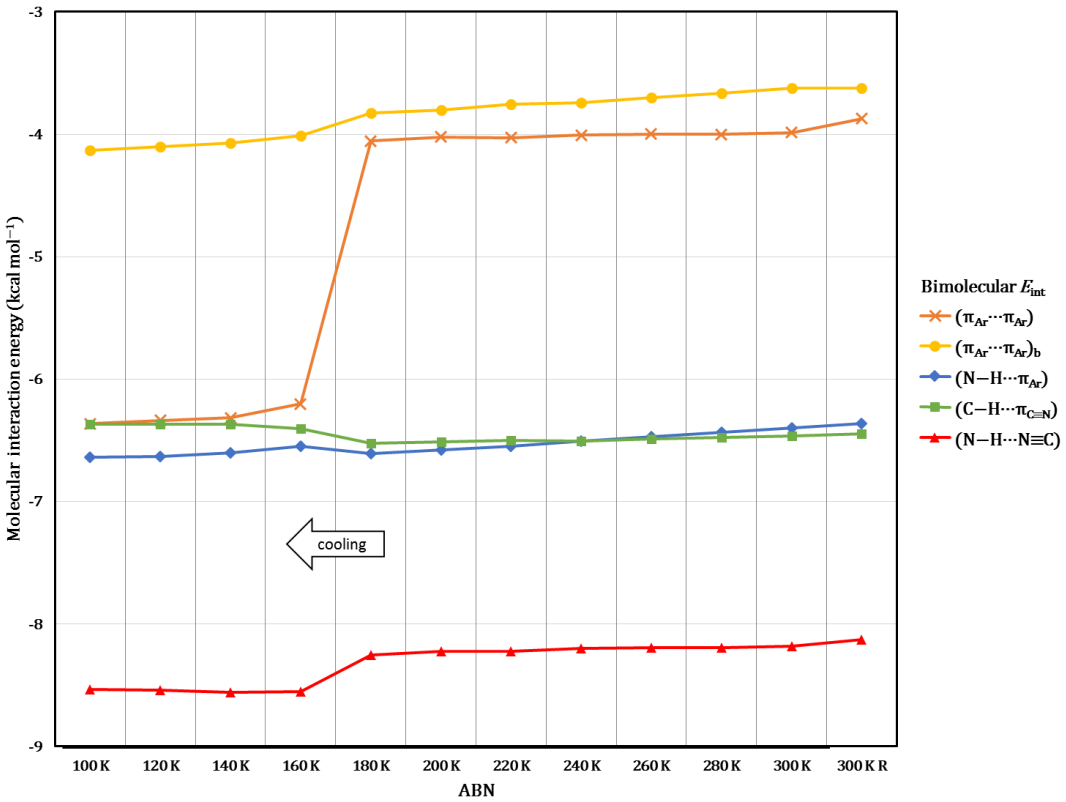

Fig. S19 Plot of molecular interaction energies of principal intermolecular interactions.

The molecular $(\pi_{Ar}\cdots\pi_{Ar})_b$ interaction (●) follows a similar trend as the periodic $\{\pi_{Ar}\cdots\pi_{Ar}\}_b$ (○, *cf.* Fig. S14). The strengthening of the periodic C–H$\cdots\pi_{C\equiv N}$ interaction is not mirrored in the molecular case due to the admixture of the $\{\pi_{Ar}\cdots\pi_{Ar}\}$ interaction. Thus, $E_{int}^{\{C-H\cdots\pi_{C\equiv N}\}}|\square \approx E_{int}^{(C-H\cdots\pi_{C\equiv N})}|\blacksquare + E_{int}^{(\pi_{Ar}\cdots\pi_{Ar})}|\times$. Whereas the molecular $E_{int}^{(N-H\cdots N\equiv C)}|\blacktriangle$ becomes more favourable during the 180 to 160 K thermosalient phase change, the periodic $E_{int}^{\{N-H\cdots N\equiv C\}}|\Delta$ shows a destabilisation. *Trimolecular* models were used to approximate crystal field polarization effects to yield the molecular interaction energies shown in Figure S20. The deconvoluted E_{int} are all more favourable than their bimolecular counterpart and show a more pronounced change over the phase change. The deconvoluted $E_{int}^{(N-H\cdots N\equiv C)}|\blacktriangle$ (Fig. S20(b)) now follows the same trend as $E_{int}^{\{N-H\cdots N\equiv C\}}|\Delta$ (*cf.* Fig. S18), highlighting the cooperative effect of intermolecular interactions in crystal structures.

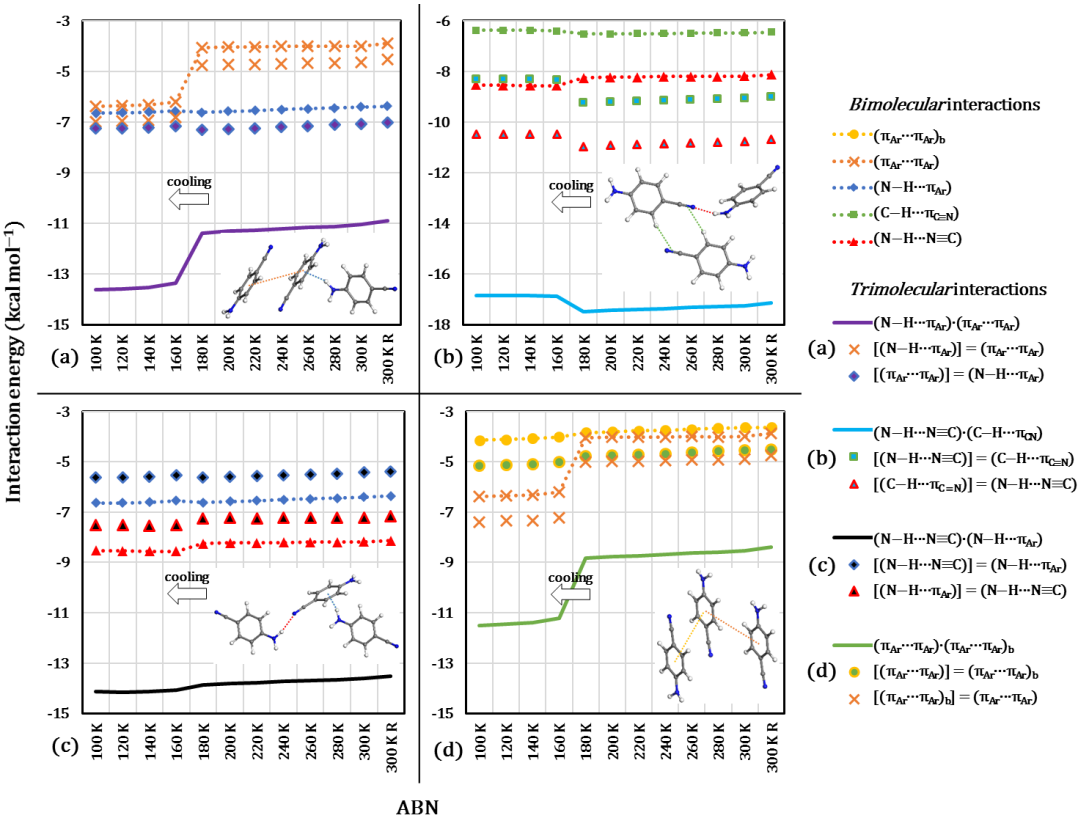

Fig. S20 Deconvoluted interaction energies calculated from *trimolecular* representations. The corresponding bimolecular interaction energies are plotted for each combination.

The 2.2 kcal mol^{-1} strengthening of the interlayer ($\pi_{Ar}\cdots\pi_{Ar}$) interaction (×, Fig. S19) can be considered a major driving force for the 180 to 160 K phase change. A similar strengthening of the intralayer N–H$\cdots\pi_{Ar}$ interaction (◊, Fig. S18) might account for the reversal of the phase change. However, a balance between directional intermolecular interactions and profuse non-directional van der Waals forces determines the physical conditions that bring about the thermosalient phase change.

5.3. References

1. *TOPAS, V4.2, General Profile and Structure Analysis Software for Powder Diffraction Data Users' Manual*; Bruker, AXS: Karlsruhe, 2009.

2. SAINT Data Reduction Software, Version 2017.3-RC2; Bruker AXS 2005-2017.

3. SADABS, Version 2.05; Bruker AXS Inc.: Madison, WI, 2002.

4. R. H. Blessing, *An Empirical Correction for Absorption Anisotropy, Acta Crystallogr., Sect. A: Found. Crystallogr.*, 1995, **51**, 33.

5. G. M. Sheldrick, *A Short History of SHELX. Acta Crystallogr., Sect. A: Found. Crystallogr.*, 2008, **64**, 112.

6. L. Barbour, X-Seed − *A Software Tool for Supramolecular Crystallography. J. Supramol. Chem.*, 2001, **1**, 189.

7. J. Cliffe and A. L. Goodwin, *J. Appl. Crystallogr.*, 2012, **45**, 1321.

8. M.A. Spackman and D. Jayatilaka, *CrystEngComm*, 2009, **11**, 19.

9. *Dassault Systèmes BIOVIA Materials Studio*, Release 18, San Diego: Dassault Systèmes, 2017.

10. B. Delley, *J. Chem. Phys.*, 2000, **113**, 7756.

11. J. P. Perdew, K. Burke and M. Ernzerhof, *Phys. Rev. Lett.*, 1996, **77**, 3865.

12. S. Grimme, *J. Comput. Chem.*, 2006, **27**, 1787.

13. H. J. Monkhorst and J. D. Pack, *Phys. Rev. B*, 1976, **13**, 5188.

14. B. Delley, *J. Chem. Phys.*, 1990, **92**, 508

15. P. Pulay, *Chem. Phys. Lett.*, 1980, **73**, 393

16. H. Sun, Z. Jin, C. Yang, R. L. C. Akkermans, S. H. Robertson, N. A. Spenley, S. Miller and S. M. Todd, *J. Mol. Model.*, 2016, **22**, 47.

17. M. P. Tosi, *Solid State Physics*, 1964, **16**, 107.

Chapter 6: Concluding remarks

We have reported in detail the thermal responsiveness of an organic crystal (ABN) and a novel organic cocrystal (ABN·2DMABN) as well as the mechanical behaviour of a rigid small organic molecule (4-BBN) for the first time.

Investigating the structure–property relationships of a material is an important fundamental aspect of supramolecular chemistry that has assisted in explaining in detail the correlation between the crystal structure (intermolecular interactions and packing) and the properties displayed by such crystals. Most organic materials that have been reported to possess exotic properties are often discovered by accident. However, through thorough investigation, efforts have been made to explain the structure-property relationships by examining the crystal structure and eventually proposing a mechanism based on the type, nature and strength of the intermolecular interactions as well as the crystal packing within the system. Consequently, the design of materials with specific properties has become viable.

Very few examples of such materials have been designed to date owing to the diverse nature of intermolecular interactions which make it difficult to establish universal and simple relationships and conclusions that would include all dynamic crystals. For these reasons, serendipity remains crucial in the discovery of these materials. This study describes our serendipitous discovery of two purely organic materials that display some visually impressive and exotic properties such as thermosalient effects, thermal expansion, and plastic bending behaviour. Potential materials were identified while exploring the thermal and mechanical history of some selected solid-state structures in the Cambridge Structural Database (CSD). We have also successfully designed a novel organic cocrystal that shows a unique thermal property.

A novel organic cocrystal (ABN·2DMABN) has been prepared by co-dissolving 4-aminobenzonitrile and 4-(dimethylamino)benzonitrile in a 1:2 molar ratio in acetone, and allowing slow evaporation over a few days. A thermal expansion study of the cocrystal was carried out over the temperature range 100–300 K at 20 K intervals. During the study it was observed that the material undergoes positive linear thermal expansion (PTE). That is, its unit cell parameters increase along all the three crystallographic axes with an increase in temperature without any evidence of a phase transition. Detailed structural analysis indicates that the thermal expansion is exclusively due to changes (lengthening) in the intermolecular

interaction distances, such as N–H···N, C–H···π and π···π interactions that are present along the principal axes *X*1, *X*2 and *X*3, respectively. Since the crystal system is monoclinic ($P2_1/n$), all the crystallographic axes need to be orthogonalised and the PASCal program was used to calculate the thermal expansion coefficients along the principal axes *X*1, *X*2 and *X*3. We observed that the axis that runs parallel to the strongest intermolecular interactions shows the lowest thermal expansion coefficient, whereas the axis parallel to the direction where the weakest interactions lie shows the highest thermal expansion coefficient. These observations are consistent with those reported in the literature. To the best of our knowledge, the associated volumetric thermal expansion coefficient of 222 MK^{-1} recorded for this material is the largest ever reported for an organic cocrystal over such a wide temperature range. This could be attributed to the fact that it shows significant linear PTE along all its three principal axes. Further characterisation using other techniques such as differential scanning calorimetry (DSC), hot-stage microscopy and X-ray powder diffraction confirms that the crystal does not undergo a phase transition over the temperature range of our investigation. Our findings imply that understanding the intermolecular interactions between molecules using cocrystallisation could be helpful in the design of new solid materials with the desired thermal expansion properties.

As we continued to explore the CSD, we encountered another group of organic 4-substitued benzonitrile molecules i.e. 4-halobenzonitriles. The search revealed that the crystal structures of 4-fluoro-, 4-chloro-, 4-bromo and 4-iodobenzonitrile as well as the mechanical bending behaviour of 4-fluoro- and 4-chlorobenzonitrile, have been reported. To our surprise no study detailing the mechanical bending of the 4-bromobenzonitrile (4-BBN) is reported to date. Since this material is structurally related to our previously studied 4-substituted benzonitrile (ABN and DMABN), we carried out a detailed investigation on its mechanical and physical properties. We crystallised 4-BBN by sublimation at 323 K for 3 h under dynamic vacuum (0.02 mbar) to obtain long, rectangular and colourless crystals. One of the important findings of this study is that crystals suitable for single-crystal X-ray diffraction (SCXRD) analysis can only be obtained by subliming the compound using the aforementioned conditions of temperature, pressure and duration. The crystals of 4-BBN obtained show plastic bending when mechanical stress is applied perpendicular to two of its crystal faces. Unlike the crystals of 4-fluorobenzonitrile and 4-chlorobenzonitrile, 4-BBN crystals display a rare bending phenomenon on two bendable crystal faces (010) and (101) that are orthogonal to each other, thus resulting in twisting and coiling which leads to the formation of helical crystals. This type

of bending behaviour is very unusual for a crystal of such a rigid small molecule. Indeed, there are only two examples in the literature (both reported by Saha *et al.*)[1,2] of crystals that exhibit two-dimensional bending (i.e. helical twisting), and both of these examples involve crystals of conformationally flexible molecules. Even though the crystal bends along two perpendicular planes, we also establish the crystallographic axis along which the bending occurs with respect to each bending face as well as that for the helical bending. Structural analysis of the crystal indicates the presence of anisotropic intermolecular interactions in the crystal packing. We discovered that C≡N···Br halogen bonding and π···π interactions are arranged perpendicular to each other on both bendable faces of the crystal that are also orthogonal to each other. The arrangement of these interactions can be said to be anisotropic since the strengths of the interactions differ, thus allowing for 2D bending. Since the crystal bends on its two perpendicular faces, this leads to the formation of helical/twisted crystals when hand twisted and, as a result, physical properties such as the melting point of the material also change.

We have also reported unusual and previously overlooked thermal behaviour of ABN. The single-crystals of ABN were obtained by sublimation at 333 K for several days under dynamic vacuum. Calorimetric and microscopic analysis of ABN crystals show that the material exhibits reversible thermosalience upon cooling from 300 to 100 K and subsequent heating to 300 K. In an attempt to explain the structural nature of this effect, variable-temperature single-crystal X-ray diffraction from 300 to 100 K at 20 K intervals was carried out on a single crystal of ABN. The single crystal was glued to the tip of a glass fibre and then covered with thin layer of epoxy to prevent it from jumping off the mount during data collection. The structural and theoretical investigations reveal that this event could be attributed to a lateral shift between the bilayers, which is governed by the interplay of the directional and non-directional interactions in the crystal packing. We observe the presence of several weak intermolecular interactions (directional and non-directional) both within and between the bilayers and this is confirmed with the aid of Hirshfeld surface analysis (using CrystalExplorer software) and theoretical energy calculations. As the molecules approach one another with decreasing temperature, the directional interactions become more favourable as evidenced by energy calculations, but at the expense of the van der Waal interactions. The steric repulsion can be understood as a topological mismatch that is enforced by the directional interactions. The built-up strain is released in a sudden transverse shearing motion of adjacent bilayers relative to one another, causing a rapid structural transformation that provides the energetic propulsion of the crystal. This study has further supported the assertion that the presence of

weak intermolecular interactions in crystal packing is a prerequisite for thermosalience. Improved understanding and control of these interactions could help in the design of materials that display this exotic property through the choice of appropriate functionality.

In conclusion, we have identified three different small organic molecules with similar structural architectures (4-substituted benzonitriles). We have successfully carried out a detailed and comprehensive structural investigation in order to explain and understand the structure-property relationships. These materials have exhibited interesting thermal and mechanical properties that have not been discovered even though the compounds have previously been reported in the literature. We can therefore infer that the fact that a material has been reported does not necessarily imply that its properties have been exhausted. It simply means a very detailed study/investigation with the aid of complementary techniques should be employed in order to discover these interesting but hidden properties.

References

1. Saha, S.; Desiraju, G. R. *J. Am. Chem. Soc.*, **2017**, *139*, 1975−1983.

2. Saha, S.; Desiraju, G. R. *Chem. Commun.*, **2017**, *53*, 6371− 6374.

Appendix

The disc attached contains the following supporting files and videos.

- **Chapter 3:**
  - ✓ CIF data files and Check CIF reports for all the structures.
  - ✓ Video showing the thermal ellipsoid vibration of ABN·2DMABN crystal structures.
- **Chapter 4:**
  - ✓ CIF data file and Check CIF report.
  - ✓ Video showing plastic bending of 4-bromobenzonitrile (4-BBN).
  - ✓ Video showing the melting of the straight crystal (4-BBN-S)
  - ✓ Video showing the melting of the bent crystal (4-BBN-B)
- **Chapter 5:**
  - ✓ CIF data files and Check CIF reports for all the structures.
  - ✓ Video showing thermosalience of 4-aminobenzonitrile (ABN) crystal.
  - ✓ Video showing thermosalience of ABN crystal covered slightly with oil.
  - ✓ Video showing the Hirshfeld surface of ABN crystal at 160 K.
  - ✓ Video showing the Hirshfeld surface of ABN crystal at 180 K.